2019

Examining Mechanisms Regulating Microtubule Assembly and Function

Melissa Pamula

EXAMINING MECHANISMS REGULATING MICROTUBULE ASSEMBLY AND FUNCTION

A Thesis Presented to the Faculty of

The Rockefeller University

in Partial Fulfillment of the Requirements for

The degree of Doctor of Philosophy

By

Melissa Pamula

June 2019

EXAMINING MECHANISMS REGULATING MICROTUBULE ASSEMBLY AND FUNCTION

Melissa Pamula, Ph.D.

The Rockefeller University 2019

Microtubules are cytoskeletal polymers assembled from α and β tubulin subunits that function in essentially all cellular activities. Microtubules can act as "tracks" for intracellular cargo transport, are required for cilia- and flagella-based motility, and establish cell morphology in specialized cells such as neurons. In dividing cells, a bipolar spindle assembles from microtubules and partitions genetic material into two daughter cells. Proper microtubule function in these diverse contexts depends on the assembly dynamics of microtubules and their organization into specialized arrays. Both intrinsic factors including the tubulin isotype composition of microtubules and extrinsic factors including microtubule-associated proteins (MAPs) can impact microtubule assembly dynamics. However, the contribution of tubulin isotype composition to microtubule dynamics is not well understood.

In the first part of this thesis, I explore the impact of specific β tubulin isotypes on microtubule dynamics. Microtubules undergo dynamic instability, an intrinsic property in which filaments in bulk equilibrium switch between periods of growth and shrinkage. The rate of polymerization and depolymerization can be quantified, as well as the frequency of switching between these states. I selected the two major β tubulin isotypes (βIIB and βIII) expressed in the vertebrate brain for examination. Using an expression and purification system developed in our lab, I generated recombinant tubulin heterodimers that were

isotypically pure in β tubulin composition. I used *in vitro* reconstitution and total internal reflection fluorescence (TIRF) microscopy to examine the dynamics of individual microtubules assembled from these distinct heterodimers. I found that microtubules assembled with βIIB are substantially more stable, switching from a state of growth to a state of shrinkage (termed catastrophe) three-fold less frequently than their βIII-containing counterparts. These two isotypes differ substantially in the C-terminal tail, a region thought important for modulating interactions with MAPs but whose contribution to microtubule dynamics is not well understood. I found that swapping the C-terminal tails did not substantially alter dynamic instability parameters. These data reveal that isotype-specific polymerization properties are mediated by residue changes in the structured "core" of tubulin, rather than the divergent C-terminal tail.

In the second part of the thesis, I examine the contribution of microtubule bundles to chromosome movement during anaphase. As sister chromosomes separate, a specialized array of microtubules called the spindle midzone assembles between the segregating chromosomes. Within this structure, microtubules overlap in the antiparallel orientation and are cross-linked by the non-motor MAP, Protein Regulator of Cytokinesis 1 (PRC1), forming bundles. Current models suggest that the spindle midzone can function to facilitate or restrict chromosome movement, however it is unclear how the accumulation of PRC1 on midzone microtubule bundles impact these activities. Using lattice light sheet microscopy, I examined the time-dependent changes in microtubule overlap length that accompany anaphase chromosome movement. I then selectively disrupted midzone formation by knocking down PRC1 and found that chromosome segregation distance and speed increased. These data support a model in which the spindle midzone, rather than

aiding in chromosome segregation, instead restricts chromosome movement. Replacing endogenous PRC1 with a mutant that has reduced microtubule affinity reveals that the change in microtubule overlap length is coupled to the braking function of the midzone.

My PhD work provides insight into two areas of microtubule assembly regulation. The studies detailed in chapters 2 and 3 reveal how changes in tubulin primary sequence impact polymerization properties of microtubules *in vitro*. The studies detailed in chapter 4 reveal how changes in the organization of microtubules in cells contributes to spindle function and chromosome segregation during anaphase.

To my parents,

Nancy and John Pamula,

For their limitless support and love

Acknowledgements

I am deeply grateful for the continued support and guidance from my advisor, Dr. Tarun Kapoor. Thank you for teaching me to think and write critically. My relationship with science (and adjectives) will never be the same.

I would like to thank my committee, Dr. Fred Cross and Dr. Titia de Lange, for their insight and feedback. Thank you for helping me set reasonable goals and make plans to achieve them. Thank you to my external examiner, Dr. Julie Canman, as well.

I would like to extend a special thanks to my colleague and biochemist extraordinaire, Shih-Chih (Jeff) Ti. You taught me to strive for both precision and accuracy in all of my bench work. Your positivity and enthusiasm for science sets an example for everyone to follow.

To the rest of my colleagues, both current and former, thank you for making my time in the lab both challenging and fun.

To all my friends, especially those in NJ, NY, CA, and NC, thank you for making life interesting.

To my family, thank you for your constant encouragement and support. I would not be here without you.

Finally, to my husband, Dan Ball, thank you for everything you do. Thank you for putting up with late dinners and early coffee. Thank you for cooking my favorite foods. Thank you for reminding me of what is important.

Table of Contents

List of Figures

Chapter 4:

List of Tables

Chapter 1: Microtubule dynamics and the spindle midzone in animal cells

1.1 Introduction

Microtubules are organized into complex arrays that perform essential functions in dividing and non-dividing cells. One such example is the mitotic spindle which assembles from >1000 microtubules (McIntosh and Landis, 1971) and functions to segregate chromosomes during cell division. Individual filaments cycle from polymer to monomer form and back while the spindle assembles, partitions the genetic material into two daughter cells, and then disassembles (Inoué and Sato, 1967). Microtubule assembly can be controlled at least two ways: through interactions with microtubule-associated proteins (MAPs) and by altering the tubulin composition of the microtubules (reviewed in(Roll-Mecak, 2019)).

This chapter describes the structure and function of the spindle midzone, a specialized microtubule-based structure that assembles in anaphase, in the context of models for chromosome motion. The primary focus is on data from vertebrate systems, contrasting with data from yeast and other invertebrates where appropriate. The impact of key MAPs on specific properties of microtubules and the implications for midzone function will be discussed. Finally, this chapter reviews how data from *in vitro* examination of filament dynamics and structure inform our current understanding of microtubule assembly.

1.2 Electron Micrograph Studies of the Anaphase Spindle and Relevance to Mechanisms of Anaphase B Spindle Elongation

Early cytologists examining dividing cells proposed two models for chromosome segregation: one that involved pushing from elements between the separating chromosomes (proposed by Druner in 1984; see (Rappaport, 1996) p. 22), and one that involved pulling from proteins on the cell cortex (proposed by Boveri in 1988; see (Schrader, 1949) p. 41). Though over 100 years of research have followed, these two ideas still lie at the heart of current models of chromosome movement.

Chromosome segregation proceeds through two distinct processes. Anaphase A refers to the movement of sister chromatids move towards opposite spindle poles (reviewed in (Asbury, 2017)). Anaphase B refers to spindle elongation along the pole-to-pole axis, further driving chromosome separation (reviewed in (Scholey et al., 2016)). Early experiments in insect cells revealed that certain drugs could specifically inhibit anaphase B but not anaphase A (Ris, 1943, 1949), suggesting that although these processes occur simultaneously in many systems, they are mechanically distinct. It is now clear that chromosome-to-pole movement is driven primarily by the shrinkage of the kinetochore-attached (k-fiber) microtubules. The mechanisms of anaphase A movement have been recently reviewed (Asbury, 2017) and will not be discussed in this section. Current models suggest that spindle elongation is driven primarily by interactions of non-kinetochore microtubules with motor and non-motor proteins, including those that contact the cortex (on astral microtubules) and those that cross-link microtubules in the midzone (on interpolar microtubules) (**Fig. 1.1**). This section reviews the data that support this model.

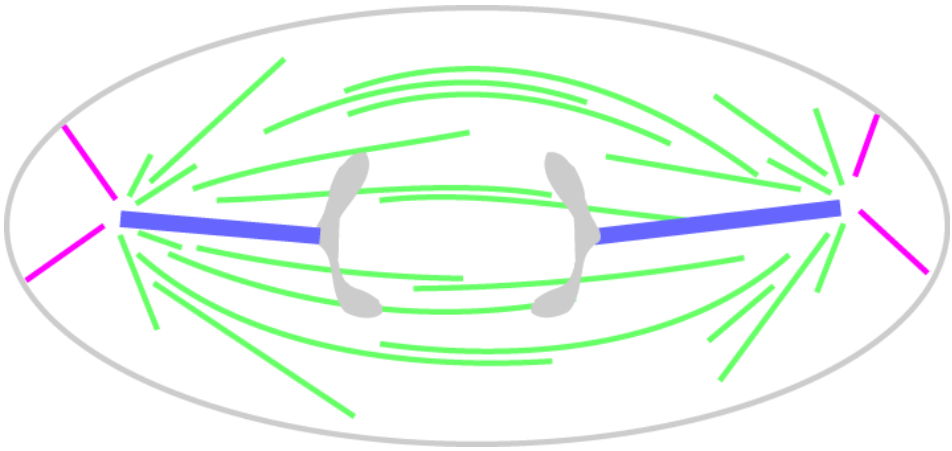

Figure 1.1. Cartoon of a human cell in anaphase.

Kinetochore-fiber microtubules (blue) attach to chromosomes (gray) during mitosis. Non-kinetochore microtubules include astral microtubules (pink) that contact the cell cortex and interpolar microtubules (green) that can interdigitate in between the segregating chromosomes.

Background and brief history

Several models were initially proposed to explain anaphase B spindle elongation. In 1967, Inoué postulated that spindles could elongate based on polymerization of microtubules alone (Inoué and Sato, 1967). This predicted that spindles would be composed of continuous microtubules that span the entire pole-to-pole length. Another early theoretical model proposed by McIntosh and colleagues recognized the importance of microtubule polarity (Mcintosh et al., 1969): similar to the mechanism of myosin-actin interactions during muscle contraction (Huxley, 1963, 1969), the proposed mitotic sliding filament model predicted that a motor protein localized to microtubules between chromosomes could generate forces to drive chromosome movement. This predicted that

only one kind of microtubule orientation could allow for such motion: one in which filaments of opposite polarity interdigitate in between the segregating chromosomes. Both models presented testable hypotheses that could be examined in subsequent electron micrograph studies.

Length and polarity of microtubules in anaphase spindles

Serial section electron microscopy studies have revealed the 3D ultrastructural position of microtubules in anaphase spindles from diverse eukaryotes. Early studies of cultured human cells revealed that few, if any, continuous microtubules were present (Brinkley and Cartwright, 1971; McIntosh and Landis, 1971), which did not support the simple model proposed by Inoué. In these data, the total number of microtubules were counted in select sections perpendicular to the pole-to-pole axis and plotted as a function of position along the pole-to-pole axis. In anaphase spindles, the planes near the cell equator had a higher number of microtubules compared to those on either side. This suggested that microtubules interdigitate near the spindle equator, providing early support for the sliding filament model.

Early ultrastructural studies were limited by the inability to assign microtubule polarity. Microtubules are intrinsically with distinct plus and minus ends (reviewed in section 1.4). The polarity of anaphase microtubules was unambiguously assigned using the method of hook decoration (Heidemann and McIntosh, 1980). In these studies, a special buffer was used to stimulate the association of tubulin dimers into ribbons. These ribbons can associate laterally with the protofilaments of pre-existing microtubules and will appear as hooks when looking down the long axis of a microtubule. Depending on the handedness

of the hooks, the polarity of the microtubule can be assigned. In permeabilized human cells, this approach was used to show that microtubules on opposite sides of the midbody in telophase cells were of opposite polarity and associate in an antiparallel organization at the cell equator (**Fig. 1.2**) (Euteneuer and McIntosh, 1980). The same method was applied to study microtubules in the *Haementhus* endosperm phragmoplast, a plant-specific microtubules structure that assembles in anaphase, revealing the presence of antiparallel microtubules there as well (Euteneuer et al., 1982; McIntosh and Euteneuer, 1984). Similar conclusions were made using flagellar dynein, which binds the microtubule lattice with identifiable polarity (Telzer and Haimo, 1981). Thus, a key prediction of the sliding filament hypothesis was confirmed.

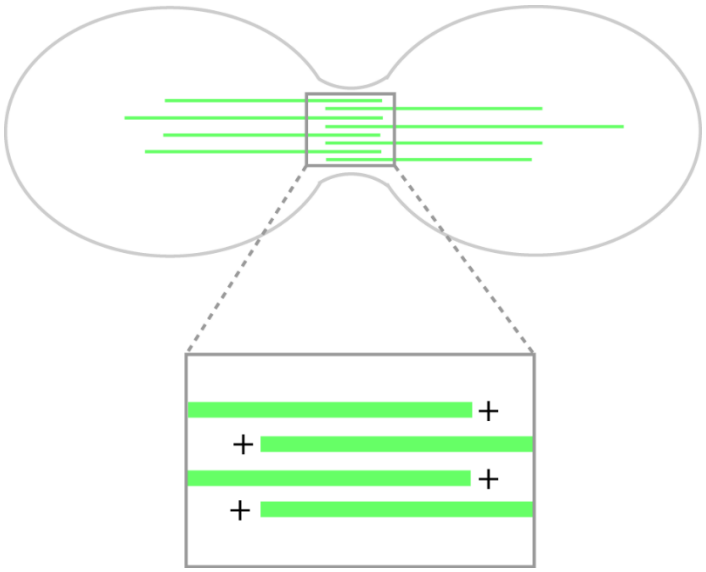

Figure 1.2. Cartoon of spindle microtubules in a cell in telophase.

Microtubules (green) in the midbody interdigitate with plus-ends overlapping (inset).

Studies in single-celled organisms, with their relatively small spindles composed of only a few dozen or a few hundred microtubules, were informative regarding the mechanisms of anaphase B. The spindles of diatom (*Diatoma vulgare*) are unusual in that the k-fiber microtubules attached to chromosomes are spatially separated from interpolar microtubules, providing a particularly clear view of the almost paracrystallin array of the 250-300 microtubules in the spindle midzone (McDonald et al., 1977). Over a period of ~20 years, serial section electron microscopy was used extensively to examine spindles from widely studied model organisms including slime mold (McIntosh et al., 1985), fission yeast (Ding et al., 1993), and budding yeast (Winey et al., 1995). These studies revealed that the organization of microtubules into a bipolar array, with some microtubules associating with chromosomes and others interdigitating in the spindle midzone, is a recurring motif throughout eukaryotes (**Fig. 1.1**).

Evidence for microtubule sliding within midzone microtubule bundles

Several observations provided support for a sliding filament mechanism of spindle elongation. During anaphase, the length of microtubule interdigitation in the midzone decreases proportionally as the spindle elongates (McDonald et al., 1977). Importantly, the ends of microtubules that overlap in the center of the cell terminate at or very close to the spindle pole and could therefore directly push on poles (referred to here as “midzone pushing”). Kinetochore fiber microtubules are thought to form a mechanical connection between kinetochores and the pericentriolar material at the spindle poles, such that movement of the poles is directly coupled to movement of chromosomes (McDonald et al.,

1992). Together, these data suggest that microtubules are situated such that antiparallel sliding in the midzone could drive anaphase B chromosome movement in these organisms.

Some of the most detailed serial section electron micrograph studies of mammalian spindles was published from the McIntosh lab (McDonald et al., 1992; Mastronarde, 1993). These studies examined the distribution, lengths, and organization of microtubules in different stages of anaphase in mammalian PtK_2 (*Potorous tridactylis*) cells. Cross-sectional slices were imaged perpendicular to the pole-to-pole axis and individual microtubules were tracked through consecutive images. The authors classify microtubules into one of two groups: those that associate with kinetochores (hereafter, "k-fiber" microtubules), and those that do not (hereafter, "interpolar" microtubules). Consistent with observations in lower eukaryotes, a subset of interpolar microtubules in PtK_2 cells interdigitate, forming bundles of filaments. The region of microtubule overlap in bundles decreased in length during anaphase, consistent with microtubules sliding.

Several observations in PtK_2 spindles challenged the hypothesis that microtubule sliding is the predominant mechanism of spindle elongation in all eukaryotes. Unlike in the small spindles mentioned above, the minus ends of bundled interpolar microtubules are not predominantly located near poles and are instead distributed over half of the spindle length. Only a small fraction of these minus ends is observed near the pole and only in early stages of anaphase. In addition, a fair number of microtubules were observed with two free ends (not associated with chromosomes, microtubule bundles, or poles). Microtubule nucleators are not conserved in all systems and could explain some of these observations (Kollman et al., 2011). Nevertheless, the distribution of the position of minus ends in microtubule bundles raised doubts as to whether microtubule sliding was occurring much at all. From

metaphase to mid-anaphase, minus-ends moved away from the midplane at the same distance that the poles moved away from the midplane. However, from mid anaphase to late anaphase, the position of plus-ends relative to the spindle midplane narrows four-fold, but the distribution of minus-end positions does not change, suggesting that microtubule sliding may not be occurring during this period. Together, these data suggest that different structural and functional principles may be guiding chromosome movement in mammals and other large spindles compared to those in the small spindles of non-mammalian species.

1.3 The contribution of microtubule-associated proteins to Anaphase B

Work by Nicklas provided the first direct measurements of the absolute force generated by anaphase spindles. Using calibrated glass microneedles to pull on individual chromosomes, Nicklas measured the stall force (the force required to inhibit chromosome movement) to be ~700 pN (Nicklas, 1983), over 1000x greater than the estimated force required to move a chromosome through the viscous drag of the cytoplasm (~0.1 pN) (Nicklas, 1965). The forces that must be overcome in order to stall chromosome movement is likely a combination of those involved in both anaphase A and B movement. Anaphase A movement is thought to be driven by microtubule depolymerization, which utilizes the energy of GTP hydrolysis stored as strain energy in the microtubules lattice (reviewed in section 1.4 and 1.5) (Asbury, 2017). Consistent with this hypothesis, experiments using permeabilized mammalian (PtK1) cells revealed that anaphase B but not anaphase A requires ATP and the loss of anaphase B movement cannot be rescued by addition of excess GTP (Cande, 1982). Thus, these two processes are mechanistically distinct.

Numerous motor and non-motor proteins have been identified that localize to the spindle and likely work in concert to coordinate anaphase B motion. In *C. elegans*, the mechanism of anaphase B has been extensively studied. In this system, astral pulling forces provide the major mechanism for spindle elongation (Grill et al., 2001, 2003). These forces are thought to be generated by microtubule depolymerization as well as dynein motors walking toward the minus end of microtubules (Kozlowski et al., 2007; Laan et al., 2012) The relative contribution of these proteins, among others (discussed below) in mammalian cells spindle elongation and midzone function is still poorly understood.

Non-motor proteins required for midzone assembly

PRC1/Ase1/MAP65/Feo/SPD-1

MAP65 family members were first identified following biochemical fractionation of cytoplasmic extracts in plants as 60-65-kDa microtubule associated proteins capable of bundling Taxol-stabilized microtubules (Chang-Jie and Sonobe, 1993). The budding yeast homolog was soon identified in a screen for synthetic lethality in a *Bik1* null background and named Anaphase Spindle Elongation 1 (Ase1) (Pellman, 1995). Mutations in Ase1 cause the spindle to prematurely fracture and disassemble in mid-anaphase. Homologs have since been identified in other organisms including fission yeast, *Drosophila, C. elegans,* and human, all of which are involvedin spindle midzone assembly and anaphase B spindle elongation (Jiang et al., 1998; Mollinari et al., 2002; Schuyler et al., 2003; Verbrugghe and White, 2004; Vernì et al., 2004; Yamashita et al., 2005). In this section, I refer to MAP65/Ase1/PRC1 proteins as PRC1 following convention in mammalian cells.

PRC1 is a critical regulator of midzone assembly. Whereas the loss of other microtubule cross-linking proteins leads to disorganized midzone bundles, the loss of PRC1 inhibits the assembly of microtubule bundles in diverse systems (Mollinari et al., 2002; Schuyler et al., 2003; Verbrugghe and White, 2004; Vernì et al., 2004; Yamashita et al., 2005; Mollinari et al., 2005). Three activities have been ascribed to PRC1 family members that underlie their function in the spindle midzone: cross-linking microtubules, resisting filament sliding, and recruiting proteins to the midzone.

Microtubule cross-linking lies at the heart of PRC1 function. Unlike several other microtubule cross-linking proteins, PRC1 exhibits specificity towards cross-linking microtubules in the antiparallel orientation (Loïodice et al., 2005; Gaillard et al., 2008).

Several structural studies have provided insight into how microtubule cross-linking is achieved (Subramanian et al., 2010, 2013; Kellogg et al., 2016). PRC1 forms a homodimer that is likely flexible in solution but becomes rigid upon microtubule binding (**Fig. 1.3**). This rigidity is thought to impose specificity for crosslinking microtubules in the antiparallel orientation.

A second function of PRC1 family proteins is the ability to oppose filament movement driven by motor proteins. Yeast PRC1 has been shown to antagonize kinesin-14 activity to prevent filament sliding (Braun et al., 2011; Janson et al., 2007). *In vitro* studies have provided insight into a possible mechanism. When microtubules that are cross-linked by budding yeast Ase1 slide apart, the density of Ase1 in regions of microtubule overlap increases. This creates an entropic force that can resist filament sliding forces generated externally (by lamellar flow) or within microtubule overlaps (by Kinesin-14/Ncd motors) (Braun et al., 2011; Lansky et al., 2015). For such a force to be sustained for several minutes, the off-rate would need to be low (Braun et al., 2011). Fluorescence recovery after photobleaching (FRAP) experiments have shown that Ase1 turnover in the spindle midzone is very slow (Schuyler et al., 2003; Fu et al., 2009; Khmelinskii et al., 2009). Anaphase in yeast typically lasts ~20 mins and the half-life of Ase1 turnover is > 7 minutes, suggesting that it is effectively immobile over the duration of anaphase (Schuyler et al., 2003). Whether mammalian PRC1 shares this propertyis still unknown.

Finally, PRC1 regulates the recruitment of dozens of proteins to the midzone via direct and indirect interactions (Roostalu et al., 2010). PRC1 directly binds several midzone-associated proteins including Kif4 (discussed below), MKLP1, MKLP2, KIF14, Plk1 and CLASP (Kurasawa et al., 2004; Gruneberg et al., 2006; Neef et al., 2007; Liu et

al., 2009). In addition, other proteins not known to directly bind PRC1 are recruited to the midzone in a PRC1-dependent manner and perform important functions during anaphase and cytokinesis (Khmelinskii and Schiebel, 2008).

How does PRC1 mediate the recruitment of proteins to the midzone in anaphase but not in metaphase? Anaphase onset initiates the destruction of cyclin B and the inhibition of CDK1 kinase. Numerous mitotic proteins are rapidly dephosphorylated, a process that is required for proper spindle function and chromosome segregation. In particular, phosphoregulation of PRC1 appears to be a conserved element of this regulatory mechanism throughout eukaryotes (Roostalu et al., 2010). PRC1 is hyperphosphorylated during metaphase, which controls its association with the spindle (Zhu et al., 2006). In human cells, premature dephosphorylation causes microtubule hyper-bundling in metaphase, and improper phosphorylation of PRC1 in anaphase prevents disrupts midzone assembly (Zhu et al., 2006). In yeast, PRC1 phosphorylation directly controls Cin8 (a kinesin-5) localization and sliding activity, required for proper spindle elongation (Khmelinskii et al., 2009). PRC1 phosphorylation is controlled by at least two kinases, CDK1 and Plk1. Inactivation of Plk1 in metaphase by chemical inhibition results in the dephosphorylation of PRC1 at Thr-602, causing an anaphase-like midzone to assemble in metaphase, marked by the premature recruitment of PRC1 to microtubules and the formation of microtubule bundles (Hu et al., 2012). In addition, a number of other midzone-associated proteins are prematurely recruited including Mklp1 and CENP-E, suggesting that dephosphorylation of PRC1 is sufficient to recruit a subset of midzone-associated proteins.

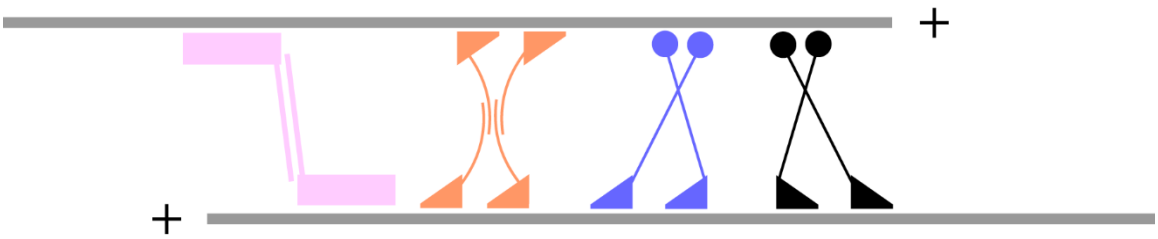

Figure 1.3. Schematic of microtubule cross-linking proteins.

PRC1 (pink) forms a homodimer that simultaneously engages two microtubules (gray) in the antiparallel orientation. Microtubule plus-ends (+) are indicated. Eg5 (orange) forms a bipolar homotetramer that binds each filament with a set of motor domains that can each walk toward the plus-end of microtubules. Motor proteins Kinesin-4 (blue), a plus-end directed motor, and Kinesin-14 (black), a minus-end directed motor, form homodimers that interact with one filament through two motor domains (triangles) and the other filament through non-motor C-terminal domains.

Motor proteins that can slide antiparallel filaments apart

Microtubule sliding between antiparallel microtubules in the midzone contributes to anaphase B pole separation in diverse systems and can explain the full extent of pole separation in some eukaryotes (Scholey et al. 2016). Experiments using laser microbeams revealed that spindle elongation was inhibited following laser ablation of midzone but not astral microtubules in both diatom (Leslie and Pickett-Heapes, 1983) and fission yeast (Khodjakov et al., 2004; Tolić-Nørrelykke et al., 2004). Combined with the structural data

mentioned above, the evidence is particularly compelling that the midzone is the primary force generation site in these organisms.

Several lines of evidence support the idea that a bipolar motor protein, utilizing the energy from ATP hydrolysis, could slide apart microtubules to push poles and thus chromosomes apart. First, isolated diatom spindles require ATP for anaphase B (Cande and McDonald, 1985, 1986). Second, addition of an antibody against a pan-kinesin peptide that binds the motor domain on kinesins prevented anaphase spindle elongation (Hogan et al., 1993). Substantial effort has been made to identify the proteins responsible for this activity. Several candidate molecules are discussed below.

Kinesin-5/Eg5/KIF11/BimC/Cut7/Cin8p/Kip1p/Klp61F/BMK-1

BimC from the fungus *Aspergillus nidulans* was the first kinesin-5 family member identified from temperature-sensitive screens for defects in mitosis (Morris, 1975; Enos and Morris, 1990). Homologs were identified in other fungal species (Hagan and Yanagida, 1990, 1992; Hoyt et al., 1992). Mutations in these genes blocked bipolar spindle assembly, supporting the hypothesis that proteins in this family are involved in antiparallel microtubule interactions (Hagan and Yanagida, 1992; Roof et al., 1992). Later, homologs were identified in vertebrates whose depletion from *Xenopus* egg extracts caused similar defects (Sawin et al., 1992) or microinjection of antibodies into human cells (Slangy et al., 1995). Hereafter, kinesin-5 proteins are referred to as Eg5 following vertebrate convention.

Drosophila embryonic Eg5 was the first kinesin protein shown to have a bipolar structure (**Fig. 1.3**) (Cole et al., 1994; Kashlna et al., 1996). This protein assembles from

four polypeptides to form a dumbbell-shaped homotetramer with motor domains on opposite ends capable of cross-linking microtubules. Analogous to a miniature myosin filament, the protein was predicted to slide microtubules relative to one another. Elegant *in vitro* experiments revealed that Eg5 moves towards the plus-end on both microtubules that it crosslinks (**Fig. 1.4**) (Kapitein et al., 2005). Markers for microtubule polarity were used to show that sliding was specifically observed between microtubules in the antiparallel orientation (**Fig. 1.4)**.

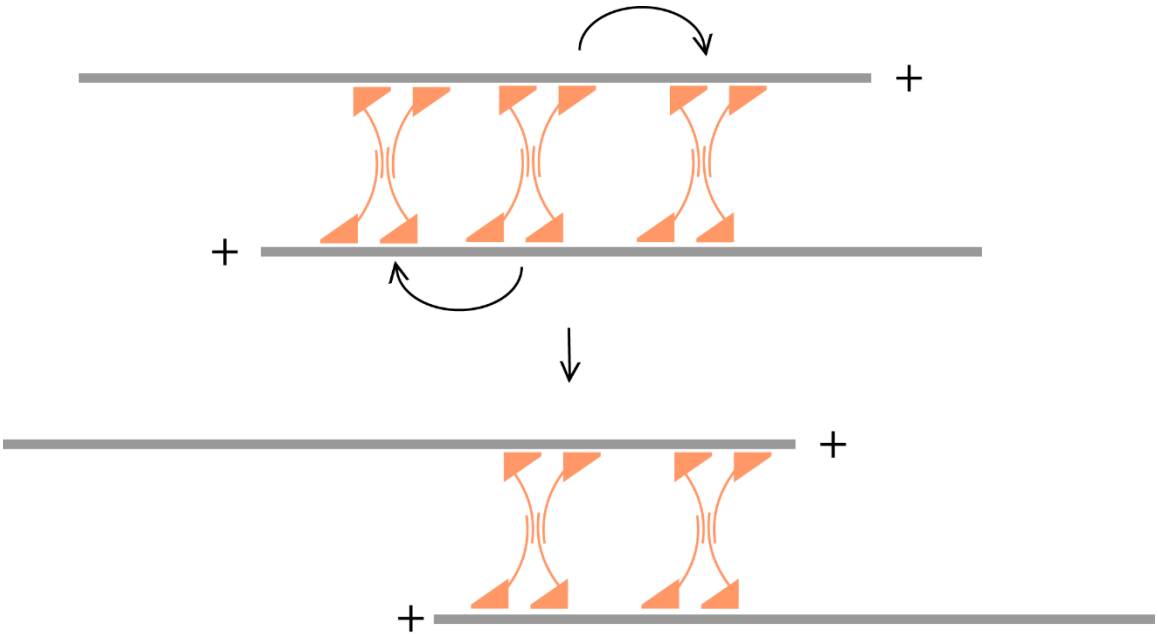

Figure 1.4. Schematic of antiparallel microtubule sliding by Eg5.

Microtubules (gray) overlap at plus-ends (+). Eg5 motors (orange) drive microtubules apart by stepping towards the plus-end on both microtubules it cross-links.

The development of selective small molecule inhibitors of Eg5 have been used to temporally control the inactivation of the protein and examine its role in different stages of mitosis (Mayer et al., 1999; Kapoor et al., 2000). Eg5 plays a clear role in the establishment of spindle bipolarity in many systems (Ferenz et al., 2010). Furthermore, it contributes to the maintenance of spindle bipolarity as inhibition causes rapid spindle collapse in yeast cells, *Drosophila* embryos, and *Xenopus* egg extract (Saunders and Hoyt, 1992; Sharp et al., 1999; Kapoor et al., 2000). Although injection of Eg5 antibodies into human (HeLa) cells does not cause spindle collapse (Slangy et al., 1995), inhibition of Eg5 in other vertebrate (LLC-Pk1) cells causes spindle shortening, a phenotype that may have been overlooked in the first report (Ferenz et al., 2009). Together, these data are consistent with a role for Eg5 in establishing spindle bipolarity by generating an outward-directed force.

Eg5 is recruited to the midzone after anaphase onset, suggesting that it may function to generate outward force to assist in spindle elongation (Sharp et al., 1999; Ferenz et al., 2010). Investigation of anaphase-specific roles of Eg5 has been complicated by the observation that knockdown causes metaphase arrest in many organisms. Two interesting exceptions are *C. elegans* embryos (Saunders et al., 2007) and *Dictyostelium* (Tikhonenko et al., 2008); knockdown does not inhibit bipolar spindle assembly and the rate of anaphase B pole separation is increased, suggesting that the protein instead acts to restrict relative filament sliding. Similarly, vertebrate (LLC-Pk1) cells treated with an Eg5 inhibitor in anaphase exbibit increased rates of pole separation (Collins et al., 2014). How can we explain these two apparently disparate functions during mitosis? Elegant *in vitro* experiments revealed that ensembles of Eg5 can either facilitate or inhibit relative filament sliding depending on the velocity of sliding (Shimamoto et al., 2015). These observations

suggest that forces that facilitate spindle elongation are counteracted by forces that slow it down, possibly through the action of Eg5 ensembles in the midzone.

Kinesin-8/Kip3

Kinesin-8 family members are perhaps best known for their ability to depolymerize microtubule ends (Varga et al., 2009). This activity scales with microtubule length and can accumulate length-dependent tags at the end of filaments *in vitro* (Varga et al., 2006; Leduc et al., 2012). In addition, budding yeast Kip3 has been shown to mediate antiparallel sliding *in vitro* (Su et al., 2013). Both microtubule sliding and microtubule depolymerization activities of Kinesin-8 contribute to spindle elongation during anaphase in budding yeast (Su et al., 2013; Rizk et al., 2014). However, the precise role of this protein in vertebrates is still unknown.

Kinesin-6/KIF23/Mklp1/CHO1/Pavarotti/ZEN-4

In vertebrates, kinesin-6 family members play crucial roles during midzone assembly and cytokinesis (White and Glotzer, 2012). First identified as the gene that encodes the antigen to the CHO1 monoclonal antibody, *Drosophila* MKLP1 is required for mitotic progression (Nislow, 1990; Nislow et al., 1992). Recombinant protein purified from bacteria was shown to slide apart antiparallel microtubules *in vitro* (Nislow et al., 1992). In higher eukaryotes including flies, worms, and mammals, Mklp1 forms a heterotetrameric complex with a Rho GTPase activating protein in a 2:2 ratio to form the centralspindlin complex (Mishima et al., 2002). An equivalent complex has not been

identified in yeast, although evidence from fission yeast suggests that kinesin-6 molecules can form homotetramers that promote anaphase spindle elongation (Fu et al., 2009). Only the complete centralspindlin complex has been shown to exhibit motor activity although recent evidence suggests that kinesin-6 dimers can cross-link microtubules (Tao et al., 2016).

Kinesin-4/Kif4/Klp3A

Like Eg5, vertebrate Kif4 is recruited to the midzone following anaphase onset. No known Kif4 homologs have been identified in yeast, suggesting functional specialization of the protein in the lineages it is found in. Kif4 is a member of kinesin-4 family of proteins that homodimerizes and processively walks toward the plus-end of microtubules (**Fig. 1.3**). the Drosophila Kif4 organizes midzone microtubules and is thought to couple anaphase onset with the reduction of poleward microtubule flux.

Kif4 and PRC1 interact directly to form a stable complex *in vitro* and are thought to 'measure' microtubule overlap length in dynamic filament networks (Bieling et al., 2010; Subramanian and Kapoor, 2012; Subramanian et al., 2013). Evidence for this hypothesis has been shown in two studies. Controlled *in vitro* assays have revealed that PRC1/kinesin-4 can autonomously regulate antiparallel overlap length of dynamic microtubules (Bieling et al., 2010). In cells, Kif4 is proposed to function as a regulator of midzone length by suppressing microtubule plus-end dynamics (Hu et al., 2011). In addition, PRC1/kinesin-4 in complex can form micron-sized tags (hereafter, "end-tags") at microtubule plus-ends (Subramanian et al., 2013). The end-tag length is proportional to microtubule length *in vitro* and during anaphase in human cells. Antenna-like models can

be used to explain how PRC1/kinesin-4 can detect microtubule length and overlap length to regulate end-tag length or inhibit plus-end microtubule growth (Bieling et al., 2010; Subramanian et al., 2013). However, we do not know how the length-dependent regulation of individual filaments or overlap regions between filaments contributes to spindle midzone assembly in human cells.

A recent report has shown that Kif4 alone can cross-link and slide microtubules but has no specificity towards antiparallel or parallel microtubules (Wijeratne and Subramanian, 2018). However, in the presence of PRC1, it can specifically slide microtubules in the antiparallel orientation and form bundles of filaments with overlap lengths proportional to the sum length of the filaments in the bundle. The midzone function of Kif4 may involve both filament sliding and suppression of microtubule dynamics.

Antiparallel sliding: pushing or breaking?

Structural studies as well as *in vitro* reconstitution approaches mentioned above support a model in which microtubules in the midzone can undergo relative filament sliding and that this activity is driven by motor proteins in the spindle midzone. However, microtubule sliding itself does not reveal the source of the proteins involved in this movement. Conceptually, sliding could also result from forces acting outside of the midzone that pull the microtubules in opposite directions.

Protein activities involved in cortical pulling

The observation that many microtubule minus-ends in mammalian spindles do not reach the spindle poles supported the hypothesis that protein activity outside of the midzone could be involved in anaphase B movement (Mastronarde, 1993). Live cell imaging of centrosome movement in newt cells (*Taricha granulosa*) during different stages of mitosis revealed that each centrosome maintained a high degree of independence, supporting the idea that centrosome separation during vertebrate spindle formation is not produced by MT-MT interactions between opposing asters, i.e., that the mechanism is intrinsic to each aster (Waters et al., 1993). Two years earlier, experiments using the fungus *Nectria haematococca* revealed direct evidence for the existence of astral pulling forces during anaphase B (AIST et al., 1991). Studies were then completed in *C. elegans* and found similar results (Grill et al., 2001). Later, experiments in *Ustilago maydis* revealed that cortically-anchored dynein was identified as a key motor protein involved in this process (Fink et al., 2006).

Molecules that can drive parallel sliding

Dynein/NuMA

Laser microsurgery experiments have revealed that kinetochore microtubules can form lateral attachments to non-kinetochore microtubules (McDonald et al., 1992; Elting et al., 2014). In these experiments, a single k-fiber, which is composed of bundled parallel microtubules and can be observed using fluorescence microscopy, is severed halfway between the pole and the kinetochore. The newly generated plus-ends on the side of the cut proximal to the spindle pole undergo rapid depolymerization, but the remaining stub

attached to the kinetochore can move toward the pole in a dynein-dependent manner. It is attractive to think that such poleward directed forces could act on minus ends of interpolar microtubules in bundles. However, the difficulty of tracking minus ends in dividing cells, along with the observation that the minus ends of microtubules in a single bundle are usually not clustered together, make it difficult to perform a similar experiment on midzone microtubules.

Kinesin-12/Kif15

Kinesin-12 family members have not been widely examined. Human kinesin-12 can form homotetramers that can cross-link microtubules and walk processively toward the plus-end (Drechsler et al., 2014). Kinesin-12 motors can cross-link and slide parallel microtubules, and can maintain spindle bipolarity in the absence of Eg5 (Drechsler and McAinsh, 2016). However, whether it is involved in any aspect of anaphase movement has not been explored.

Multiple motor and non-motor proteins that interact with microtubules during anaphase can work in concert to amplify or antagonize the activity of each other, making it difficult to reveal the relative contribution of each to anaphase B movement. While fission yeast, for example, rely almost exclusively on midzone-driven microtubule sliding for spindle elongation (Ding et al., 1993; Khodjakov et al., 2004; Tolić-Nørrelykke et al., 2004), same cannot be said for many vertebrate systems (for review, see (Scholey et al., 2016)). For example, spindle elongation in *C. elegans* embryo relies primarily on astral pulling forces (Grill et al., 2001). Thus, more work is needed to determine the precise function of the spindle midzone in human cells.

1.4 Microtubule assembly and dynamic instability

When cells enter mitosis, the interphase microtubule array is rapidly (< 1 min) disassembled and new microtubules are assembled around chromosomes to form the mitotic spindle (Zhai et al., 1996). These mitotic microtubules are substantially more dynamic than their interphase counterparts, a property that appears to be important for proper spindle assembly. When microtubule dynamics are perturbed with microtubule-stabilizing drugs such as paclitaxel or destabilizing drugs such as nocodazole, cells arrest in metaphase and will enter apoptosis after prolonged arrest (Jordan et al., 1996). Thus, the regulation of microtubule dynamics and turnover is important to ensure proper spindle function. It is important to understand the dynamics of microtubules assembled in the absence of other regulatory proteins (discussed in sections 1.5 and 1.6), as this forms the basis of our understanding of microtubule dynamics in cells.

Overview of dynamic instability

A fundamental property of microtubules is their ability to undergo dynamic instability; microtubules can stochastically switch between periods of growth and shrinkage such that both populations co-exist in a bulk steady state (Mitchison and Kirschner, 1984). Observed both *in vitro* and *in vivo*, dynamic instability is thought to be the primary mechanism controlling microtubule assembly (Horio and Hotani, 1986; Cassimeris et al., 1988). This process is intrinsic to microtubules and occurs in the absence of associated proteins, although numerous microtubules-associated proteins (MAPs) have been identified that can strongly modulate dynamics (Akhmanova and Steinmetz, 2015) (reviewed in section 1.4 and 1.6). This section will focus on microtubule assembly from

tubulin alone, which lays the foundation for understanding how MAPs can impact specific aspects of this process.

Microtubule dynamic instability can be described using four parameters: rate of growth (hereafter, "polymerization rate"), rate of shrinkage (hereafter, "depolymerization rate"), frequency of switching from growth to shrinkage (hereafter, "catastrophe") and frequency of switching back (hereafter, "rescue") (Desai and Mitchison, 1997) (**Fig. 1.5 A**). Occasionally a fifth parameter is used (called "pause ratio") which describes the fraction of time spent in a state of quiescence during which no detectible length change occurs. It is conceivable that such a state represents an intermediate between polymerization and depolymerization but could also reflect a state during which the ends are being modified but the length changes are below the level of detection of most microscope systems (Kerssemakers et al., 2006; Schek et al., 2007).

Microtubules are assembled from α/β tubulin heterodimers in a head-to-tail configuration, which imparts intrinsic polarity to the filament. Both α and β subunits bind GTP (Weisenberg et al., 1968), but only β-tubulin hydrolyzes GTP (at the exchangeable site, hereafter "E-site") and releases phosphate following incorporation into the microtubule lattice (Weisenberg and Deery, 1976). Microtubule ends were first defined based on their distinct dynamics; the faster-growing end was noted as the plus-end and the slower-growing end, the minus-end (Allen and Borisy, 1974). When new ends are created via microtubule severing, each end has a unique response: the newly generated plus-ends rapidly shrink, while the minus-ends are stable and can continue to grow

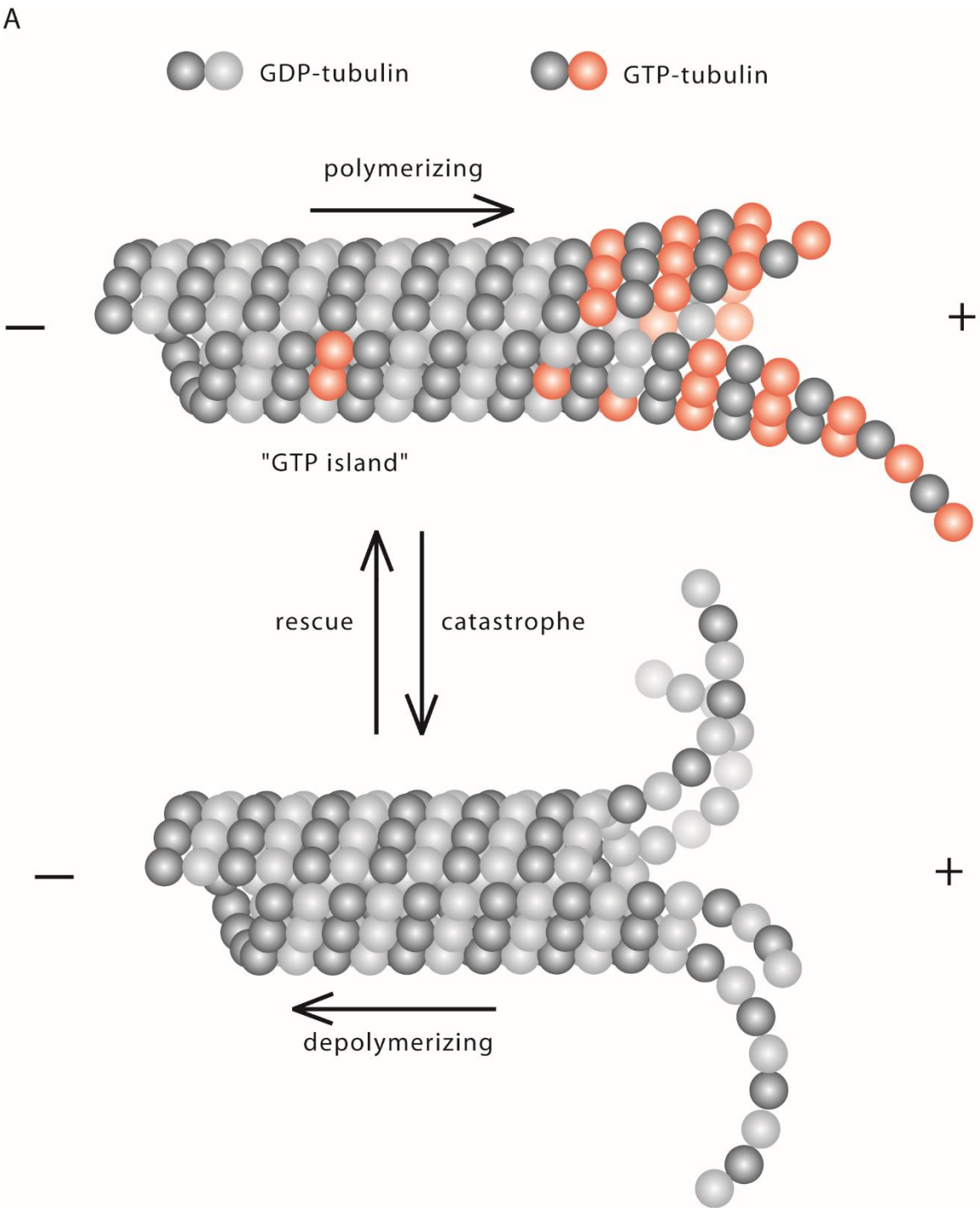

Figure 1.5 Microtubule dynamic instability.

(**A**) Cartoon illustrating GTP-tubulin incorporation at microtubule plus-ends (+) and GDP-tubulin dissociation during depolymerization. Microtubules stochastically switch between periods of growth and shrinkage (termed “catastrophe”) and back again (termed “rescue”).

(Walker et al., 1989; Tran et al., 1997). We now know that the plus-end terminates with β-tubulin facing out and the minus-end terminates with α-tubulin. Three lines of evidence support this claim: First, *in vitro* experiments showed that GTP-coated beads bind only to microtubule plus-ends, presumably at the β-tubulin E-site (Mitchison, 1993). Second, negative stain electron microscopy revealed that kinesin motor head binds on the side closer to the plus-end (Hirose et al., 1995), and it was previously shown that kinesin motor head binds exclusively to β-tubulin (Song and Mandelkow, 1993). Third, beads coated with an antibody raised against an N-terminal fragment of α-tubulin bound exclusively to the minus-ends of axonemes (Fan et al., 1996). While we have a good understanding of many aspects of tubulin polymerization *in vitro*, a complete understanding of the molecular basis of microtubule assembly is still lacking.

Microtubules elongate by adding GTP-bound tubulin to the ends in a process termed polymerization. Important insight into microtubule elongation was provided by Walker et al. (1988) who determined the association and dissociation rate constants of microtubule elongation by examining individual microtubules assembled from purified brain tubulin. These rates can be determined from a plot of microtubule polymerization rate over tubulin concentration, which shows a linear dependence (Oosawa, 1975). Polymerization rate increases with increasing free tubulin concentration, although the steepness of this dependence is typically different for plus- and minus-ends (Walker et al., 1988). The slope and y-intercept provide the association (a second-order reaction) and dissociation (a first-order reaction) rate constants, respectively. By contrast, microtubule depolymerization is a unimolecular reaction, insensitive to free tubulin concentration and occurs as GDP-bound tubulin dissociates from the microtubule end. The depolymerization

rate is thus governed primarily by the dissociation rate constant of GDP-tubulin from the microtubule lattice. The association rate constants measured here were 2-6x greater than those reported in previous studies (Mitchison and Kirschner, 1984; Gard and Kirschner, 1987), which were determined using a population assay, which can underestimate the rate of elongation due to catastrophe events. These rate constants have since been measured in numerous studies and can provide a simple way to compare microtubule polymerization dynamics assembled from tubulins of diverse origins.

GTP hydrolysis is required for depolymerization

GTP hydrolysis is at the heart of microtubule dynamic instability. Single microtubules never reach an equilibrium state and thus requires constant energy input in the form of nucleotide hydrolysis. The use of slowly-hydrolyzable GTP analogs such as GMPCPP have provided insight to how the energy from GTP hydrolysis is partitioned into different steps of the polymerization/depolymerization cycle (Hyman et al., 1992). GMPCPP binds to the exchangeable (E-site) on β-tubulin and undergoes a negligibly small amount of hydrolysis under typical experimental conditions (4×10^{-7} s^{-1}). Microtubules assemble from subunits bound to GMPCPP, revealing that the free energy of hydrolysis is not required for polymerization. In fact, microtubules assembled with GMPCPP have become valuable tools for studies of microtubule behavior *in vitro* because they can act as stable nucleators of microtubule growth (see chapters 2 and 3 for more detail) due to their slow rate of disassembly (0.1 s^{-1} compared to 500 s^{-1} for GDP-tubulin) (Hyman et al., 1992). Importantly, GMPCPP microtubules do not undergo dynamic instability.

In certain buffer conditions, hydrolysis of GMPCPP in polymerized tubulin can be stimulated, after which the microtubule undergoes rapid depolymerization, showing unambiguously that the energy from GTP hydrolysis drives dynamic instability (Caplow et al., 1994). This study showed that the polymerization of GMPCPP-bound tubulin is more favorable than that of the hydrolysis product, GMPCP-bound tubulin by ~4 kcal mol^{-1}. As the free energy of hydrolysis is only moderately larger (-5.2 kcal mol^{-1}), this suggested that most of the free energy of hydrolysis is harnessed as strain energy in the microtubule lattice and used primarily to destabilize microtubules. Later studies have shown that this energy can be harnessed to perform work in cells, e.g. the depolymerization of kinetochore-fiber microtubules is coupled to and drives anaphase A chromosome-to-pole movement in cells (Asbury, 2017). These data suggested that the microtubule lattice composed of GDP-bound tubulin is less stable than that composed of GTP-tubulin, likely due to a weakening of the inter-tubulin contacts following GTP hydrolysis.

Evidence that a GTP "cap" protects microtubules from disassembly

Microtubule disassembly is preceded by a catastrophe event in which the growing microtubule stochastically switches to a state of rapid shrinkage. Long-standing models of catastrophe postulated that it involves the loss of a stabilizing "GTP cap" at the microtubules end (Mitchison and Kirschner, 1984). Such a cap would act to stabilize microtubules by constraining the unstable GDP lattice. Evidence to support some kind of stabilizing cap came in part from microtubule severing experiments (using a laser microbeam or glass microneedle) which showed that individual microtubules severed distal

from the growing tip rapidly depolymerized at the newly generated plus-ends (Walker et al., 1989; Tran et al., 1997).

In solution, the hydrolysis rate of free tubulin in nonpolymerizing conditions is below the level of detection but is stimulated many-fold following incorporation into microtubules (0.1-6 s^{-1}) (David-Pfeuty et al., 1977; O'Brien et al., 1987; Caplow and Shanks, 1990). A GTP-cap would form if a lag occurs between the incorporation of GTP-tubulin and the initiation of GTP hydrolysis. If the rate of polymerization is higher, GTP-bound tubulins can accumulate near the microtubule end. Although it is known that GTP hydrolysis occurs relatively rapidly following polymerization, the rate at which GTP hydrolysis occurs is likely not fixed. If the GTP hydrolysis rate were constant, then catastrophe should be observed only over a very narrow range of concentrations, limited most likely to the lowest tubulin concentrations for which microtubule growth is observed. This is not the case; catastrophe events are observed over at least a two-fold range of tubulin concentrations and increasing tubulin concentration suppresses catastrophe frequency only modestly. These data suggest that there is likely some form of coupling between polymerization and GTP hydrolysis.

How many subunits of GTP tubulin must accumulate at the end to efficiently stabilize the microtubule from depolymerization? Substantial effort has been made to measure the size of the GTP cap. One way to indirectly measure this is to examine the behavior of dynamic microtubules by microscopy following rapid dilution of free tubulin. The time lag between tubulin washout and catastrophe can provide a readout of the size and stability of the GTP cap. This time lag has been shown to be relatively short (1-4 s), suggesting that the cap is also small (Walker et al., 1991). These data also showed that the

time lag was not dependent on polymerization rate, further supporting the model that polymerization rate and GTP hydrolysis are coupled. Later experiments sought to measure them minimum number of GMPCPP tubulins (mimicking the GTP tubulin cap) that must incorporate at the end of microtubules to stabilize it from depolymerization. These data showed that as few as 1-3 GMPCPP subunits at the end of each protofilament could be sufficient (Drechsel and Kirschner, 1994; Caplow and Shanks, 1996). However, other studies have estimated the size of the cap at over 1000 subunits in each protofilament (Seetapun et al., 2012). Without method to directly measure the presence of GTP tubulin at the microtubule end, the exact size the of GTP cap remains an open question.

Catastrophe is a multi-step process

Is the presence of a protective layer of GTP tubulin the only gatekeeper to microtubule catastrophe? Probabalistic analysis of the distribution of growth times of individual microtubules have revealed an additional level of complexity; microtubules were shown to age such that older microtubules are more likely to undergo catastrophe than younger microtubules (Odde et al., 1995). Fluorescence and electron micrographs show that microtubules become more tapered as microtubules age, suggesting that the structure of the microtubule end can contribute to its stability (Coombes et al., 2013). Together, these observations can only be explained if catastrophe is viewed as a multi-step process.

Models of microtubule catastrophe have undergone numerous rounds of refinement and reimagination as new data become available. Single filament models have been proposed that can explain many but not all experimental observation, in part because they

do not take into consideration lateral bond associations, and ultimately cannot account for the multistep catastrophe process. Current models now account for the hydrolysis state of subunits in multiple protofilaments but are still limited to only a subset of the 13 protofilaments that make up a typical microtubule (Bowne-Anderson et al., 2013).

Rescue, the transition from microtubule rapid shrinkage back to growth, is common in vivo but rare *in vitro* (Gardner et al., 2013). Rescues were thought to occur when the depolymerizing end encountered local lattice features such as GTP islands, clusters of GFP-bound tubulin heterodimers in the microtubule lattice (Dimitrov et al., 2008) (**Fig. 1.5 A**). These islands were thought to promote rescue by mimicking the GTP cap, although how they were introduced into the lattice were not understood. Recent reports have shown that microtubule damage can promote the spontaneous exchange of tubulin subunits in the middle of the polymer (Schaedel et al., 2015). Rescue can occur when the disassembling end reaches GTP tubulin at the damage site (Aumeier et al., 2016). Similar results have been found following protein-mediated removal of tubulin subunits in the microtubule lattice by severing proteins including spastin and katanin (Vemu et al., 2018). Using these two approaches to promote tubulin exchange at sites distal from the growing end, future studies will likely be able to gain insight into the mechanisms of microtubule rescue.

Together, studies of individual microtubule dynamics *in vitro* have provided valuable insight that has helped shape our understanding of microtubule dynamic instability. In the next section, I review structural studies of tubulin and microtubules.

1.5 The structure of microtubules

Microtubules in cells can grow to tens of microns in length. Composed of ~1,600 tubulin heterodimers per micron, a single microtubule can grow to be 10,000x larger than the subunit of which it is composed. To understand how microtubules assemble, we must understand how the subunits physically contact each other in the microtubule lattice as well as the conformational changes that accompany polymerization.

The helical structure of the microtubule polymer

In polymer form, tubulin heterodimers are organized such that two kinds of inter-dimer associations are made: lateral and longitudinal (Kirschner et al., 1974; Chrétien and Wade, 1991). Longitudinal interactions are defined by the interface of β- and α-tubulin for subunits within a single protofilament, and longitudinal interactions are formed between subunits in adjacent protofilaments (**Fig. 1.6 A**). Microtubules form a B-type lattice meaning that the interactions between subunits in adjacent protofilaments are homotypic between most protofilaments (α-tubulin contacts α-tubulin and β-tubulin contacts β-tubulin). In human cells and other eukaryotes, 13-protofilament microtubules are most commonly observed by far, although there are notable exceptions (Chaaban et al., 2017). In a typical 13-protofilament microtubule, tubulin subunits are displaced longitudinally in adjacent protofilaments, creating a 10º pitch (**Fig. 1.6 A**). This pitch generates a pattern known as a three-start helix because a helical path around the microtubule leads back to the same position three subunits higher than the starting position (Grimstone and Klug, 1966) (**Fig. 1.6 B**). By consequence of this odd-numbered helical pattern, this also

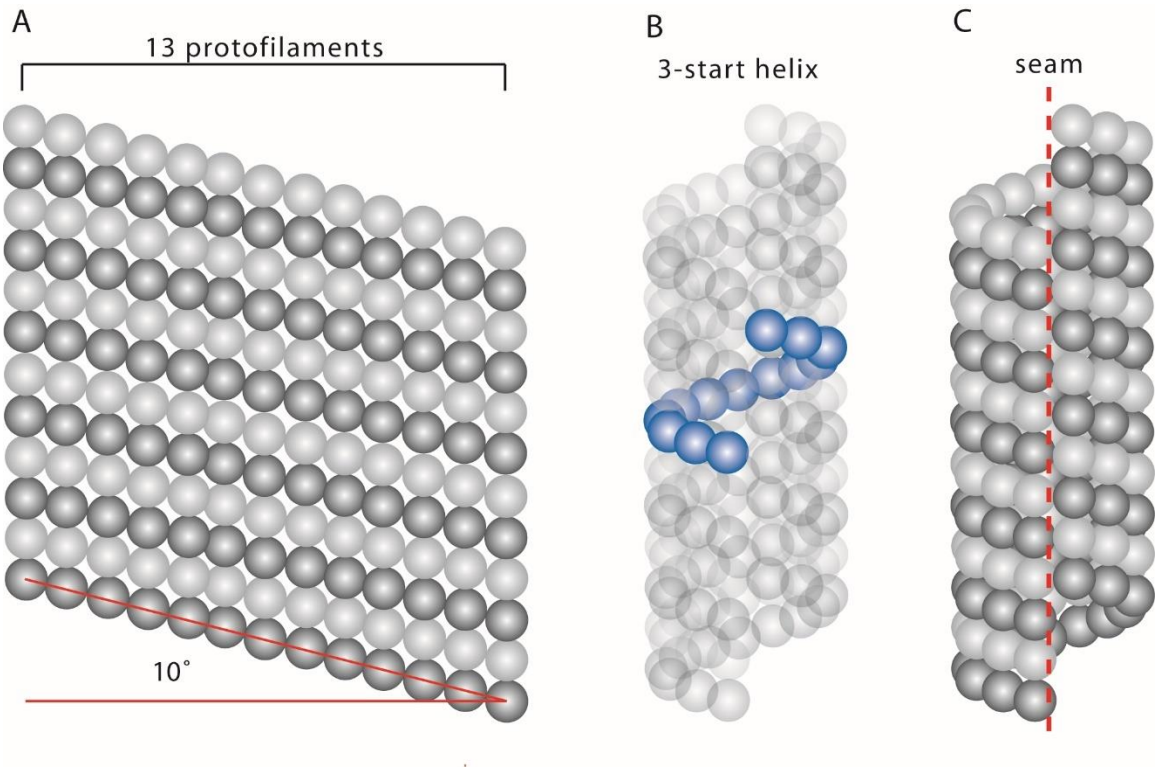

Figure 1.6. The helical structure of a 13-protofilament microtubule.

(**A**) Cartoon showing the surface lattice of a 13-protofilament microtubule, drawn as if the tube were unrolled. There is a 10º pitch between adjacent protofilaments. (**B**) Cartoon representation of a microtubule. The path around the microtubule of one row of monomers is highlighted. (**C**) Non-homotypic interactions are seen between monomers in adjacent protofilaments at the seam.

generates a microtubule "seam" at which α- and β-tubulin make non-homotypic lateral interactions (**Fig. 1.6 C**).

The functional relevance of the seam is not well understood, but structural studies suggest that it can impact the binding of microtubule-associated proteins. For example, the +TIP tracking protein EB3 binds at the interface between protofilaments except at the seam (Zhang et al., 2015). It is thought that the interactions between subunits at the seam are weaker than between other protofilaments, but whether the presence of the seam can impact parameters of dynamic instability is not known.

Tubulin curvature and implications for dynamic instability

Early cryo-electron microscopy studies of dynamic microtubules revealed that protofilaments in the lattice of microtubules are straight, but the structure of microtubule ends differs substantially whether the microtubule is growing or shrinking (Mandelkow et al., 1991). Depolymerizing microtubules appear to have curved ends in which protofilaments appear to be peeling back on themselves. Furthermore, cold depolymerization of microtubules has shown that GDP-tubulin can formed ring-like oligomers (Melki et al., 1989). The observation of curved protofilaments and oligomers led to the hypothesis that GTP-tubulin adopts a straight conformation and GDP-tubulin is curved and therefore under strain in the microtubule lattice. However, even growing microtubules are not always straight and appear to exhibit gently curving sheets at their plus-ends, suggesting that tubulin heterodimers likely undergo several conformational changes both during polymerization and depolymerization that involve the adaptation of a curved conformation (Chrétien et al., 1995).

The tendency for microtubules to spontaneously nucleate and polymerize under high tubulin concentration has made crystallizing this protein for X-ray studies challenging. The first high-resolution structure of straight tubulin in protofilaments came from studies using zinc-induced tubulin sheets (Nogales et al., 1998). High-resolution structures of curved tubulin was solved following co-crystallization of α/β heterodimers with the stathmin-like domain of Rb3, which interferes with microtubule dynamics (Gigant et al., 2000; Ravelli et al., 2004). Comparison between monomers of the same identity in the two structures revealed that both α- and β-tubulins adopt different conformations. Furthermore, the longitudinal interactions between heterodimers is also impacted. In the curved conformation, successive tubulins in a protofilament would be rotated by ~12º, which matches the ~12º radius of curvature in the rams-horn-like structures seen at depolymerizing microtubule ends (Kirschner et al., 1974).

Other structural studies have revealed that there are likely additional conformations that tubulin heterodimers can adopt during the polymerization cycle. Cryo-electron microscopy studies of microtubule ribbons assembled from GMPCPP-tubulin showed that heterodimers were arranged with a ~5 degree rotation, suggesting the presence of a possible intermediate structure between straight and curved (Wang and Nogales, 2005).

Three groups have presented high-resolution structures of GTP-tubulin bound to different proteins including stathmin/RB3, Stu2p, or DARPin (Nawrotek et al., 2011; Ayaz et al., 2012; Pecqueur et al., 2012). In all of these structures, GTP-tubulin appears to adopt a curved conformation with a ~12º rotation, inconsistent with previous models proposing that only GDP tubulin is curved. Importantly, both stathmin/Rb3 and the TOG domain of Stu2p were found to have a similar affinity for both GDP and GTP tubulin, suggesting that

it was unlikely that the binding of these proteins to GTP was inducing the curved conformation (Honnappa et al., 2003; Ayaz et al., 2012). Furthermore, the binding of tubulin to allocolchicine, a derivative of colchicine that fluoresces upon tubulin binding, is conformation-dependent, but allocolchicine affinity is independent of nucleotide state (Rice et al., 2008). Together, these structural data suggest that tubulin is curved in solution independent of nucleotide state, and that the transition to a straight conformation occurs following polymerization.

The structure of tubulin in the microtubule polymer

Solving the structure of tubulin in microtubules is crucial for understanding the conformational changes that take place in tubulin during polymerization. The presence of the microtubule seam, which breaks the helical symmetry of the microtubule lattice, has for many years presented a challenge to structural studies of tubulin subunits. In cells, 13-protofilament microtubules are common, but microtubules that spontaneously assembly *in vitro* are heterogeneous, with 9-16 protofilament microtubules observed (Pierson et al., 1978). Early reconstructions relied on the use of 15-protofilament microtubules, which do not have a seam, but due to the low abundance of these microtubules in samples, the resolution of the reconstructions were limited to ~20 Å (Arnal et al., 1996; Sosa et al., 1997).

The development of sophisticated reconstruction methods for cryo-electron microscopy along with technological improvements in electron detectors have allowed recent structures of tubulin in microtubule polymers to achieve near-atomic resolution while bound to various microtubule associated proteins and nucleotides (Nogales and

Kellogg, 2017). The first study to show high-resolution (4.7-5.6 Å) structures of microtubules assembled from bovine brain tubulin showed microtubules in three different states: GDP-bound (in dynamic microtubules), Taxol-stabilized, and GMPCPP-bound (Alushin et al., 2014). In each state, the lateral contacts between tubulin subunits are very similar. However, the inter-dimer longitudinal contact site is compacted in the GDP-tubulin state. These data support a model in which the energy from GTP hydrolysis is stored as strain in the lattice and modulated primarily at longitudinal interfaces.

Tubulin primary sequence and microtubule structure

For decades, purified tubulin was sourced from animal brain, usually of porcine or bovine origin, and was the material of choice for many of the abovementioned structural studies. However, brain tubulin is a heterogeneous mixture of tubulin heterodimers composed of various α- and β-tubulin isotypes (Banerjee et al., 1988). Further attempts to purify the mixture to obtain isotypically pure tubulin are limited by the availability of different isotypes in the tissue.

Several lines of evidence point to the non-interchangeability of tubulin isotypes, suggesting functional specialization which could manifest as differences in microtubule structure and dynamics. In insects, when a β-tubulin from moth, which forms microtubules with 15 protofilaments, was expressed in *Drosophila*, which makes microtubules with 13 protofilaments, the flies assembled microtubules with 15 protofilaments (Hoyle and Raff, 1990). This study provided compelling evidence that differences in amino acid sequence can directly impact microtubule structure. The development of methods to purify tubulin with specific amino acid sequence has aided our understanding of how changes in the

amino acid sequence of tubulin can impact microtubule stability and structure (Chaaban et al., 2018; Ti et al., 2018). I explore this topic further in chapters 2 and 3.

Through my PhD work, I examine two aspects of microtubule function: intrinsic assembly dynamics of individual microtubules *in vitro* and the function of the spindle midzone during mitosis in living cells.

Chapter 2: The structured core of human β tubulin confers isotype-specific polymerization properties

Note to readers: A closely related version of the work described below has been published in the Journal of Cell Biology (DOI: 10.1083/jcb.201603050). I performed all experiments and analysis.

2.1 Summary

Diversity in cytoskeleton organization and function may be achieved through variations in primary sequence of tubulin isotypes. Recently, isotype functional diversity has been linked to a tubulin code in which the C-terminal tail, a region of substantial sequence divergence between isotypes, specifies interactions with microtubule-associated proteins. However, it is not known whether residue changes in this region alter microtubule dynamic instability. Here, we examine recombinant tubulin with human β isotype βIIB and characterize polymerization dynamics. Microtubules with βIIB have catastrophe frequencies ~3-fold lower than those with βIII, a suppression similar to what is achieved by regulatory proteins. Further, we generate chimeric β tubulins with native tail sequences swapped between isotypes. These chimeras have catastrophe frequencies similar to the corresponding full-length construct with the same core sequence. Together, our data indicate that residue changes within the conserved β tubulin core are largely responsible for the observed isotype-specific changes in dynamic instability parameters and tune tubulin's polymerization properties across a wide range.

2.2 Introduction

Microtubules, polymers of α/β tubulin subunits, carry out a wide range of functions in eukaryotes (Desai and Mitchison, 1997; Nogales, 2000). The tubulin gene family has expanded substantially in higher eukaryotes, and the expression of different isotypes can vary according to cell identity and stage of development (Ludueña, 2013). For example, flies encode four α and four β tubulin isotypes, while humans encode at least seven α and eight β tubulin isotypes that have distinct expression profiles (Ludueña and Banerjee, 2008). In particular, βII and βIII are the major β tubulins in the brain (Banerjee et al., 1988), and βVI is limited to the hematopoietic cell lineage (Leandro-García et al., 2012; Wang et al., 1986). Recent *in vivo* studies have revealed that β tubulin isotypes have non-interchangeable roles in development. In Drosophila, when one β tubulin isotype was expressed in place of a testes-specific β tubulin, axoneme assembly and meiosis were not supported (Hoyle and Raff, 1990). In mice, embryonic knockdown of neuronal βIII expression led to neural migration defects that could not be rescued by expression of other β tubulin isotypes (Saillour et al., 2014). Together, these studies suggest that having multiple tubulin isotypes can be important for achieving diversity in function.

Differences in amino acid sequence of tubulin isotypes can impact two important aspects of tubulin function: the binding to microtubule associated proteins (MAPs), and the dynamics of microtubule polymer assembly. Numerous studies examining MAP interactions have focused on the ~25 amino acids that comprise the C-terminal 'tail' of tubulin where many post-translational modifications are found and where isotype sequence differences are concentrated (Westermann and Weber, 2003; Verhey and Gaertig, 2007). Thus it has been proposed that tubulin's C-terminal tail may establish a ‘tubulin code’ to

direct unique interactions with MAPs (Verhey and Gaertig, 2007). By contrast, it is unclear whether residue changes in tubulin's C-terminal tail sequence can directly impact microtubule polymerization dynamics. Studies using native tubulin isolated from bovine brain have shown that α/β tubulin dimers with different β isotype composition have distinct polymerization properties (Banerjee et al., 1992; Lu and Ludueña, 1994; Panda et al., 1994), which are partially altered after limited proteolysis by subtilisin (Lu and Ludueña, 1994). However, due to challenges in generating human tubulins with modified amino acid sequence from recombinant sources, the basis of the observed changes in polymerization dynamics between tubulin isotypes is still unknown.

Here, we purify recombinant tubulin heterodimers that have human β tubulin isotype 2B (βIIB) and provide the first characterization of its biochemical properties and assembly dynamics. We quantify parameters of dynamic instability and compare them to those of isotype 3 (βIII) heterodimers that we have recently examined (Ti et al., 2016). Further, we generate chimeric 'tail-swapped' tubulins by fusing the C-terminal tail domain of one isotype to the core of the other and use these proteins to dissect the basis of isotype-specific changes in dynamic instability.

2.3 Results

Purification of recombinant α/βIIB tubulin heterodimers

To determine the biochemical and polymerization properties of human β tubulin isotypes, we purified recombinant tubulin heterodimers using a protocol we have recently developed (Ti et al., 2016). This three-step procedure generated affinity tag-free recombinant protein (**Fig. 2.1 A-C**). We then used mass spectrometry to confirm the presence of human βIIB and showed that heterodimers contained an approximately equimolar mixture of human and insect α tubulin which are ~97% identical by sequence (**Fig. 2.2 A**). Efforts to tag both α and β tubulin with different affinity tags led to a substantially reduced protein yield and this strategy was not pursued further. We find our multi-step approach suitable for comparing tubulins with different β isotype compositions as done in this study. Hereafter, we refer to the purified recombinant tubulin as α/βIIB, highlighting the specific purified human β tubulin isotype.

We assessed the recombinant α/βIIB tubulin using two approaches. First, size-exclusion chromatography indicated that α/βIIB existed as a stable dimer in solution (**Fig. 2.3 A**), and eluted at a similar volume to bovine tubulin purified using standard methods (Al-Bassam et al., 2006; Gell et al., 2011). Second, we examined α/βIIB in the presence of compounds that stabilize or destabilize microtubules. We found that the protein polymerized to form microtubules in the presence of the drug Taxol (**Fig. 2.3 B**) and the slowly-hydrolyzable GTP analog, GMPCPP (**Fig. 2.3 C**). Colchicine and related analogs bind soluble tubulin at an interface between the α and β subunits and inhibit tubulin polymerization (Ravelli et al., 2004). In particular, we examined the binding of our recombinant α/βIIB protein to a colchicine analog, allocolchicine, which fluoresces only

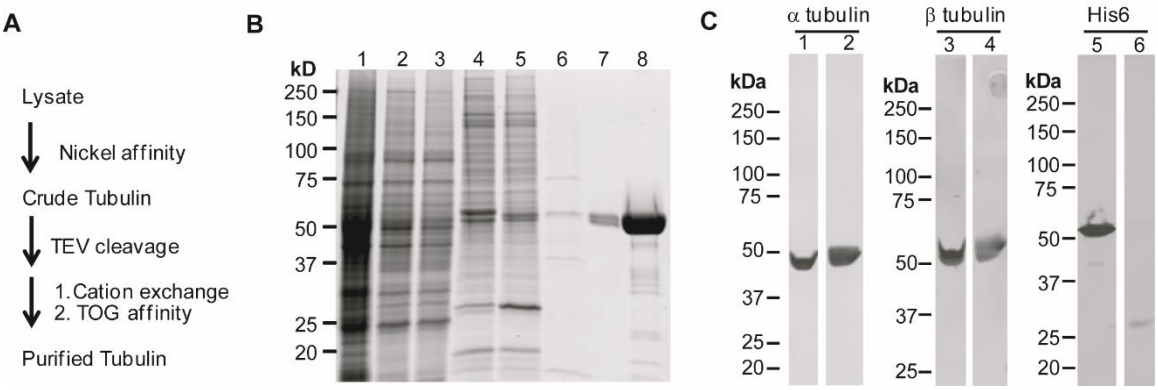

Figure 2.1. Purification of recombinant α/βIIB tubulin heterodimers.

(A) Purification scheme. (B) SDS-PAGE analysis (1, lysate; 2, supernatant; 3-5, nickel affinity: flow-through (3); elution (4); 5, elution after TEV digest (5); 6-8, TOG affinity: flow-through (6); elution (7), 20X amount in lane-7 (8)) (Coomassie stained). (C) Western blot analyses of proteins eluted from nickel affinity (lanes 1, 3, and 5) and TOG affinity (lanes 2, 4, and 6) chromatography. Antibodies against α tubulin, β tubulin, and C-terminal hexa-histidine tag are indicated.

A

```
Human a-tubulin 1B   1  MRECISIHVGQAGVQIGNACWELYCLEHGIQPDGQMPSDKTIGGGDDSFNTFFSETGAGK
Moth  a-tubulin      1  MRECISVHVGQAGVQIGNACWELYCLEHGIQPDGQMPTDKTVGGGDDSFNTFFSETGAGK
                        ****** ****************************** *** ******************
Human a-tubulin 1B  61  HVPRAVFVDLEPTVIDEVRTGTYRQLFHPEQLITGKEDAANNYARGHYTIGKEIIDLVLD
Moth  a-tubulin      61  HVPRAVFVDLEPTVVDEVRTGTYRQLFHPEQLITGKEDAANNYARGHYTIGKEIVDLVLD
                        ************** ************************************** *****
Human a-tubulin 1B 121  RIRKLADQCTGLQGFLVFHSFGGGTGSGFTSLLMERLSVDYGKKSKLEFSIYPAPQVSTA
Moth  a-tubulin    121  RIRKLADQCTGLQGFLIFHSFGGGTGSGFTSLLMERLSVDYGKKSKLEFAIYPAPQVSTA
                        ***************** ******************************** **********
Human a-tubulin 1B 181  VVEPYNSILTTHTTLEHSDCAFMVDNEAIYDICRRNLDIERPTYTNLNRLISQIVSSITA
Moth  a-tubulin    181  VVEPYNSILTTHTTLEHSDCAFMVDNEAIYDICRRNLDIERPTYTNLNRLIGQIVSSITA
                        ************************************************** ********
Human a-tubulin 1B 241  SLRFDGALNVDLTEFQTNLVPYPRIHFPLATYAPVISAEKAYHEQLSVAEITNACFEPAN
Moth  a-tubulin    241  SLRFDGALNVDLTEFQTNLVPYPRIHFPLVTYAPVISAEKAYHEQLSVAEITNACFEPAN
                        **************************** ******************************
Human a-tubulin 1B 301  QMVKCDPRHGKYMACCLLYRGDVVPKDVNAAIATIKTKRSIQFVDWCPTGFKVGINYQPP
Moth  a-tubulin    301  QMVKCDPRHGKYMACCMLYRGDVVPKDVNAAIATIKTKRTIQFVDWCPTGFKVGINYQPP
                        ***************** ********************** ********************
Human a-tubulin 1B 361  TVVPGGDLAKVQRAVCMLSNTTAIAEAWARLDHKFDLMYAKRAFVHWYVGEGMEEGEFSE
Moth  a-tubulin    361  TVVPGGDLAKVQRAVCMLSNTTAIAEAWARLDHKFDLMYAKRAFVHWYVGEGMEEGEFSE
                        ************************************************************
Human a-tubulin 1B 421  AREDMAALEKDYEEVGVDSVEGEGEEEGEEY
Moth  a-tubulin    421  AREDLAALEKDYEEVGMDSAEGEGEGA EEY
                        **** *********** ** *****   ***
```

Figure 2.2. Sequence alignment between human and insect α tubulin.

(A) Alignment of protein sequences from human α tubulin 1B (NP_006073.2) and α tubulin from insect cells (ABU94679.1). Peptide fragments that were used to estimate the relative amounts of human and insect α tubulin are labeled in red.

Figure 2.3. Characterization of recombinant α/βIIB tubulin heterodimers.

(A) Elution profiles from size-exclusion chromatography. Peak volume: 14.4 ml (α/βIIB); 14.3 ml (bovine tubulin, used as reference). Void volume (V_o) is 7 ml. (B and C) TIRF images of (B) taxol-stabilized or (C) GMPCPP microtubules. Scale bars, 3 μm. (D) SDS-PAGE analysis of tubulin sedimentation in the presence of allocolchicine (+Allo) or 3% DMSO control (-Allo). Pellet (P) and supernatant (S) fractions are indicated. (E and F) Equilibrium binding curve for α/βIIB with allocolchicine from (E) one experiment and (F) average from three independent experiments. K_d = 1.8 ± 0.42 μM (n=3, mean ± SD).

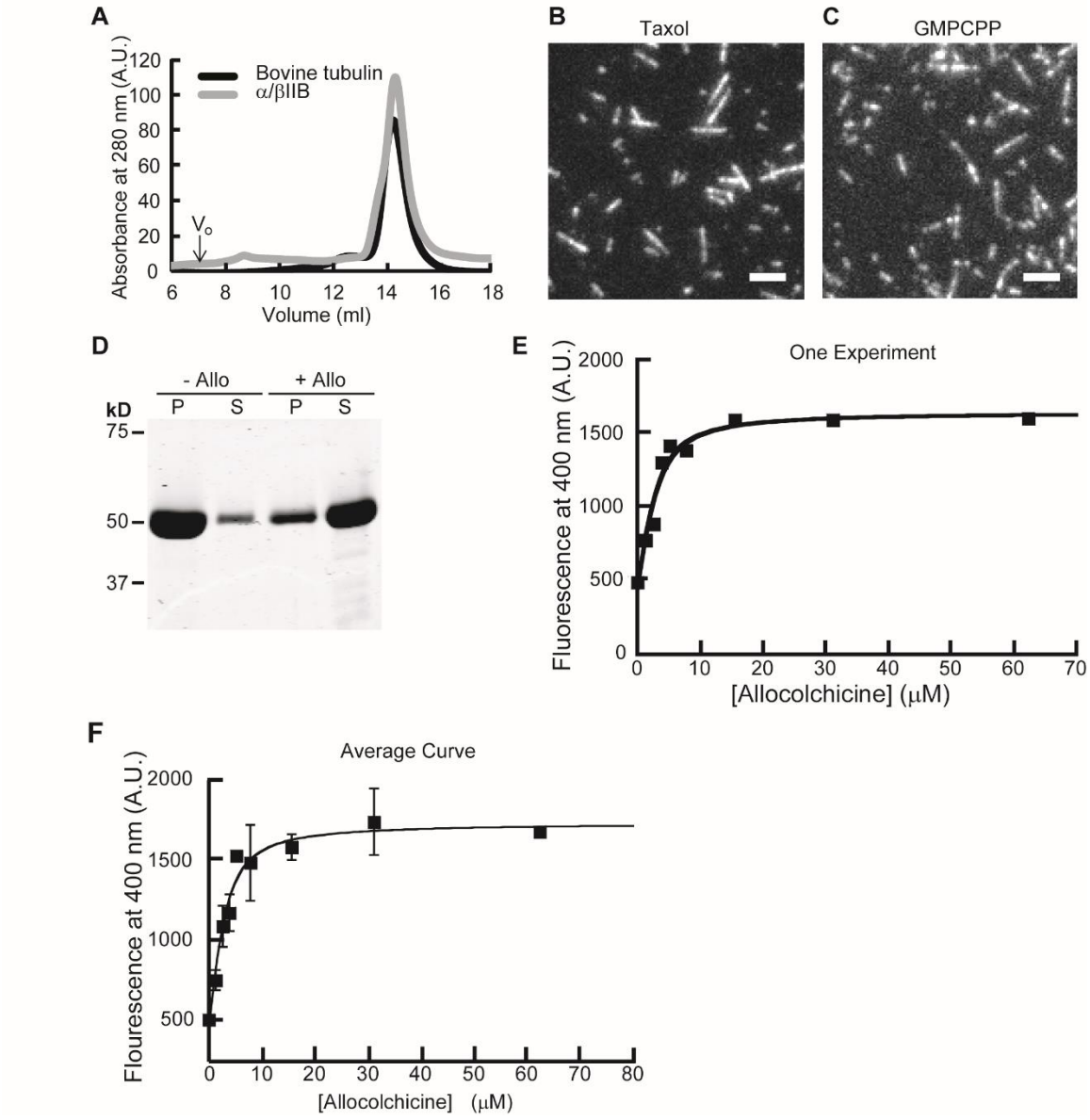
A
Absorbance at 280 nm (A.U.)
120
100
80
60
40
20
0
Bovine tubulin
α/βIIB
Vo
6
8
10
12
14
16
18
Volume (ml)
B
Taxol
C
GMPCPP
D
- Allo
+ Allo
kD
P
S
P
S
75
50
37
E
One Experiment
Fluorescence at 400 nm (A.U.)
2000
1500
1000
500
0
0
10
20
30
40
50
60
70
[Allocolchicine] (μM)
F
Average Curve
Flourescence at 400 nm (A.U.)
2000
1500
1000
500
0
10
20
30
40
50
60
70
80
[Allocolchicine] (μM)

upon binding soluble tubulin and allows for a direct readout of the interaction (Hastie, 1989; Medrano et al., 1989). We first confirmed that allocolchicine can inhibit the assembly of α/βIIB microtubules (**Fig. 2.3 D**). We next determined equilibrium binding and find that α/βIIB tubulin binds allocolchicine with a low-micromolar affinity (K_d = 1.8 ± 0.42 μM, n= 3) (**Fig. 2.3 E-F**), similar to that reported for bovine brain tubulin (Rice et al., 2008). Together, these data indicate that our recombinant α/βIIB protein shares overall properties similar to those of bovine tubulin purified using conventional methods.

Polymerization properties of recombinant α/βIIB tubulin heterodimers

To analyze polymerization dynamics of recombinant α/βIIB, we employed a TIRF-based single filament assay (**Fig. 2.4 A**). As a template for microtubule formation, we used GMPCPP-stabilized 'seeds' assembled from α/βIIB tubulin. We then applied solutions of soluble tubulin and observed microtubule assembly off of these 'seeds' over a range of tubulin concentrations (**Fig. 2.4 B and D**). To quantify dynamic instability parameters, we generated kymographs from the time lapse images of growing microtubules (**Fig. 2.4 C and E**). Even at the lowest tubulin concentration used (6 μM), we observed growth off of the plus-ends of all filaments examined. By contrast, assembly of microtubule polymer was rarely observed off of the minus-ends at this concentration and only occasionally observed at the highest concentration used (13 μM), therefore we did not quantify the polymerization properties of tubulin at this end.

We measured the average polymerization rate at plus-ends of microtubules assembled from α/βIIB tubulin and found this rate increased with free tubulin concentration

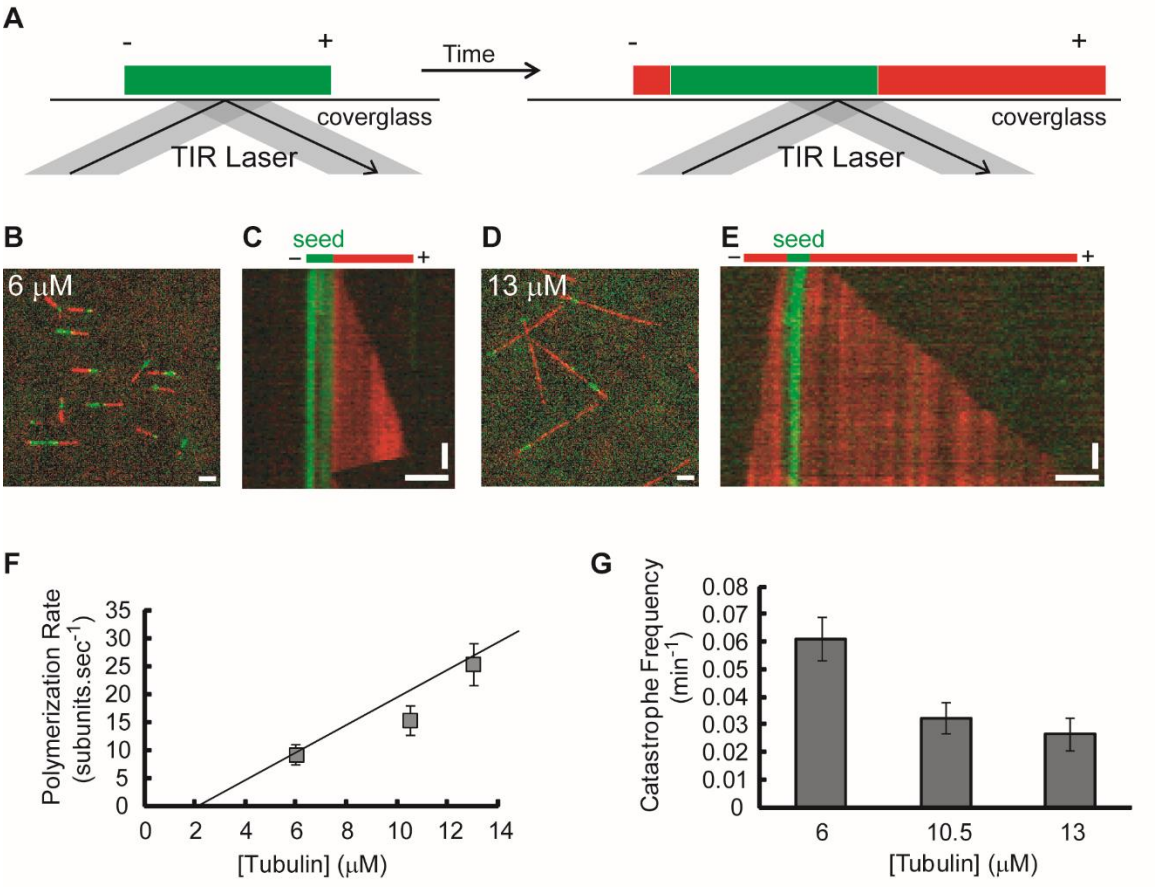

Figure 2.4. Single filament TIRF analysis of α/βIIB tubulin polymerization properties.

(A) TIRF assay schematic. Microtubule extensions (red) and GMPCPP- 'seeds' (green) are shown with plus-ends (+) and minus-ends (-) indicated. TIRF image overlays (B and D) and kymographs (C and E) of microtubules extensions (red) growing from 'seeds' (green) (total tubulin: 6 μM (B and C);13 μM (D and E)). (F and G) Plus-end polymerization rates (F) and catastrophe frequencies (G) for microtubules composed of α/βIIB at different free tubulin concentrations. Table 2.1 summarizes these measurements.

(**Fig. 2.4F and Table 1**). The measured growth rates were close to the reported values for α/βIII (Ti et al., 2016) and for purified bovine brain tubulin (Walker et al., 1988). We then fit the data to a simple 1-D model (Oosawa, 1970) whose slope and intercept are the apparent association (k_+) and dissociation (k_-) rate constants of tubulin subunits, respectively ($k_+ = 1.9 \pm 0.5\ \mu M^{-1}\ s^{-1}$ and $k_- = 2.6 \pm 4.2\ s^{-1}$).

We next measured the frequency of catastrophe, the transition from a state of filament growth to a state of rapid shrinkage. Microtubules assembled from α/βIIB heterodimers underwent a catastrophe event infrequently, and we observed a moderate decrease in catastrophe frequency as tubulin concentration was increased from 6 μM to 13 μM (**Fig. 2.4 G**). We measured a frequency of $0.03 \pm 0.006\ min^{-1}$ at a tubulin concentration (10.5 μM) close to physiologic levels. We rarely observed rescue events (the transition from rapid shortening to relatively slow growth) under our experimental conditions and did not analyze this parameter. When we compared our analysis of recombinant α/βIIB tubulin with that of recombinant β tubulin isotype 3 (α/βIII) (Ti et al., 2016), we observed key differences. Notably, the catastrophe frequency for α/βIIB was 1.5- to 3-fold lower than that of α/βIII at all tubulin concentrations tested (Ti et al., 2016) (p-value <0.02 at each concentration).

Tubulin in cells is a mixture of multiple isoforms of β tubulin. In particular, bovine brain β tubulin has been shown to be a mixture of at least four isotypes (β2, β3, β4, and β1 detected at 58%, 25%, 13%, and 3%, respectively) (Banerjee et al., 1988). Therefore, we mixed α/βIIB and α/βIII heterodimers and analyzed polymerization dynamics (**Fig 2.5 A-H).** At equal ratios of α/βIIB and α/βIII tubulin (10.5 μM total tubulin), microtubules readily polymerized off of GMPCPP seeds (**Fig. 2.5 B**). The polymerization rate of these

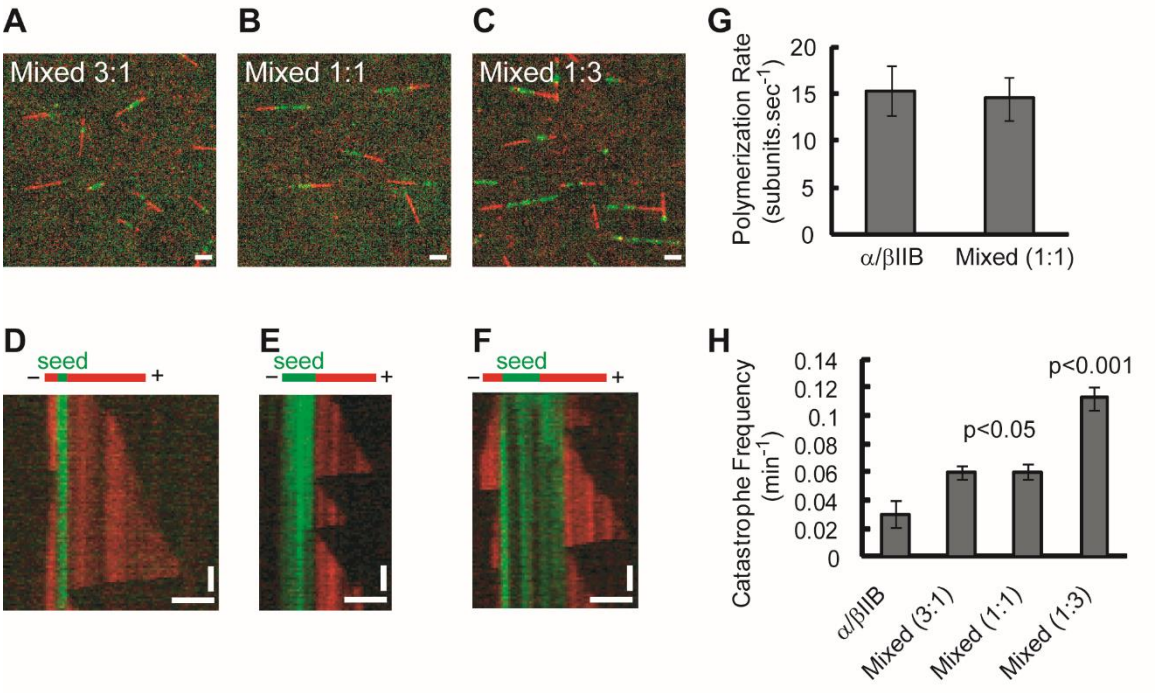

Figure 2.5. Single filament TIRF analysis of mixed α/βIIB and α/βIII tubulin polymerization properties.

(A) Overlay images (A-C) and kymographs (D-F) of mixed α/βIIB and α/βIII microtubules (α/βIIB: α/βIII ratio is 3:1 (A and D), 1:1 (B and E), or 1:3 (C and F)) (total tubulin: 10.5 μM). (G and H) Plus-end polymerization rate (G) and catastrophe frequency (H) for 'mixed' microtubules (α/βIIB: α/βIII ratio is 1:1, total tubulin: 10.5 μM) with α/βIIB shown as reference. The data were pooled from at least two independent experiments. Scale bars: 3 μm (horizontal), 2 min (vertical). Error bars are SD. For catastrophe frequency (f_{cat}), SD were calculated as $f_{cat}/\sqrt{n}$ (assuming a Poisson distribution), where n is the number of catastrophe events. Table 2.1 summarizes these measurements.

'mixed' microtubules (14 ± 2 subunit.sec^{-1}) was close to that of α/βIIB microtubules (15 ± 3 subunit.sec^{-1}) (**Fig. 2.5 G**) and α/βIII microtubules (Ti et al., 2016) at the same tubulin concentration. This suggests that the two isotypes can indeed co-polymerize. If they did not, the expected polymerization rate would be ~7-8 subunit.sec^{-1} as the effective concentration would be 5.25 μM for each isotype. The catastrophe frequency at filament plus-ends was 0.06 ± 0.01 min^{-1} at 10.5 μM total tubulin concentration (**Fig. 2.5 H**). This value is intermediate between that for α/βIIB microtubules (0.03 ± 0.01 min^{-1}) (**Fig. 2.5 H**) and that for α/βIII microtubules (Ti et al., 2016). Together, our data indicate that the dynamics of microtubules assembled from mixed tubulin populations depends on the contribution of each isotype, and that mixing gives a catastrophe frequency intermediate between what is observed for either isotype alone.

Characterization of recombinant tubulins containing human β tubulin chimeras

To examine whether residue changes within tubulin's C-terminal tail, which are proposed to specify interactions with MAPs (Sirajuddin et al., 2014), also confer the observed isotype-specific catastrophe frequencies, we generated chimeric β tubulin constructs with the C-terminal tails 'swapped' (**Fig. 2.6 A**). We designated the 'core' region (aa 1-427) to be equal to the length of tubulin protein resolved in a recent structural study (Alushin et al., 2014), and the 'tail' region to be the remaining C-terminal amino acids (aa 428-445 in βIIB, or 428-450 in βIII). We co-expressed one of the two chimeric β tubulins fused to a cleavable hexa-histidine tag along with human β isotype 1B in insect cells and generated the following two heterodimers - 'α/βIIB-tail-III' (βIIB core and βIII tail) and 'α/βIII-tail-IIB' (βIII core with βIIB tail) (**Fig. 2.6 B**).

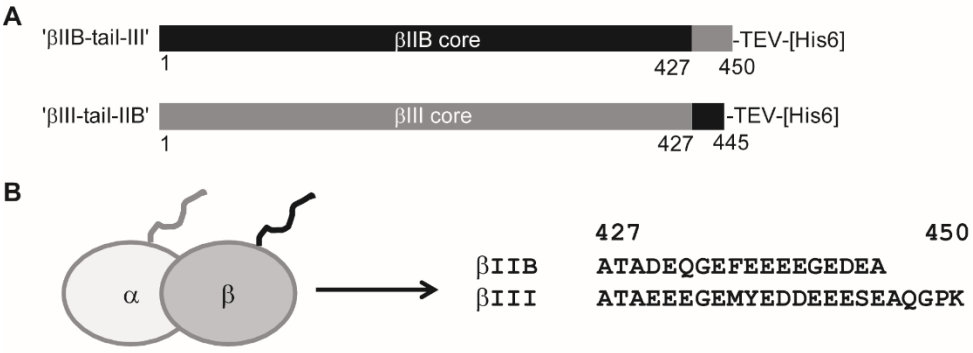

C

Percent Identity Matrix - created by Clustal2.1

		βVI	βV	βIII	βIVA	βIIA	βIIB	βIVB	βI
1: βVI	|NM_030773.3|	100.00	78.03	77.33	78.60	78.43	78.65	78.43	78.60
2: βV	|NM_032525.2|	78.03	100.00	92.38	91.89	90.34	90.56	90.79	90.77
3: βIII	|NM_006086.3|	77.33	92.38	100.00	91.67	91.46	91.69	92.81	92.57
4: βIVA	|NM_006087.3|	78.60	91.89	91.67	100.00	94.59	95.05	97.97	96.61
5: βIIA	|NM_001069.2|	78.43	90.34	91.46	94.59	100.00	99.55	96.40	95.05
6: βIIB	|NM_178012.4|	78.65	90.56	91.69	95.05	99.55	100.00	96.85	95.50
7: βIVB	|NM_006088.5|	78.43	90.79	92.81	97.97	96.40	96.85	100.00	97.52
8: βI	|NM_178014.3|	78.60	90.77	92.57	96.61	95.05	95.50	97.52	100.00

Figure 2.6. Design of chimeric β tubulin constructs.

(A) Design of 'tail-swapped' β tubulin constructs, with amino acid sequence derived from α/βIIB (black) and α/βIII (grey). (B) Cartoon of tubulin heterodimer indicating β tubulin C-terminal tail (black). Amino acid sequences from the C-terminus of βIIB and βIII are shown. (C) Percent identity matrix for human β tubulin isotypes.

Figure 2.7. Characterization of chimeric β tubulin constructs. (A) SDS-PAGE analysis (1, Nickel affinity elution; 2, TOG affinity elution) (Coomassie stained). (B) Protein elution profiles from size-exclusion chromatography. Peak volume: 14.2 ml (α/βIIB-tail-III); 14.1 ml (α/βIII-tail-IIB). Void volume (V_o) is 7 ml. (C-D) Western blot (WB) analyses of proteins eluted from nickel affinity (lanes 1, 3, and 5) and TOG affinity (lanes 2, 4, and 6) chromatography for (C) α/βIIB-tail-III and (D) α/βIII-tail-IIB. Antibodies against α tubulin, β tubulin, and C-terminal hexa-histidine tag are indicated. (E-F) TIRF images of (E) Taxol-stabilized or (F) GMPCPP microtubules. Scale bar, 3μm.

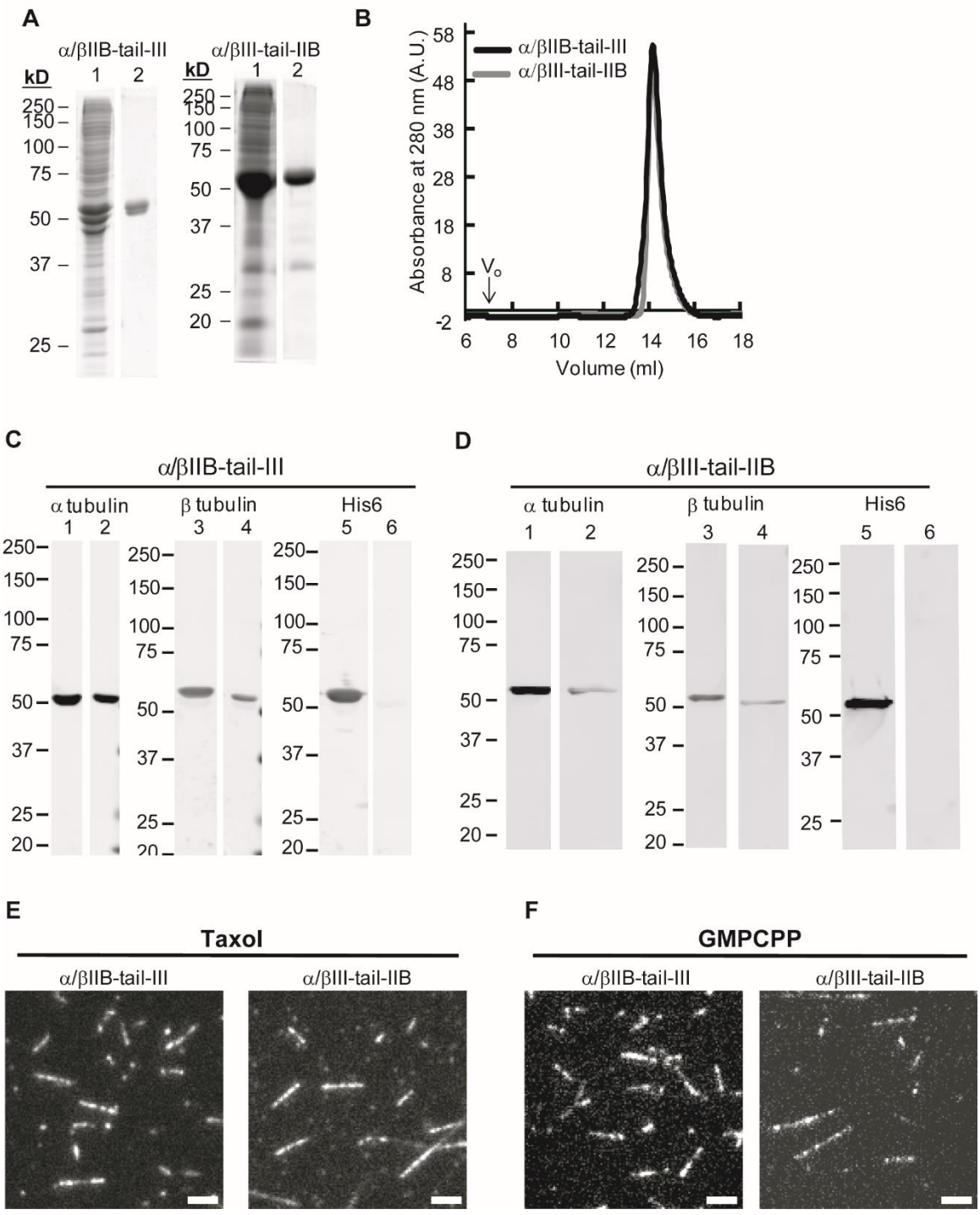
A
α/βIIB-tail-III
α/βIII-tail-IIB
kD
1
2
250
150
100
75
50
37
25
20
B
α/βIIB-tail-III
α/βIII-tail-IIB
Absorbance at 280 nm (A.U.)
58
48
38
28
18
8
-2
Vo
6
8
10
12
14
16
18
Volume (ml)
C
α/βIIB-tail-III
α tubulin
β tubulin
His6
1
2
3
4
5
6
D
α/βIII-tail-IIB
α tubulin
β tubulin
His6
1
2
3
4
5
6
E
Taxol
α/βIIB-tail-III
α/βIII-tail-IIB
F
GMPCPP
α/βIIB-tail-III
α/βIII-tail-IIB

Using our purification protocol, we generated affinity tag-free recombinant chimeric tubulin heterodimers that were of similar purity to that of α/βIIB (**Fig. 2.7 A-D**). Size-exclusion chromatography analysis indicated that the α/βIIB-tail-III and α/βIII-tail-IIB proteins existed as stable dimers in solution and eluted at a volume similar to the full-length α/βIIB (**Fig. 2.7 B** and **Fig. 2.3 A**). As with the full-length α/βIIB tubulin, we analyzed the chimeric proteins using a TIRF microscopy-based assay. We showed that both chimeric tubulins assembled readily into microtubules in the presence of Taxol (**Fig. 2.7 E**) and GMPCPP (**Fig. 2.7 F**). These experiments indicated that the chimeric tubulins formed stable dimers and polymerized under standard conditions.

Polymerization properties of recombinant tubulins containing β tubulin chimeras

To determine the intrinsic dynamic properties of recombinant tubulin heterodimers containing chimeric β tubulins, we used the same single filament TIRF assays used to analyze the full-length α/βIIB construct (**Fig. 2.4 A**). We first used GMPCPP-stabilized seeds assembled from α/βIIB-tail-III and applied solutions composed of different concentrations of α/βIIB-tail-III onto the seeds. In separate experiments, we examined growth of α/βIII-tail-IIB tubulin off of α/βIII-tail-IIB seeds.

In the case of α/βIIB-tail-III tubulin, we frequently observed growth at only one of the two ends of the seed (**Fig. 2.8 A-D**), as was noted for full-length α/βIIB. At the plus-ends, the rate of polymerization for microtubules assembled from α/βIIB-tail-III increased with greater concentration of free tubulin (**Fig. 2.8 I** and **Table 2.1**). The apparent association (k_+) and dissociation (k_-) rate constants for α/βIIB-tail-III ($k_+ = 2.0 \pm 0.4\ \mu M^{-1}$

Figure 2.8. Single filament TIRF analysis of chimeric β tubulins.

TIRF image overlays (A, C, E and G) and kymographs (B, D, F and H) showing microtubules extensions (red) growing from GMPCPP seeds (green) assembled with α/βIIB-tail-III (A-D) or α/βIII-tail-IIB (E-H). (I and J) Plus-end polymerization rates (I) and catastrophe frequencies (J) for chimeric α/βIIB-tail-III or α/βIII-tail-IIB microtubules at different free tubulin concentrations. Catastrophe frequency measurements for full-length α/βIIB (blue dashed line) and α/βIII (red dashed line) is shown as reference. The data were pooled from at least three independent experiments. Error bars are SD. For catastrophe frequency (f_{cat}), SD were calculated as $f_{cat}/\sqrt{n}$ (assuming a Poisson distribution), where n is the number of catastrophe events. Scale bars: 3μm (horizontal), 2 min (vertical). Table 2.1 summarizes these measurements.

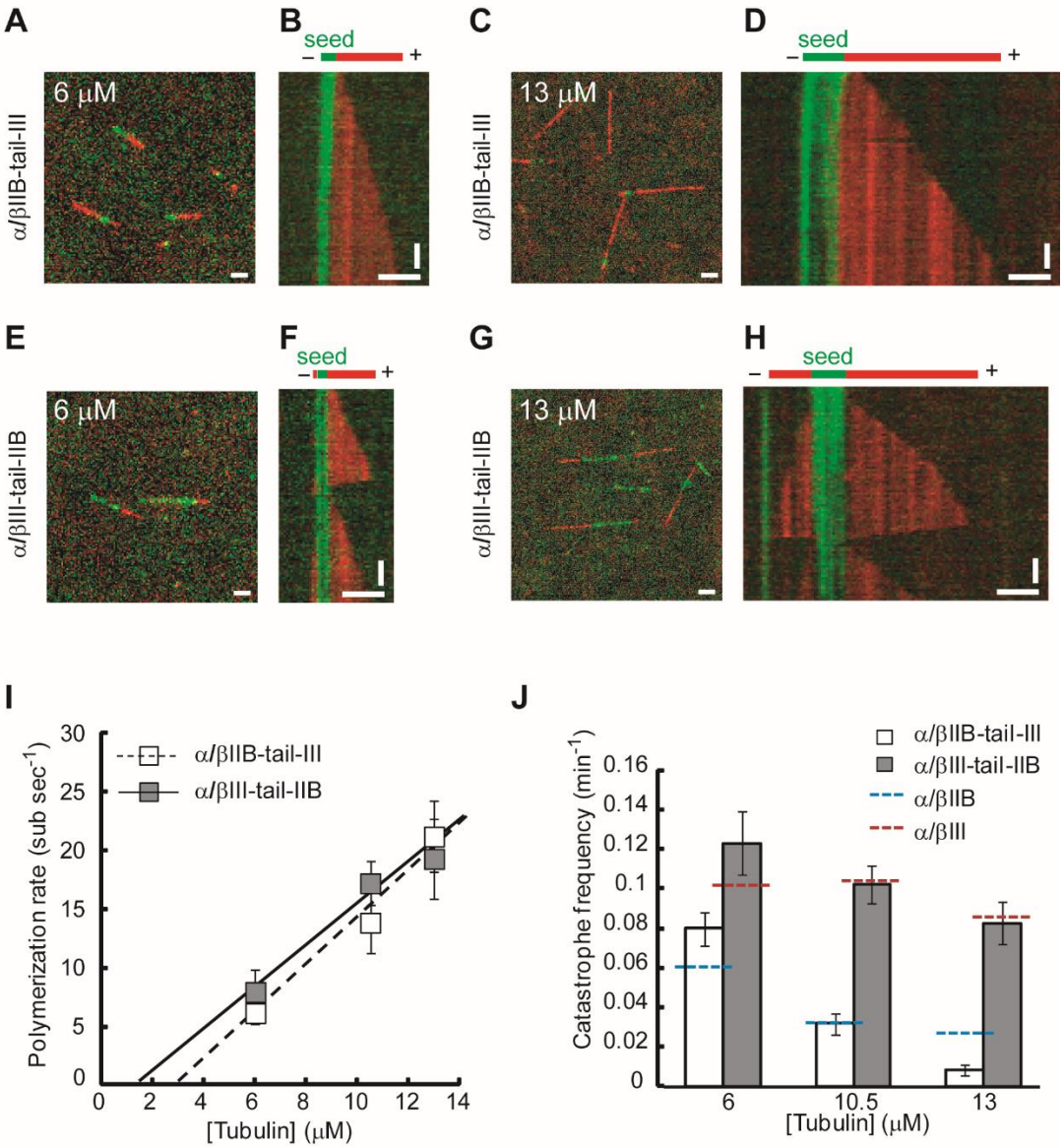
A
B
C
D
E
F
G
H
I
J
6 μM
13 μM
α/βIIB-tail-III
α/βIII-tail-IIB
seed
–
+
Polymerization rate (sub sec^{-1})
[Tubulin] (μM)
α/βIIB
α/βIII
Catastrophe frequency (min^{-1})

s^{-1} and $k_- = 5.5 \pm 2.7\ s^{-1}$) were close to those measured for α/βIIB and for α/βIII (Ti et al., 2016).

By contrast, in a solution of α/βIII-tail-IIB tubulin, assembly frequently occurred off both ends of seeds at all tubulin concentrations (**Fig. 2.8 E-H**). This was consistent with what we found for full-length recombinant α/βIII, which grows frequently at both seed ends under similar experimental conditions (Ti et al., 2016). To compare rates between isotypes, we focused on the faster-growing plus-end. The polymerization rate of microtubules assembled from α/βIII-tail-IIB tubulin also increased with increasing concentrations of free tubulin (**Fig. 2.8 I**). The apparent association (k_+) and dissociation (k_-) rate constants for α/βIII-tail-IIB ($k_+ = 1.8 \pm 0.5\ \mu M^{-1}\ s^{-1}$ and $k_- = 2.4 \pm 4.2\ s^{-1}$) were close to those of both full-length α/βIIB and full-length α/βIII. These data indicate that each of the chimeric β tubulin constructs can elongate into microtubule polymer at rates close to those measured for each of the full-length wild-type proteins α/βIIB and α/βIII.

We next analyzed catastrophe frequency, the dynamic instability parameter that differs substantially between α/βIIB and α/βIII. For α/βIIB-tail-III microtubules, the catastrophe frequencies are close to those of the full-length α/βIIB at the same tubulin concentrations (**Fig. 2.8 J** and **Fig. 2.4 G**). Next, we measured the catastrophe frequencies of microtubules assembled from α/βIII-tail-IIB tubulin and found them to be ~1.5- to 3-fold higher than those of α/βIIB-tail-III microtubules over a range of tubulin concentrations (**Fig 2.8 J** and **Table 2.1**). These catastrophe frequencies of α/βIII-tail-IIB microtubules were close to the reported catastrophe frequencies of microtubules assembled from full-length α/βIII (**Fig. 2.8 J** and **Table 2.1**). Together, these data indicate that the amino acid

substitutions within the structured core are crucial for establishing isotype-specific parameters of dynamic instability.

Table 2.1. Dynamic instability parameters for full-length wild-type tubulins and chimeric tubulins. Table includes data presented in **Fig. 2.4 F** and **G**, **Fig. 2.5 G** and **H**, and **Fig. 2.8 I** and **J**. Mean ± SD are shown. n represents the number of filaments analyzed (for polymerization rate) or catastrophe events (for catastrophe frequency). Asterisks indicate data from (Ti et al., 2016).

Total tubulin concentration	**Recombinant protein**	**Polymerization rate (subunit.sec^{-1})**	**Catastrophe frequency (min^{-1})**
6 μM	α/βIIB	9 ± 2 (n = 70)	0.06 ± 0.008 (n = 60)
	α/βIIB-tail-III	6 ± 1 (n = 87)	0.08 ± 0.008 (n = 92)
	α/βIII-tail-IIB	8 ± 2 (n = 37)	0.12 ± 0.02 (n = 58)
	α/βIII*	8 ± 3 (n = 77)	0.10 ± 0.01 (n = 105)
10.5 μM	α/βIIB	15 ± 3 (n = 70)	0.03 ± 0.006 (n = 33)
	α/βIIB-tail-III	14 ± 3 (n = 81)	0.03 ± 0.005 (n = 37)
	α/βIII-tail-IIB	17 ± 2 (n = 88)	0.10 ± 0.01 (n = 115)
	α/βIII*	16 ± 6 (n = 75)	0.10 ± 0.01 (n = 104)
	Mixed (3:1) (α/βIIB: α/βIII)	n.d.	0.05 ± 0.008 (n = 41)
	Mixed (1:1) (α/βIIB: α/βIII)	14 ± 2 (n = 79)	0.06 ± 0.007 (n = 65)
	Mixed (1:3) (α/βIIB: α/βIII)	n.d.	0.12 ± 0.009 (n = 153)
13 μM	α/βIIB	25 ± 4 (n = 52)	0.03 ± 0.006 (n = 20)
	α/βIIB-tail-III	21 ± 3 (n = 49)	0.008 ± 0.003 (n = 9)
	α/βIII-tail-IIB	19 ± 3 (n = 53)	0.08 ± 0.01 (n = 62)
	α/βIII*	19 ± 4 (n = 57)	0.09 ± 0.01 (n = 68)

2.4 Discussion

Our studies suggest that the differences in dynamic instability for microtubules assembled from each of the two tubulins can be attributed in large part to varied catastrophe frequency. The suppression of catastrophe in α/βIIB microtubules observed *in vitro* is on the order of what can be achieved by regulatory proteins in cells, such as TPX2, and by microtubule-stabilizing drugs, such as Taxol (Mohan et al., 2013; Wieczorek et al., 2015). Human tubulins βIIB and βIII differ in amino acid identity at ~9% of residues within the ~450 amino acid polypeptide, and the short ~25 residue C-terminal tail carries a large fraction (15 out of 42) of the total residue changes (**Fig. 2.9 A**). Our analyses of chimeric 'tail-swapped' tubulins suggest that of these 42 non-identical residues, it is those within the structured core of tubulin that are largely responsible for the different dynamics. Recent studies examining the effects of residue mutations in tubulin's intermediate domain (Geyer et al., 2015) and kinesin-binding site (Ti et al., 2016) are beginning to reveal how subtle allostery within the tubulin heterodimer impacts microtubule assembly dynamics. Given that there are 27 amino acid differences between the βIIB and βIII isotypes within the tubulin core, and that each may affect long-range communication across the dimer, structure or sequence alone are not likely to prioritize which residues should be examined. Additional studies will be needed to identify which of the 27 amino acid differences, alone or in combination with other residues, specify the observed differences in dynamic instability.

There are five β tubulins expressed in the brain (Banerjee et al., 1988; Leandro-García et al., 2010). The core sequence of βIIB shares the least amount of similarity to that

Figure 2.9. Alignment of βIII and βIIB amino acid sequence.

(A) Secondary structure topology map corresponds to features derived from PDB listing 3J6E. Residues on β tubulin within 3Å of intra-tubulin (orange stars), longitudinal (purple stars), or lateral (blue stars) contacts or the GMPCPP binding site (black stars) are indicated. Residues that differ between isotypes βIII and βIIB are labeled in red.

A

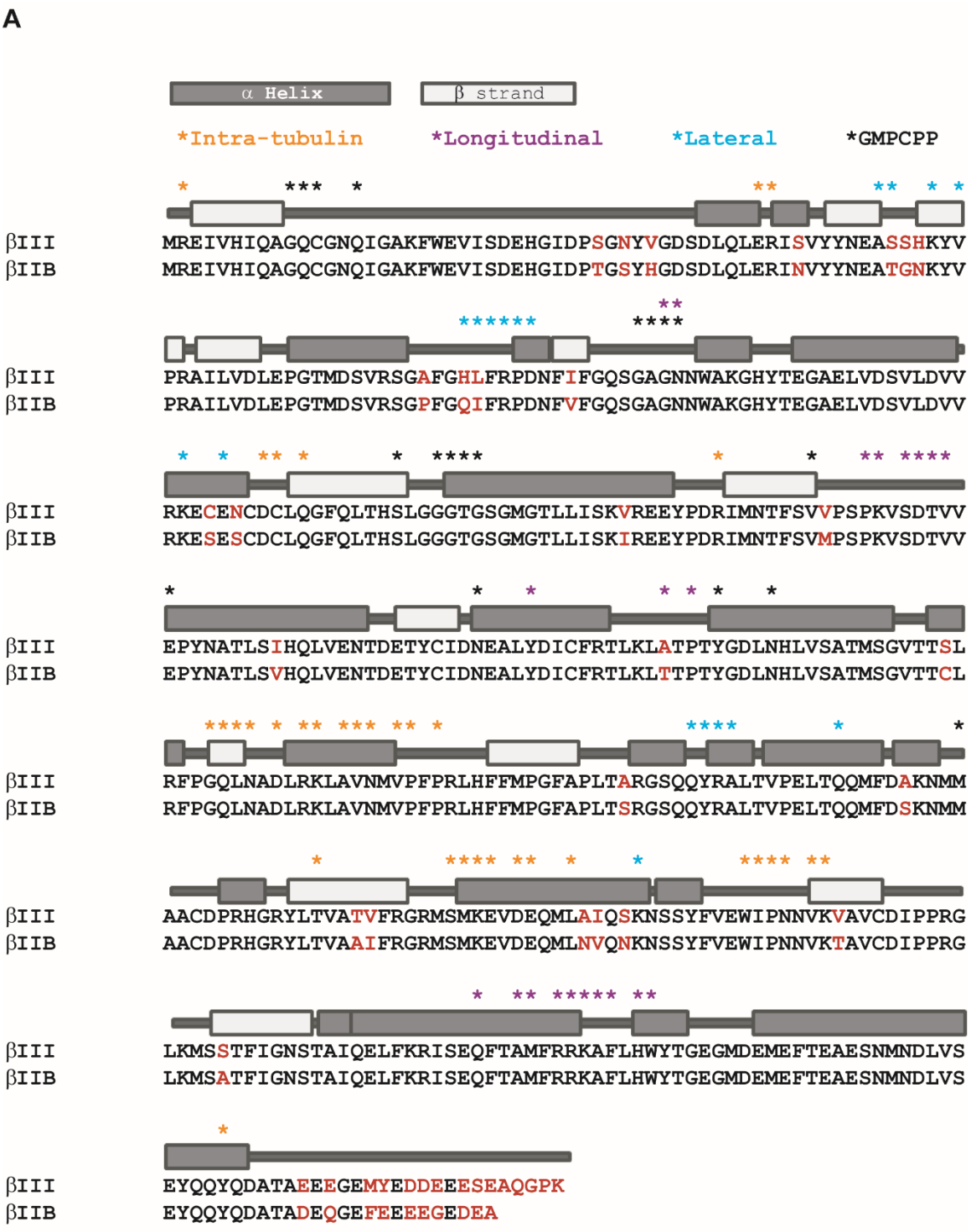
α Helix
β strand
*Intra-tubulin
*Longitudinal
*Lateral
*GMPCPP
βIII MREIVHIQAGQCGNQIGAKFWEVISDEHGIDPSGNYVGDSDLQLERISVYYNEASSHKYV
βIIB MREIVHIQAGQCGNQIGAKFWEVISDEHGIDPTGSYHGDSDLQLERINVYYNEATGNKYV
βIII PRAILVDLEPGTMDSVRSGAFGHLFRPDNFIFGQSGAGNNWAKGHYTEGAELVDSVLDVV
βIIB PRAILVDLEPGTMDSVRSGPFGQIFRPDNFVFGQSGAGNNWAKGHYTEGAELVDSVLDVV
βIII RKECENCDCLQGFQLTHSLGGGTGSGMGTLLISKVREEYPDRIMNTFSVVPSPKVSDTVV
βIIB RKESESCDCLQGFQLTHSLGGGTGSGMGTLLISKIREEYPDRIMNTFSVMPSPKVSDTVV
βIII EPYNATLSIHQLVENTDETYCIDNEALYDICFRTLKLATPTYGDLNHLVSATMSGVTTSL
βIIB EPYNATLSVHQLVENTDETYCIDNEALYDICFRTLKLTTPTYGDLNHLVSATMSGVTTCL
βIII RFPGQLNADLRKLAVNMVPFPRLHFFMPGFAPLTARGSQQYRALTVPELTQQMFDAKNMM
βIIB RFPGQLNADLRKLAVNMVPFPRLHFFMPGFAPLTSRGSQQYRALTVPELTQQMFDSKNMM
βIII AACDPRHGRYLTVATVFRGRMSMKEVDEQMLAIQSKNSSYFVEWIPNNVKVAVCDIPPRG
βIIB AACDPRHGRYLTVAAIFRGRMSMKEVDEQMLNVQNKNSSYFVEWIPNNVKTAVCDIPPRG
βIII LKMSSTFIGNSTAIQELFKRISEQFTAMFRRKAFLHWYTGEGMDEMEFTEAESNMNDLVS
βIIB LKMSATFIGNSTAIQELFKRISEQFTAMFRRKAFLHWYTGEGMDEMEFTEAESNMNDLVS
βIII EYQQYQDATAEEEGEMYEDDEEESEAQGPK
βIIB EYQQYQDATADEQGEFEEEEGEDEA

of βIII compared to the other isotypes expressed in the tissue (Leandro-García et al., 2010) (**Fig. 2.6 C**). We hypothesize that these two tubulin isotypes establish the range of potential catastrophe frequencies of neuronal microtubules. In addition, our data indicate that recombinant α/βIIB and α/βIII tubulin can co-polymerize and form microtubules comprised of 'mixed' isotypes, which have catastrophe frequencies intermediate between those measured for microtubules composed of only one tubulin. Based on intrinsic polymerization properties alone and a simple model (Verde et al., 1992), the average length of microtubules assembled from α/βIIB would be ~3 times longer than those assembled from α/βIII (see Materials and Methods), and the average length of 'mixed' microtubules would be intermediate. Thus, microtubule dynamics could be 'tuned' to have different catastrophe frequencies by varying the ratio of different isotypes in cells. Additional functional specialization would come through interactions with MAPs and via post-translational modifications.

Chapter 3: Mutations in human tubulin proximal to the kinesin binding site alter dynamic instability at microtubule plus- and minus-ends

Note to readers: Some of the work described below has been included in a manuscript published in the Developmental Cell (DOI: 10.1016/j.devcel.2016.03.003). Here, I include only experiments and analysis that I personally participated in.

3.1 Summary

The assembly of microtubule-based cellular structures depends on regulated tubulin polymerization and directional transport. Here, we purify and characterize tubulin heterodimers that have human β-tubulin isotype III (βIII), as well as heterodimers with one of two β-tubulin mutations (D417H or R262H). Both point mutations are proximal to the kinesin-binding site and have been linked to an ocular motility disorder in humans. Compared to wild-type, microtubules with these mutations are substantially more stable, reflected in decreased catastrophe frequencies. Examination of the assembly dynamics and MAP binding properties of microtubules assembled from mixtures of wild-type and mutant tubulins reveals that these mutations have dose-dependent effects on microtubule function. Together, our findings reveal how residues on the surface of microtubules, distal from the GTP-hydrolysis site and inter-subunit contacts, can alter polymerization dynamics at the plus- and minus-ends of microtubules.

3.2 Introduction

Heterodimers of α/β-tubulin undergo guanosine triphosphate (GTP)-dependent polymerization to form microtubules, cytoskeletal filaments essential for diverse cellular processes including neuronal transport, cell migration, and cell division (Desai and Mitchison, 1997; Heald and Khodjakov, 2015; Kapitein and Hoogenraad, 2015). The proper organization of microtubules depends on dynamic instability, the stochastic transitions of the microtubule between growth and shrinkage, and microtubule-associated proteins (MAPs) that can step along these filaments to transport cargoes or regulate filament polymerization dynamics (Heald and Khodjakov, 2015; Nogales and Zhang, 2016). Consistent with these basic functions, mutations in tubulin or MAPs that disrupt MAP-microtubule interactions can lead to defective cytoskeletal architectures and have been linked to disease (Hirokawa et al., 2009; Niwa et al., 2013; Tischfield et al., 2011).

We now have good structural models for tubulin heterodimers, microtubules, and how motor and non-motor MAPs interact with conserved amino acids on the surface of the hollow tube-like filament (Nogales and Zhang, 2016). MAPs such as the end-binding (EB) proteins that regulate microtubule polymerization dynamics bind tubulin subunits at sites proximal to the GTP-binding pocket of tubulin to sense and modulate changes in nucleotide states that directly contribute to polymerization dynamics (Akhmanova and Steinmetz, 2010; Maurer et al., 2012). In contrast, MAPs such as kinesins that move directionally along the microtubule lattice interact with surface-exposed residues that are distal from tubulin's GTP-binding site and the contact regions between different subunits (Nogales and Zhang, 2016). Based on structural data alone, we would not expect these surface residues to be involved in modulating microtubule polymerization dynamics. However, the

effect of mutating residues proximal to the kinesin-binding site on parameters of dynamic instability or on tubulin and microtubule conformation is not known.

Seven α- and eight β-tubulin isotypes have been identified in humans (Ludueña and Banerjee, 2008). The distribution of these isotypes varies across different tissues, with β-tubulin isotype III (βIII) expression mainly limited to developing and mature neurons (Jiang and Oblinger, 1992). Heterozygous point mutations in βIII have been identified in patients with severe congenital fibrosis of the extraocular muscle type 3 (CFEOM3), an ocular motility disorder (Tischfield et al., 2010). Studies in mice and budding yeast suggest that the phenotypes associated with heterozygous βIII mutations are likely due to reduced binding to kinesins (Niwa et al., 2013; Tischfield et al., 2010). Currently it is difficult to establish whether these mutations directly reduce binding to MAPs. It is also unclear whether these mutations in tubulin alter polymerization dynamics. This is in large part due to the challenges in generating human tubulin from recombinant sources.

To examine the contribution of surface residues in βIII to the structural and biochemical properties of microtubules, we devised a strategy to generate recombinant tubulin heterodimers that have human βIII. We determined the high-resolution structure, characterized the binding to MAPs, and analyzed the polymerization dynamics of wild-type and mutant tubulins. Surprisingly, we find that two disease-related point mutations in βIII, D417H and R262H, alter polymerization dynamics at microtubule plus- and minus-ends. By examining the properties of microtubules assembled from mixtures of wild-type and mutant tubulins, we dissect how the presence of sub-stoichiometric levels of mutant β-tubulin can have distinct effects on MAP binding and dynamic instability.

3.3 Results

Purification of Recombinant Tubulin Heterodimers that Have Wild-Type and Mutant βIII

To generate recombinant human tubulin, we first used a recently reported insect cell-based strategy (Minoura et al., 2013). However, in our hands this immunoprecipitation approach, which generates heterodimers with FLAG-tagged β-tubulin and hexahistidine-tagged α-tubulin, produced an insufficient yield of pure tubulin. Therefore, to generate recombinant tubulin in sufficient yield and to remove any affinity tags, we significantly redesigned the method, incorporating a cleavable hexahistidine tag at the C terminus of β-tubulin, and left α-tubulin untagged. To purify tubulin, we designed a three-step purification strategy that employs nickel-affinity chromatography, cleavage of the hexahistidine tag on β-tubulin, and TOG-domain affinity chromatography (Widlund et al., 2012) (**Fig. 3.1 A**). This protocol typically yielded >95% pure tubulin in amounts sufficient for biochemical and biophysical studies (1.5 mg tubulin per liter of cultured insect cells) (**Fig. 3.1 B**). We generated recombinant forms of tubulin heterodimers containing wild-type βIII and two CFEOM3-linked βIII mutants, D417H and R262H (**Fig. 3.1B**). Protein immunoblots showed that purified recombinant human tubulin has no detectable hexahistidine tag (**Fig. 3.1 C**).

We next used mass spectrometry to confirm the presence of mutated residues (**Fig. 3.2 A-C**) and found that purified α/β-tubulin consisted of >99% recombinant βIII and a close to equimolar mixture of recombinant human (isotype α1B) and endogenous insect α-tubulin (**Fig. 3.3 A**). As human and insect α-tubulin are ~97% identical by sequence

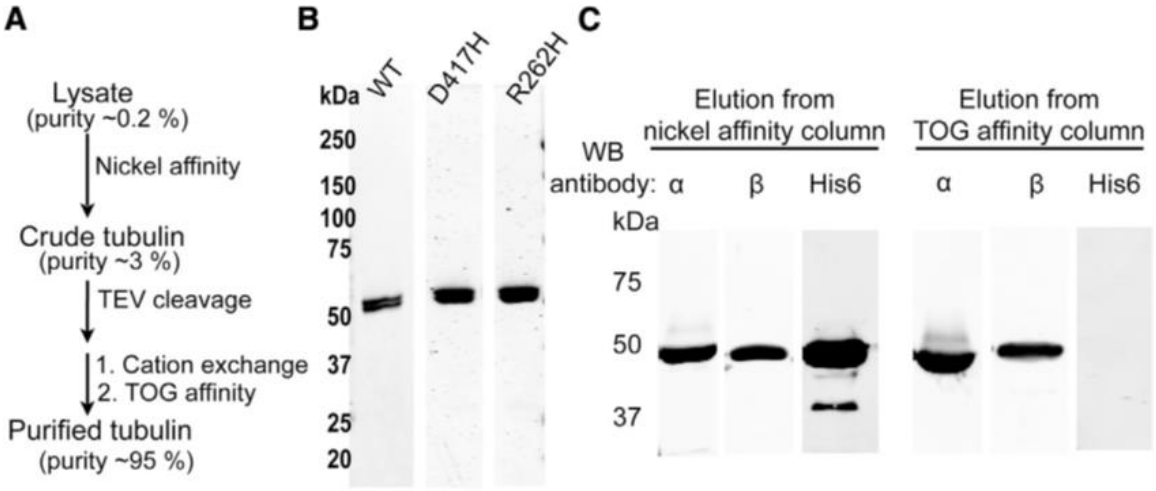

Figure 3.1. Purification and Western Blot Analysis of Recombinant Human βIII.

(A) Schematic detailing the purification of recombinant human tubulin. Typical tubulin purity at key steps is indicated. TEV, tobacco etch virus. (B) SDS-PAGE analysis of purified tubulin. WT, wild-type. (C) Immunoblot analyses of proteins eluted from nickel-affinity and TOG-affinity columns. Antibodies against α-tubulin, β-tubulin, and C-terminal hexahistidine tag were used for Western blots (WB), as indicated.

Figure 3.2. Mass spectrometry analyses of purified recombinant βIII-wild-type, βIII-D417H and βIII-R262H.

(A-C), Peptide fragments from the mass-spectrometry characterization of purified recombinant βIII-wild-type (A), βIII-D417H (B) and βIII-R262H (C). Fragments identified in trypsin digests (blue) and in chymotrypsin digests (underlined) are highlighted. Mutated residues are shown in red.

A

Wild-type

```
  1 M R E I V H I Q A G Q C G N Q I G A K F W E V I S D E H G I D P S G N Y V G
 39 D S D L Q L E R I S V Y Y N E A S S H K Y V P R A I L V D L E P G T M D S V
 77 R S G A F G H L F R P D N F I F G Q S G A G N N W A K G H Y T E G A E L V D
115 S V L D V V R K E C E N C D C L Q G F Q L T H S L G G G T G S G M G T L L I
153 S K V R E E Y P D R I M N T F S V V P S P K V S D T V V E P Y N A T L S I H
191 Q L V E N T D E T Y C I D N E A L Y D I C F R T L K L A T P T Y G D L N H L
229 V S A T M S G V T T S L R F P G Q L N A D L R K L A V N M V P F P R L H F F
267 M P G F A P L T A R G S Q Q Y R A L T V P E L T Q Q M F D A K N M M A A C D
305 P R H G R Y L T V A T V F R G R M S M K E V D E Q M L A I Q S K N S S Y F V
343 E W I P N N V K V A V C D I P P R G L K M S S T F I G N S T A I Q E L F K R
381 I S E Q F T A M F R R K A F L H W Y T G E G M D E M E F T E A E S N M N D L
419 V S E Y Q Q Y Q D A T A E E E G E M Y E D D E E E S E A Q G P K E N L Y F Q
```

B

BIII-D417H

```
  1 M R E I V H I Q A G Q C G N Q I G A K F W E V I S D E H G I D P S G N Y V G
 39 D S D L Q L E R I S V Y Y N E A S S H K Y V P R A I L V D L E P G T M D S V
 77 R S G A F G H L F R P D N F I F G Q S G A G N N W A K G H Y T E G A E L V D
115 S V L D V V R K E C E N C D C L Q G F Q L T H S L G G G T G S G M G T L L I
153 S K V R E E Y P D R I M N T F S V V P S P K V S D T V V E P Y N A T L S I H
191 Q L V E N T D E T Y C I D N E A L Y D I C F R T L K L A T P T Y G D L N H L
229 V S A T M S G V T T S L R F P G Q L N A D L R K L A V N M V P F P R L H F F
267 M P G F A P L T A R G S Q Q Y R A L T V P E L T Q Q M F D A K N M M A A C D
305 P R H G R Y L T V A T V F R G R M S M K E V D E Q M L A I Q S K N S S Y F V
343 E W I P N N V K V A V C D I P P R G L K M S S T F I G N S T A I Q E L F K R
381 I S E Q F T A M F R R K A F L H W Y T G E G M D E M E F T E A E S N M N H L
419 V S E Y Q Q Y Q D A T A E E E G E M Y E D D E E E S E A Q G P K E N L Y F Q
```

C

BIII-R262H

```
  1 M R E I V H I Q A G Q C G N Q I G A K F W E V I S D E H G I D P S G N Y V G
 39 D S D L Q L E R I S V Y Y N E A S S H K Y V P R A I L V D L E P G T M D S V
 77 R S G A F G H L F R P D N F I F G Q S G A G N N W A K G H Y T E G A E L V D
115 S V L D V V R K E C E N C D C L Q G F Q L T H S L G G G T G S G M G T L L I
153 S K V R E E Y P D R I M N T F S V V P S P K V S D T V V E P Y N A T L S I H
191 Q L V E N T D E T Y C I D N E A L Y D I C F R T L K L A T P T Y G D L N H L
229 V S A T M S G V T T S L R F P G Q L N A D L R K L A V N M V P F P H L H F F
267 M P G F A P L T A R G S Q Q Y R A L T V P E L T Q Q M F D A K N M M A A C D
305 P R H G R Y L T V A T V F R G R M S M K E V D E Q M L A I Q S K N S S Y F V
343 E W I P N N V K V A V C D I P P R G L K M S S T F I G N S T A I Q E L F K R
381 I S E Q F T A M F R R K A F L H W Y T G E G M D E M E F T E A E S N M N D L
419 V S E Y Q Q Y Q D A T A E E E G E M Y E D D E E E S E A Q G P K E N L Y F Q
```

A

Figure 3.3. Sequence alignment between human and insect α tubulin.

(A) Protein sequence alignment shows 97% identity between human α-tubulin 1B (NP_006073.2) and α-tubulin from moth cells (ABU94679.1). Peptide fragments that were used to estimate the relative amount of human and insect α-tubulin are labeled in red.

(**Fig. 3.3 A**), we expect that the presence of insect α-tubulin is not likely to have a substantial impact on our analyses. We believe that our recombinant tubulin purification strategy is particularly useful for directly comparing wild-type and mutant forms of human β-tubulin. Hereafter, to emphasize the specific β-tubulin present in the purified tubulin, we refer to our wild-type tubulin as βIII-wild-type and the mutant forms as βIII-D417H and βIII-R262H.

We analyzed the recombinant wild-type and mutant βIII using two approaches. First, size-exclusion chromatography indicated that purified recombinant wild-type and mutant βIII exist as stable dimers in solution with Stokes radii (43 A°) similar to that of bovine tubulin (**Fig. 3.4 A and B**) purified using standard methods involving polymerization/depolymerization cycles (Al-Bassam et al., 2006; Gell et al., 2011). Second, fluorescence microscopy-based analysis indicated that βIII-wild-type, βIII-D417H, and βIII-R262H polymerized to form microtubules in the presence of Taxol (**Fig. 3.4 C-E**).

Disease-Related Point Mutations in βIII Reduce Binding to Motor and Non-motor MAPs

To determine effects of the D417H and R262H tubulin mutations on the binding to motor and non-motor MAPs, we first used a total internal reflection fluorescence (TIRF) microscopy-based assay (**Fig. 3.5 A**). We analyzed the association of Taxol-stabilized microtubules with GFP-tagged kinesin superfamily proteins that share a motor domain conserved in both structure and sequence (Vale and Fletterick, 1997) (kinesin-1ΔC and kinesin-5, in the presence of 2 mM MgATP), and two non-motor MAPs that have

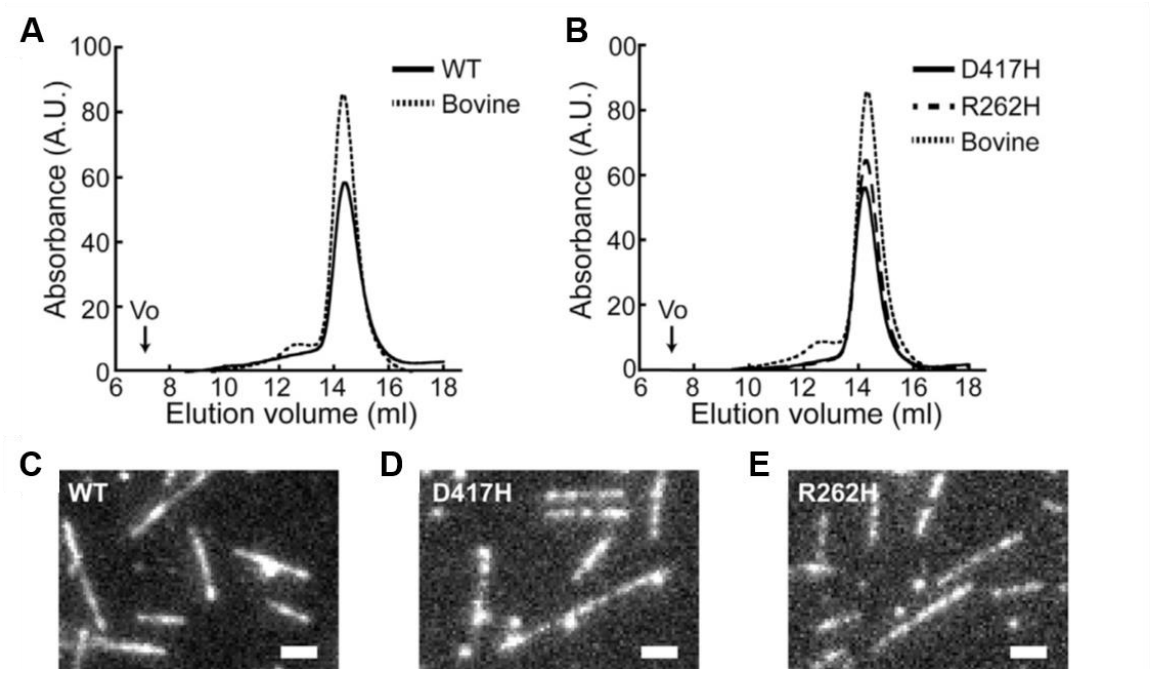

Figure 3.4. Analysis of recombinant human βIII proteins.

(A) Elution profiles of βIII-wild-type (peak volume, 14.4 ml) and bovine tubulin (peak volume, 14.3 ml) from size-exclusion chromatography. V0, void volume. (B) Elution profiles of βIII-D417H (peak volume, 14.3 ml) and βIII-R262H (peak volume, 14.3 ml) from size-exclusion chromatography. Bovine tubulin elution profile is shown as reference. (C-E) TIRF microscopy images of Taxol-stabilized βIII-wild-type (C), βIII-D417H (D), and βIII-R262H (E) microtubules. Fluorescently labeled bovine tubulin (~4%) was added to visualize filaments. Scale bars, 2 μm.

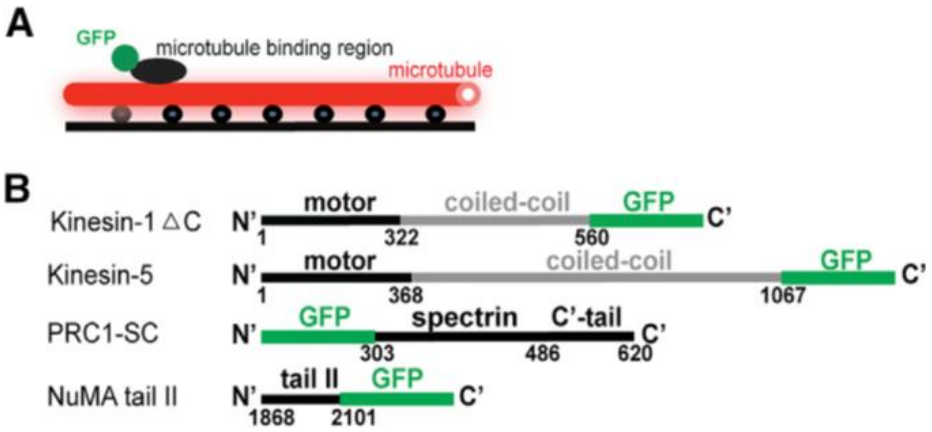

Figure 3.5. Design of TIRF Microscopy Experiments and Fluorescent Protein Constructs.

(A and B) Schematics for assay (A) and MAP constructs used (B) with microtubule-binding regions (black), coiled-coil domain (gray) and GFP (green) highlighted.

structurally distinct microtubule-binding motifs (PRC1-SC and NuMA tail II) (**Fig. 3.5 B**) (Haren and Merdes, 2002; Subramanian et al., 2010; Forth et al., 2014). We found that all of the tested MAPs associate more strongly with wild-type than with mutant βIII microtubules (**Fig. 3.6 A-B** and **Fig. 3.7 A-B**). The GFP fluorescence intensity per micron of microtubule length indicated that under our assay conditions these MAPs have a 5- to 10-fold reduction in direct association with microtubules polymerized either with βIII-D417H or βIII-R262H compared to βIII-wild-type microtubules (**Fig. 3.8 A-D**).

βIII-D417H and βIII-R262H Microtubules Have Altered Intrinsic Polymerization Dynamics Compared to Wild-Type Microtubules

We next employed a TIRF-based single-filament assay to analyze polymerization dynamics of βIII-wild-type (**Fig. 3.9 A**). As a template for microtubule formation, we used guanosine-5'-[(α,β)-methyleno]triphosphate (GMPCPP)-stabilized seeds generated with βIII-wild-type tubulin. In the presence of soluble tubulin and GTP (1 mM), microtubules were observed to grow and shrink at both ends of seeds (**Fig. 3.9 B**). Kymographs of individual microtubules show a noticeable difference in the length and growth rates of microtubule polymer assembled from one end of the seed compared to the other (**Fig. 3.9 C**). Hereafter, as per convention, the faster-growing end is referred to as the plus-end and the slower-growing end as the minus-end. We next measured key parameters of microtubule dynamic instability, including rate of growth (polymerization rate) and the likelihood of transition from relatively slow growth to rapid shortening (catastrophe frequency) (Desai and Mitchison, 1997) at both plus- and minus-ends.

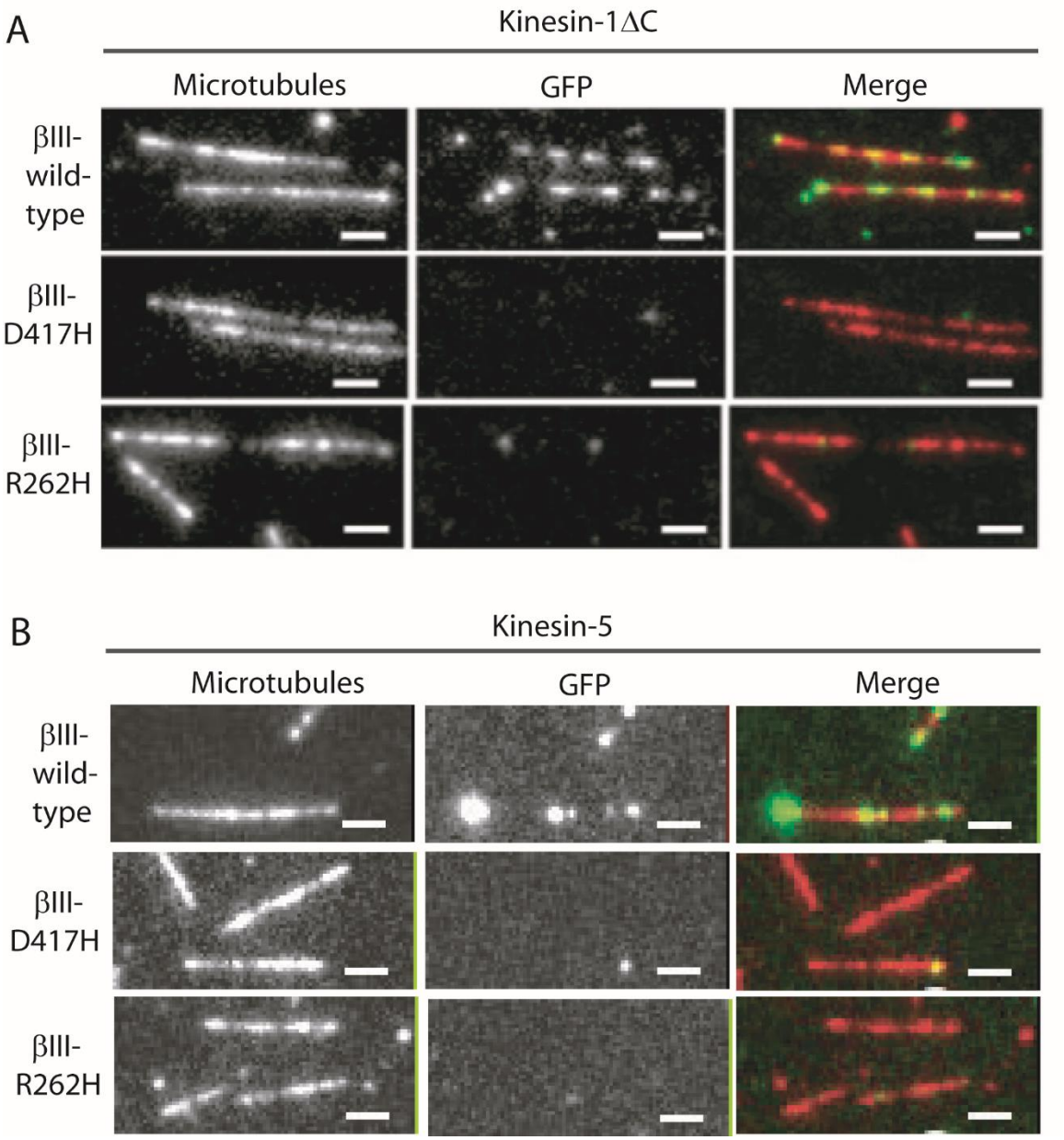

Figure 3.6. Analysis of Motor MAP Binding to Microtubules Assembled with Recombinant βIII Tubulins.

(A and B) Images of microtubule and GFP-tagged MAPs, along with two-color overlays (microtubule, red; GFP, green), are shown for (A) kinesin-1ΔC-GFP (0.7 nM, 2 mM MgATP) and (B) kinesin-5 (0.6 nM, 2 mM MgATP). Scale bars, 2 μm.

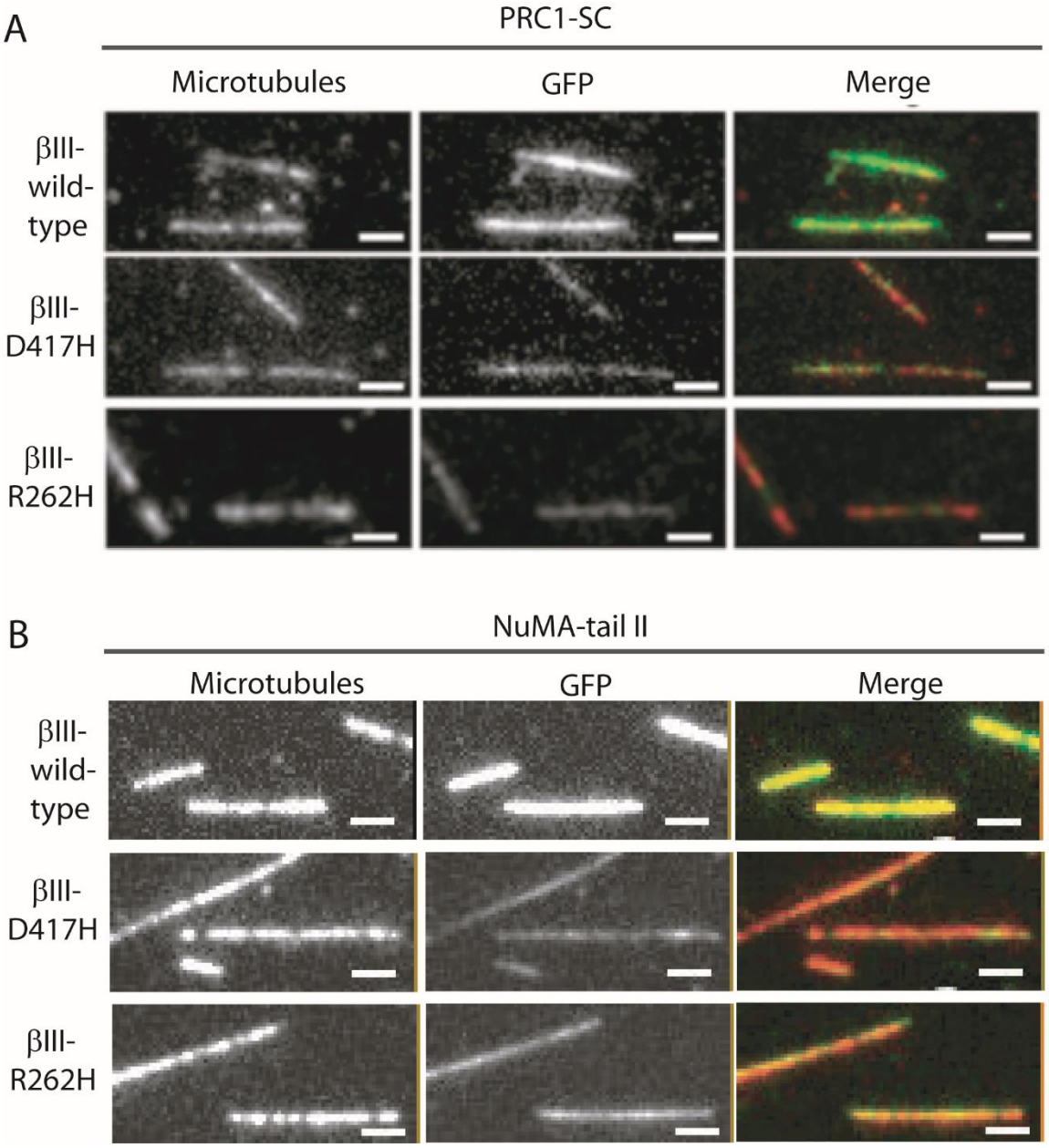

Figure 3.7. Analysis of Non-motor MAP Binding to Microtubules Assembled with Recombinant βIII Tubulins.

(A and B) Images of microtubule and GFP-tagged MAPs, along with two-color overlays (microtubule, red; GFP, green), are shown for (A) GFP-PRC1-SC (16 nM) and (B) GFP-NuMA tail II (20 nM). Scale bars, 2 μm.

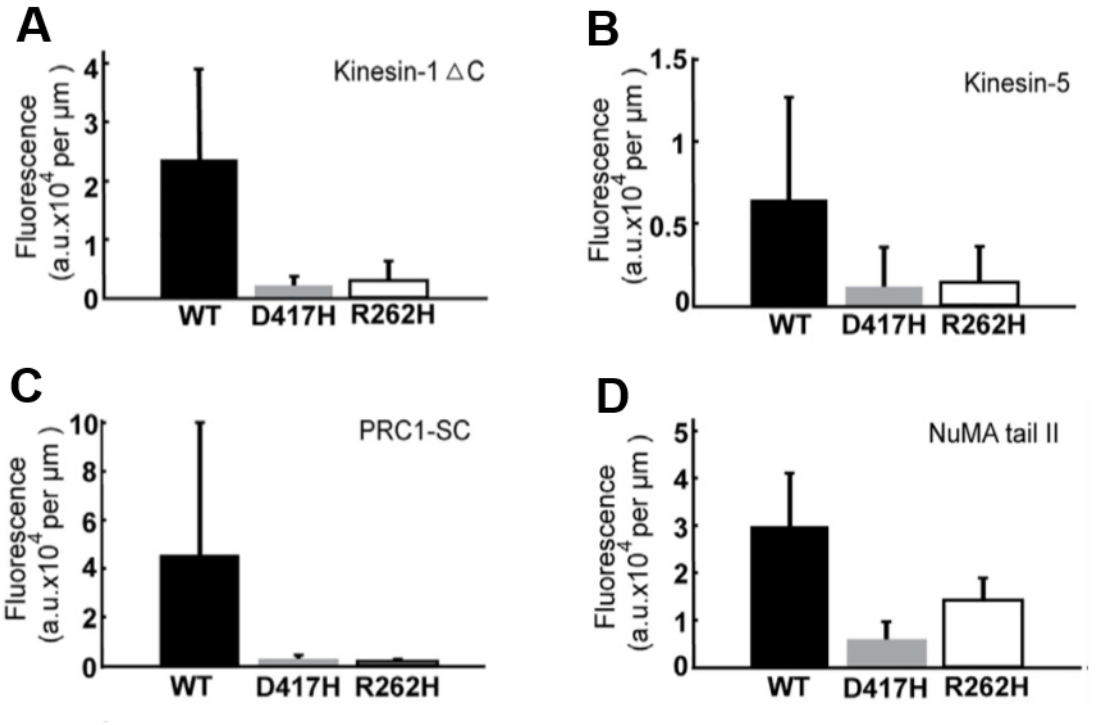

Figure 3.8. Point Mutations D417H and R262H in βIII Reduce the Binding of Motor and Non-motor MAPs to Microtubules.

(A–D) GFP fluorescence intensity per micron along the microtubules for kinesin-1ΔC (A), kinesin-5 (B), PRC1-SC (C), and NuMA tail II (D) is shown. Data from three independent experiments were pooled for each condition and analyzed to determine averages and SD (error bars) (n = 62 or greater).

Figure 3.9. Intrinsic Polymerization Dynamics of βIII-Wild-Type.

(A) Schematic for assay used to analyze polymerization dynamics of single microtubules. Tubulin (red) incorporates at plus- and minus-ends of GMPCPP-stabilized microtubule seeds (green). (B and C) TIRF microscopy image (B) and kymograph (C) of dynamic microtubules growing from GMPCPP seeds in the presence of 10.5 μM βIII-wild-type (WT). (D) Elongation rates of βIII-wild-type at plus- and minus-ends across three different tubulin concentrations. (E) Catastrophe frequency of βIII-wild-type at microtubule plus- and minus-ends. Data from three independent experiments were pooled for each condition and analyzed to determine averages and SD (error bars) (n = 41 or greater). Elongation rates were fitted with the linear equation as a function of the free tubulin concentration. Assuming a Poisson distribution, the standard deviations of catastrophe frequency were calculated as (observed catastrophe frequency)/(number of events counted)$^{0.5}$. Horizontal scale bars, 2 μm; vertical scale bars, 60 s. See also Table 3.1.

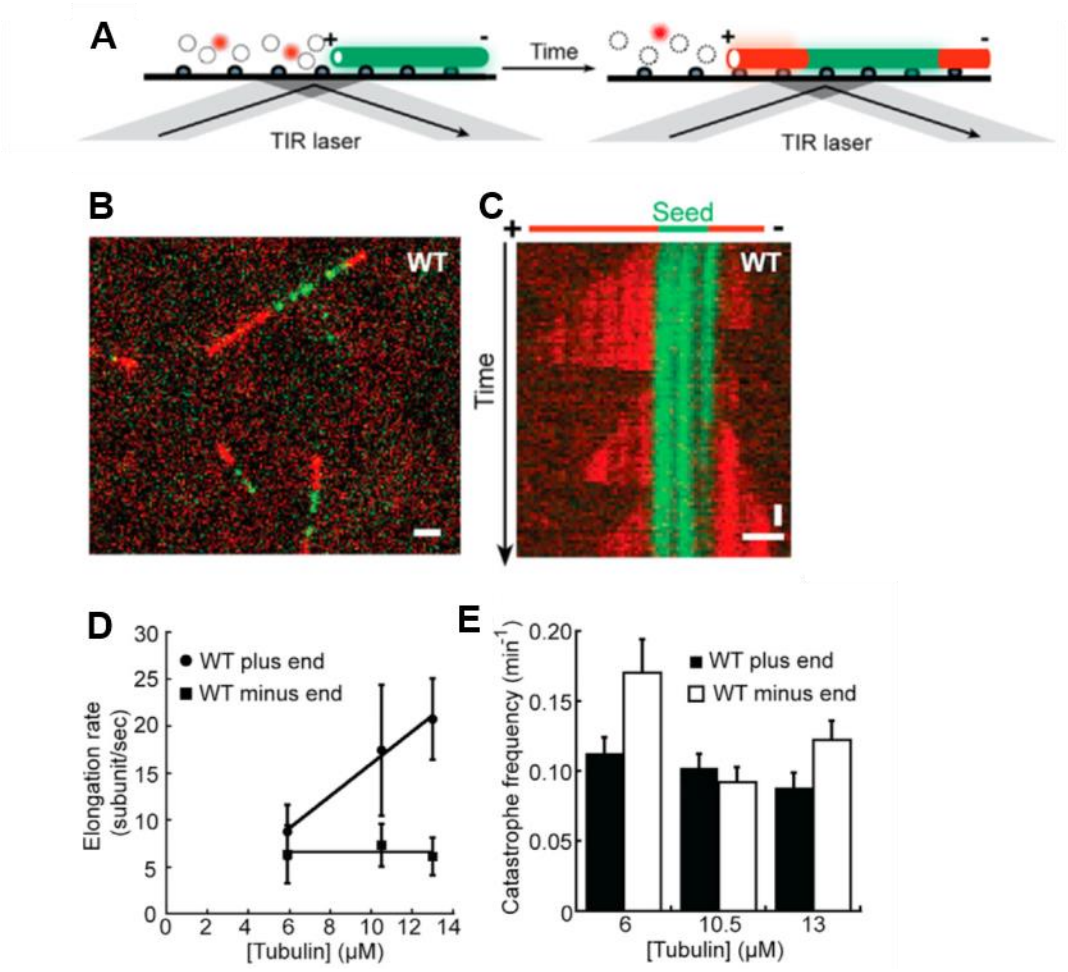
A
+
-
Time
TIR laser
TIR laser
B
WT
C
Seed
+
-
WT
Time
D
WT plus end
WT minus end
Elongation rate (subunit/sec)
30
25
20
15
10
5
0
0 2 4 6 8 10 12 14
[Tubulin] (μM)
E
WT plus end
WT minus end
Catastrophe frequency (min-1)
0.20
0.15
0.10
0.05
0
6
10.5
13
[Tubulin] (μM)

The polymerization rate from plus-ends of βIII-wild-type increased with tubulin concentration and could be fit to a line (Oosawa, 1970), whose slope and intercept suggested the apparent association (k^+) and dissociation (k^-) rate constants of tubulin subunits ($k^+ = 1.7 \pm 0.15\ \mu M^{-1}\ s^{-1}$ and $k^- = 1.1 \pm 1.5\ s^{-1}$) in the 1D model (**Fig. 3.9 D**). By contrast, the minus-end polymerization rate of βIII-wildtype was relatively constant across the range of tubulin concentrations tested (**Fig. 3.9 D**). The catastrophe frequency was 0.1 $\pm$ 0.01 min^{-1} for plus-ends and 0.09 $\pm$ 0.01 min^{-1} for minus-ends at a tubulin concentration (10.5 μM) close to physiological levels (**Fig. 3.9 E**). While variation in catastrophe frequency was observed at different tubulin concentrations, the scatter in these data did not allow for the establishment of a strong correlation between catastrophe frequency and concentration. Together, these data demonstrate βIII-wild-type's dynamic instability and yield key parameters, which thus far have not been available for any purified human tubulin isotype.

We next examined the dynamics of mutant βIII microtubules. At equivalent time intervals, βIII-D417H and βIII-R262H assembled longer microtubule extensions from GMPCPP-stabilized seeds compared to βIII-wild-type across different tubulin concentrations (**Fig. 3.10 A-D**). We first focused on plus-end dynamic instability parameters. For βIII-D417H, polymerization rates at plus-ends of microtubules were ~1.7-fold faster than those for βIII-wild-type (10.5 μM), with a 2-fold higher k^+ and a 7-fold higher k^- (**Fig. 3.10 E**). These microtubules were substantially more stable, undergoing catastrophe ~4-fold less frequently than did microtubules assembled from βIII-wild-type (10.5 μM, **Fig. 3.10 F**). In the case of βIII-R262H, the polymerization rates at plus-ends were similar to those measured for βIII-wild-type (**Fig. 3.10 E**). The catastrophe

Figure 3.10. βIII-D417H and βIII-R262H Have Altered Intrinsic Polymerization Dynamics Compared to βIII-Wild-Type.

(A–D) TIRF microscopy images (A and C) and kymographs (B and D) of dynamic microtubules growing from GMPCPP seeds in the presence of βIII-D417H (A and B) or βIII-R262H (C and D) (10.5 μM). (E–H) Analyses of dynamic instability parameters at plus-ends (E and F) and minus-ends (G and H) of βIII-D417H and βIII-R262H microtubules: elongation rate (E and G) and catastrophe frequency (F and H) are shown. For comparison, the dashed lines indicate the concentration dependence of elongation rates and the catastrophe frequencies of βIII-wild-type (see Fig. 3.9 D and E). Data from three independent experiments were pooled for each condition and analyzed to determine averages and SD (error bars) (n = 41 or greater). Elongation rates were fitted with the linear equation as a function of the free tubulin concentration. Assuming a Poisson distribution, the standard deviations of catastrophe frequency were calculated as (observed catastrophe frequency)/(number of events counted)$^{0.5}$. Horizontal scale bars, 2 μm; vertical scale bars, 60 s. See also Table 3.1.

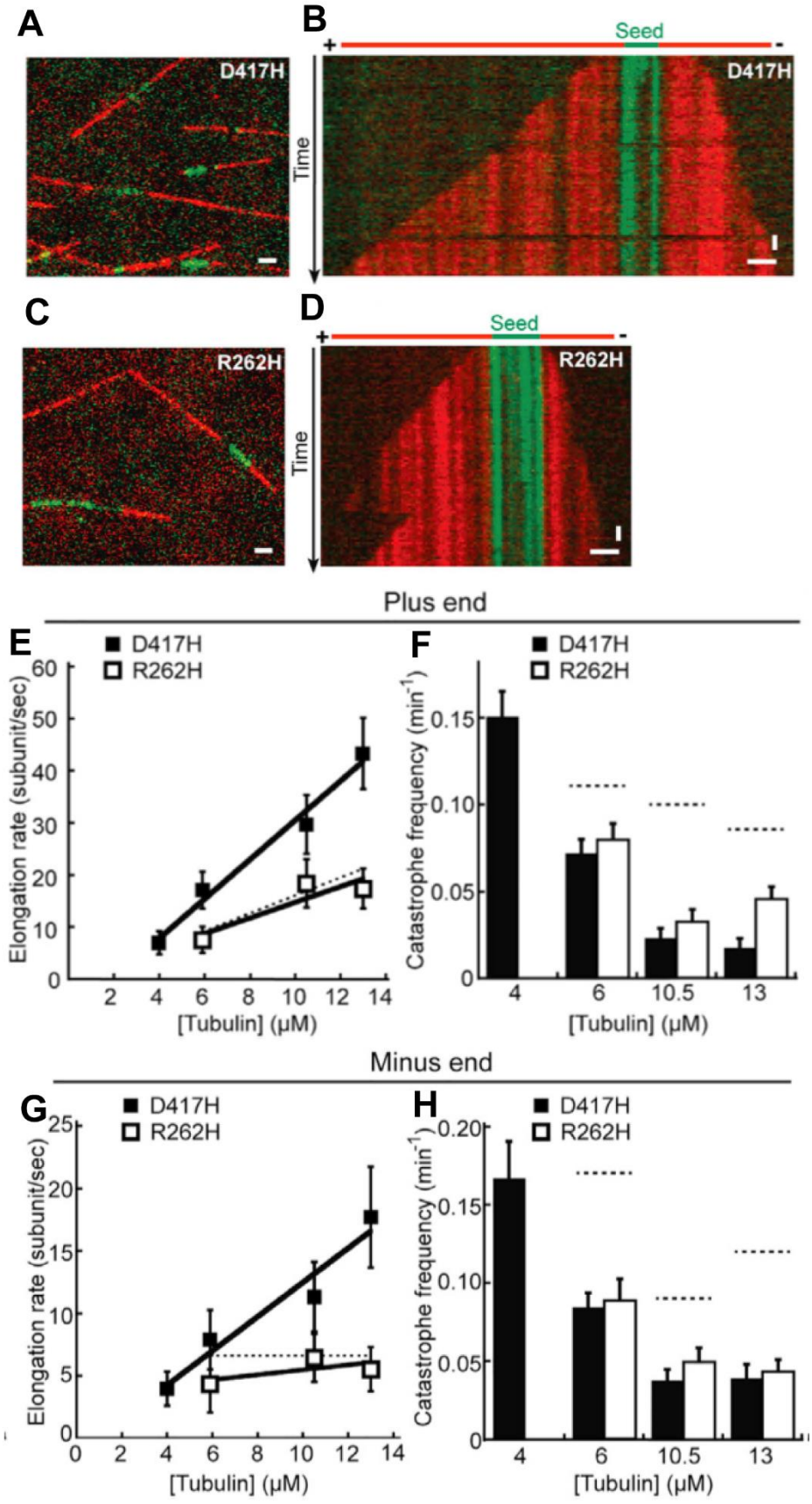
A
B
Seed
+
-
D417H
D417H
Time
C
D
Seed
R262H
R262H
Time
Plus end
E
D417H
R262H
Elongation rate (subunit/sec)
[Tubulin] (μM)
F
D417H
R262H
Catastrophe frequency (min-1)
[Tubulin] (μM)
Minus end
G
D417H
R262H
Elongation rate (subunit/sec)
[Tubulin] (μM)
H
D417H
R262H
Catastrophe frequency (min-1)
[Tubulin] (μM)

requency at microtubule plus-ends was ~3-fold lower than βIII-wild-type (10.5 μM, **Fig. 3.10 F**). Based on the model developed by Leibler and colleagues (Verde et al., 1992) and these measurements, we estimate that βIII-D417H microtubules would be, on average, ~7 times longer than βIII-wild-type, and βIII-R262H microtubules would be ~3 times longer than βIII-wild-type (detailed calculation is provided in **Methods**).

D417H and R262H mutations in βIII not only affect microtubule polymerization dynamics at the plus-ends but also alter filament dynamics at the minus-ends. The growth rates of βIII-D417H microtubule minus-ends were substantially faster than those we measured for βIII-wild-type and varied with tubulin concentration ($k^+ = 1.4 \pm 0.23\ \mu M^{-1}\ s^{-1}$ and $k^- = 1.2 \pm 2.1\ s^{-1}$, **Fig. 3.10 G**). Furthermore, catastrophe frequency was ~2-fold lower for βIII-D417H compared to wild-type tubulin (10.5 μM, **Fig. 3.10 H**). In the case of βIII-R262H microtubule minus-ends, the catastrophe frequency was 2-fold lower compared to βIII-wild-type (10.5 μM, **Fig. 3.10 H**). However, substantial differences in minus-end polymerization rates were not observed between βIII-wild-type and βIII-R262H (**Fig. 3.10 G**). **Table 3.1** summarizes these data. Together, our findings reveal that mutations near the kinesin-binding site can directly alter microtubule dynamics at both filament ends.

Analyses of Mixtures of Wild-Type and Mutant Tubulins

To test whether these βIII mutations have dose-dependent effects on microtubule function, we mixed wild-type and mutant tubulins and examined both binding to MAPs and assembly dynamics. First, we compared MAP binding between mixed mutant and wild-type microtubules. At different ratios of βIII-D417H or βIII-R262H and βIII-wild-type tubulin, microtubules readily polymerized in the presence of Taxol (**Fig. 3.11 A-B**). We added GFP-tagged kinesin-1ΔC to these microtubules and measured the fluorescence

intensity per unit filament length. The average GFP fluorescence intensity on mixed microtubules was lower than that observed for microtubules assembled from βIII-wild-type and decreased further with increasing amounts of βIII-D417H in the polymer (**Fig. 3.11 C**). We also examined the binding of GFP-tagged PRC1-SC to these microtubules and observed fluorescence intensities that were lower than what we observed for wild-type tubulin filaments and higher than what we observed for βIII-D417H filaments (**Fig. 3.11 D**). A similar trend was observed for βIII-R262H and βIII-wild-type mixed microtubules (**Fig. 3.11 A-D**).

Next, we measured dynamic instability parameters in single-filament assays. We observed dynamic microtubule extensions at both plus- and minus-ends of GMPCPP seeds (**Fig. 3.12 A-B**). The catastrophe frequency at filament plus-ends was ~0.11 min^{-1} at equal ratios of βIII-D417H and βIII-wild-type, and ~0.09 min^{-1} at equal ratios of βIII-R262H and βIII-wild-type microtubules (10.5 μM total tubulin concentration). These values are similar to those measured for microtubules assembled with βIII-wild-type (~0.10 min^{-1}, 10.5 μM total tubulin) (**Fig. 3.12 C**). The catastrophe frequency at the minus-ends of mixed microtubules was also similar to that of wild-type alone (**Fig. 3.12 D**). Together, our data suggest that the presence of wild-type tubulin can suppress the altered catastrophe frequencies but only partially recover the reduction in MAP binding due to these point mutations in βIII.

Figure 3.11. Analyses of MAP Binding of Microtubules Polymerized from Mixtures of Wild-Type and Mutant Tubulin

(A and B) Images of microtubules polymerized from equal ratios of βIII-wild-type and βIII-D417H (WT/D417H) or βIII-R262H (WT/R262H), associated GFP-tagged MAPs, along with two-color overlays (microtubule, red; GFP, green), are shown for (A) kinesin-1ΔC (0.7 nM, 2 mM MgATP) and (B) PRC1-SC (16 nM). (C and D) GFP fluorescence intensity of kinesin-1ΔC (C) and PRC1-SC (D) per micron of Taxol-stabilized microtubules polymerized from tubulin with different ratios of βIII-wild-type and mutant βIII tubulin. Data from three independent experiments were pooled for each condition and analyzed to determine averages and SD (error bars) (kinesin-1ΔC, n = 64 or greater; PRC1-SC, n = 66 or greater). Scale bar, 2 μm.

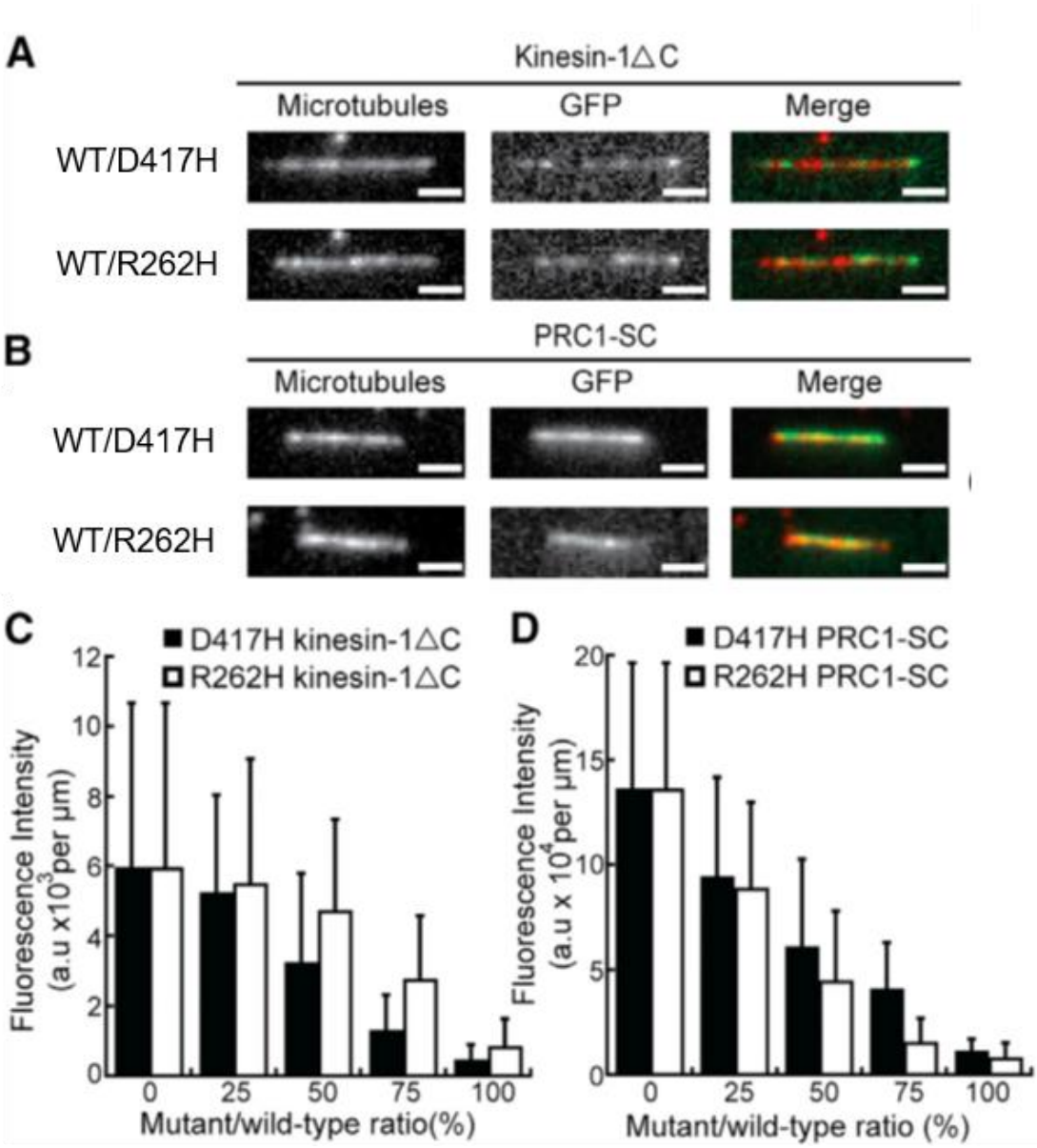
A
Kinesin-1△C
Microtubules
GFP
Merge
WT/D417H
WT/R262H
B
PRC1-SC
Microtubules
GFP
Merge
WT/D417H
WT/R262H
C
D417H kinesin-1△C
R262H kinesin-1△C
Fluorescence Intensity
(a.u x10^3 per μm)
Mutant/wild-type ratio(%)
D
D417H PRC1-SC
R262H PRC1-SC
Fluorescence Intensity
(a.u x 10^4 per μm)
Mutant/wild-type ratio (%)

Figure 3.12. Analyses of Polymerization Dynamics of Microtubules Polymerized from Mixtures of Wild-Type and Mutant Tubulin

(A and B) Kymographs of dynamic microtubule extensions from GMPCPP seeds at equal ratios of βIII-D417H and βIII-wild-type (WT) (A) and at equal ratios of βIII-R262H and wild-type (B). (C and D) Analyses of catastrophe frequency at the growing plus-ends (C) and minus-ends (D) of microtubules. Wild-type and mutant tubulin were mixed in equal ratios while the total tubulin concentration was kept at 10.5 μM. For comparison, dashed lines indicate catastrophe frequency values for microtubules assembled with wild-type (red), βIII-D417H (blue), or βIII-R262H (orange) tubulin (see Fig. 3.9). For C and D, data from three independent experiments were pooled for each condition and analyzed to determine averages and SD (error bars) (n = 43 or greater). Assuming a Poisson distribution, the standard deviations of catastrophe frequency were calculated as (observed catastrophe frequency)/(number of events counted)$^{0.5}$. Horizontal scale bars, 2 μm; vertical scale bars, 60 s.

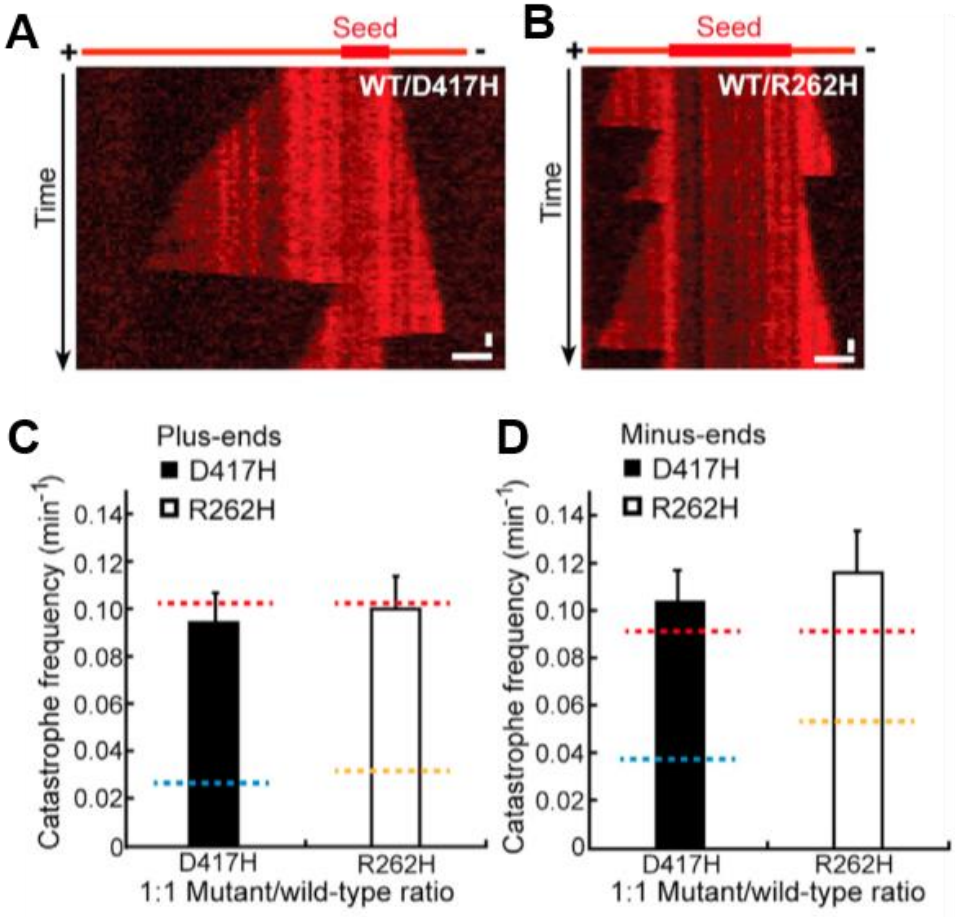
A
Seed
+
-
WT/D417H
Time
B
Seed
+
-
WT/R262H
Time
C
Plus-ends
D417H
R262H
Catastrophe frequency (min-1)
0.14
0.12
0.10
0.08
0.06
0.04
0.02
0
D417H
R262H
1:1 Mutant/wild-type ratio
D
Minus-ends
D417H
R262H
Catastrophe frequency (min-1)
0.14
0.12
0.10
0.08
0.06
0.04
0.02
0
D417H
R262H
1:1 Mutant/wild-type ratio

Table 3.1. Dynamic instability parameters for βIII-wild-type, βIII-D417H and βIII-R262H.

TIRF microscopy-based single filament assays were carried out as described in Methods. Mean±SD are shown for >65 measurements. The values of catastrophe frequency and polymerization rate are from the analyses of experiments with 10.5 μM βIII-wild-type, βIII-D417H or βIII-R262H.

	βIII-Wild-type		βIII-D417H		βIII-R262H	
	Plus-end	Minus-end	Plus-end	Minus-end	Plus-end	Minus-end
k_+ ($\mu M^{-1}s^{-1}$)	1.7±0.15	N/A	3.8±0.4	1.4±0.23	1.5±0.7	N/A
k_- (s^{-1})	1.1±1.5	N/A	7.3±3.4	1.2±2.1	0.4±7.2	N/A
Catastrophe frequency (min^{-1})	0.10± 0.01	0.09± 0.01	0.023± 0.006	0.038± 0.007	0.033± 0.007	0.05± 0.009
Polymerization rate (μm/min)	0.6±0.2	0.3±0.1	1.0±0.2	0.4±0.1	0.6±0.2	0.2±0.1

3.4 Discussion

Our studies indicate that mutations proximal to the βIII kinesin-binding site alter polymerization dynamics. In particular, these mutants suppress catastrophe frequency by magnitudes similar to what is achieved by regulatory proteins or microtubule stabilizing drugs (Mohan et al., 2013; Wieczorek et al., 2015). Structural and mutagenesis studies indicate that residues in helix H7, an element buried in tubulin's core, are important for relaying conformational changes upon GTP hydrolysis during microtubule polymerization (Ravelli et al., 2004; Alushin et al., 2014; Geyer et al., 2015). In contrast, the effects of mutating residues located in tubulin's kinesin-binding site on microtubule dynamics had not been explored. Our studies reveal a largely unexpected mechanism by which residues located on the surface of the microtubule lattice, distal from the nucleotide-binding site and from longitudinal and lateral contacts between subunits, can affect polymerization dynamics.

In contrast to the all-or-nothing effect on polymerization dynamics, the impact on MAP binding when mixing wild-type tubulin with mutant forms is dose dependent, as MAP affinities decrease with increasing amounts of mutant tubulins in the polymer. The concentration of tubulin in cells is estimated to be ~10 μM, of which up to ~80% can be in the polymerized form (Pipeleers et al., 1977). Based on simple binding principles, the fraction of microtubule-bound MAPs that have sub-micromolar binding constants (e.g., kinesin) would be reduced by only a very small amount (~5%) for mutant microtubules relative to wild-type microtubules. A more substantial difference in the fraction bound to wild-type versus mutant microtubules would be observed for MAPs with weak microtubule-binding affinities (details on these calculations are provided in **Methods**).

Therefore, we posit that these mutations in tubulin would cause the associated phenotypes in only those cells where the functions of weakly binding MAPs are critical. Additional cell biological studies are needed to establish whether this hypothesis can help explain disease phenotypes (Niwa et al., 2013; Tischfield et al., 2010).

Our findings reveal that disease-related tubulin mutations alter polymerization dynamics at not only the plus-ends but also the minus-ends of microtubules. The regulation of microtubule plus-ends by MAPs, such as the EB proteins, has been extensively studied (Galjart, 2010; Howard and Hyman, 2007). In contrast, the regulation and function of microtubule minus-end polymerization in cells are poorly understood. It has been generally accepted that γ-tubulin caps and stabilizes microtubule minus-ends in cells (Kollman et al., 2011). However, it is now becoming clear that MAPs, such as katanin and spastin, sever existing filaments to remodel microtubule networks (Roll-Mecak and McNally, 2010). The fate of these new minus-ends is unclear, and we do not know if and when they are capped and stabilized. One clue comes from recent studies of calmodulin-regulated spectrin-associated proteins (CAMSAPs), MAPs that selectively bind microtubule minus-ends, showing that newly generated minus-ends in human cells are not immediately capped but can grow (Jiang et al., 2014). Furthermore, it has been suggested that minus-end-binding proteins have important roles in the development and maintenance of axons and dendrites in neurons (Yau et al., 2014). Together, these data suggest that regulation of microtubule minus-end polymerization plays a key role in regulating microtubule organization. It is likely that access to recombinant human tubulin and different mutant forms should help dissect how these microtubule minus-end-binding proteins interact with the end-stabilizing cap to control microtubule minus-end polymerization in different cellular contexts.

Chapter 4: The spindle midzone functions as a brake to restrict chromosome movement in anaphase.

4.1 Summary

In anaphase, microtubules from opposite half-spindles form antiparallel bundles in the midzone through interactions with PRC1, a conserved non-motor cross-linking protein. Microtubule sliding decreases the length of overlap however it is unclear whether this change facilitates or restricts spindle elongation and thus chromosome movement. Here, we use live cell imaging to examine individual antiparallel bundles during anaphase. We find that the length of overlap decreases while the cross-sectional spacing of bundles stays the same. Loss of midzone organization by knockdown of PRC1 allows chromosomes to hyper-segregate due to increased rates of anaphase spindle elongation. Antiparallel bundle formation can be restored by expressing a mutant PRC1 with reduced affinity for microtubules. However, the length of overlap does not decrease during anaphase and chromosomes still hyper-segregate. Together, these data suggest that the spindle midzone in vertebrates primarily acts as a brake to restrict spindle elongation and to properly position chromosomes during cell division.

4.2 Introduction

Specialized microtubule arrays perform critical functions in diverse cellular contexts. During cell division the spindle midzone, an array of overlapping antiparallel microtubules, assembles between segregating sister chromosomes (Khmelinskii and Schiebel, 2008). Several motor and non-motor proteins, including kinases and phosphatases, that contribute to the assembly and function of the spindle midzone have been identified (Glotzer, 2009). The spindle midzone contributes to positioning the cell division plane and anaphase chromosome movement (Green et al., 2012). Currently, it is not clear if the spindle midzone in human cells generates pushing or braking forces regulating anaphase chromosome movement.

Spindle midzone microtubules have plus-ends that interdigitate near the cell equator and minus-ends proximal to separating spindle poles (Heidemann and McIntosh, 1980; Euteneuer and McIntosh, 1980). A subset of these filaments associate through cross-linking proteins to form bundles that have reduced dynamics (Hu et al., 2011). Filaments in bundles can undergo relative sliding, as evidenced by both photoactivation studies (Saxton and McIntosh, 1987) and serial section electron microscopy showing that the length of microtubule overlap in bundles decreases during anaphase (Mastronarde, 1993).

The change in overlap length can be a consequence of at least two activities. First, motor protein cross-linkers could slide apart midzone microtubules to drive spindle elongation and consequently chromosome segregation (Mcintosh et al., 1969). Several proteins have since been identified, including Eg5 and MKLP1, that can slide antiparallel filaments apart *in vitro* (Nislow et al., 1992; Kapitein et al., 2005) and localize to the midzone (Nislow, 1990; Sharp et al., 1999), suggesting that they may function to slide apart

microtubules in the spindle midzone. In support of this hypothesis, laser ablation of the spindle midzone in human cells decreases the rate of chromosome separation and prevents sister chromatid segregation when the connection to one spindle pole is severed (Kajtez et al., 2016; Vukušić et al., 2017). Second, cortically-anchored motors could pull on microtubules to separate spindle poles and consequently reduce the amount of overlap in spindle midzones. In this scenario, protein cross-linkers within overlapping microtubules in the spindle midzone would act to resist filament sliding. Consistent with this hypothesis, laser ablation of the spindle in *C. elegans* resulted in faster rates of pole separation (Grill et al., 2001). Additionally, ensembles of Eg5 *in vitro* were found to resist relative filament sliding at high velocity, explaining an earlier result that knockdown of the Eg5 ortholog, Bmk-1, results in increased rates of pole separation (Saunders et al., 2007; Shimamoto et al., 2015). Currently, we do not know how changes in the length of microtubule overlap in the spindle midzone of human cells contributes to its function.

Disruption of the spindle midzone (e.g. by laser cutting) reveals evidence for both pushing and braking in different systems. Early laser cutting experiments in fungi and diatoms support a model in which the spindle midzone limits the separation rate of chromosomes during anaphase (Aist and Berns, 1981; Leslie and Pickett-Heapes, 1983). Similar results were observed in the first mitotic division of *C. elegans* embryos (Grill et al., 2001) where molecular dissection has revealed a possible role for motor cross-linking proteins in restricting chromosome movement (Collins et al., 2014; Saunders et al., 2007). In contrast, human cells exhibit decreased rates of chromosome segregation following multiple laser ablations of midzone microtubules in early anaphase (Vukušić et al., 2017). In these cells, a specialized array of overlapping microtubules termed “bridging fibers”

have been identified that link kinetochore fibers on sister chromatids during metaphase (Kajtez et al., 2016). Severing these fibers and the connection to one spindle pole during early anaphase prevents the segregation of sister chromatids on the periphery of the spindle (Kajtez et al. 2016; Vukušić et al. 2017). However, as fungi, worms, and humans recruit a similar set of midzone-associated proteins, it is unclear if differences between species represent lineage-specific specializations of the midzone machinery and if so, the molecular basis of these changes are still unclear.

Specific disruption of the spindle midzone can be achieved through knockdown of PRC1, a member of the conserved Ase1/PRC1/MAP65 family of microtubule cross-linking proteins, without preventing bipolar spindle assembly (Roostalu et al., 2010). Loss of PRC1 or its orthologs impairs antiparallel microtubule bundle formation in the midzone in all organisms examined, in many cases leading to the appearance of two disconnected half spindles in anaphase (Maton et al., 2015; Mollinari et al., 2002; Verbrugghe and White, 2004; Vernì et al., 2004). Interestingly, the impact of loss of PRC1 on chromosome segregation is not equivalent in all systems. In budding and fission yeast, Ase1 deletion impairs spindle elongation, leading to incomplete chromosome segregation and spindle collapse (Pellman, 1995; Schuyler et al., 2003; Yamashita et al., 2005). In contrast, loss of function of the *C. elegans* ortholog of PRC1, SPD-1, increases rates of spindle elongation (Verbrugghe and White, 2004). In human cells, the impact of PRC1 knockdown on chromosome segregation rates has not been studied.

Differences in cell division function may be manifested through differences in the biochemical or biophysical properties of PRC1 family members. Budding yeast Ase1 turnover in the midzone is slow ($t_{1/2} > 7$ min) and *in vitro* can concentrate in microtubule

overlaps to generate entropic forces that resist filament sliding (Schuyler et al., 2003; Lansky et al., 2015). Unlike Ase1, vertebrate PRC1 is not known to concentrate in overlap regions. Experiments defining the cellular turnover rate of PRC1 on midzone microtubule bundles will likely provide insight into PRC1 function in cells. The localization of PRC1 on midzone microtubules narrows during anaphase, likely reflecting the change in microtubule overlap length. However, the dynamics of individual bundles has not been examined in live cells. Furthermore, the basic properties of PRC1, such as microtubule binding affinity, and its impact on microtubule overlap length in human cells has not been examined.

Here, we combine live cell imaging with protein knockdown to examine how microtubule overlap length in the spindle midzone contributes to chromosome movement. We track the 3D organization of dynamic and non-dynamic microtubules tagged by EB1 or PRC1, respectively. Microtubule bundles maintain a constant nearest-neighbor spacing during spindle elongation. Microtubule overlap length decreases during the first half of anaphase and reaches a steady-state length that persists for several minutes. Knockdown of PRC1 increases chromosome segregation rates due to a ~50% increase in the rate of anaphase B spindle elongation. Expression of a mutant PRC1 with reduced microtubule binding affinity forms bundles but cannot rescue the chromosome hyper-elongation defects observed in knockdown cells alone. Together, our data suggest that the midzone in human cells acts as a brake to restrict chromosome separation during anaphase.

4.3 Results

Examining PRC1 and EB1 localization in cross-sectional planes of dividing cells

The spindle midzone consists of both dynamic and non-dynamic microtubules. The plus-ends of dynamic microtubules accumulate plus-end tracking proteins (+TIPs) whereas non-dynamic microtubules, including those in midzone bundles, do not (Akhmanova and Steinmetz, 2015). To examine both populations of microtubules in dividing cells, we generated stable hTERT-RPE1 cells expressing both GFP-tagged EB1 (hereafter, "GFP-EB1"), a +TIP, and Halo-tagged PRC1 (hereafter, "Halo-PRC1"). Immunofluorescence analysis revealed that the pattern of PRC1 localization in cells expressing Halo-PRC1 was similar to endogenous protein in control cells (**Fig. 4.1 A** and **B**). We imaged dividing cells using two-color lattice light sheet microscopy (LLSM) after treating with a Halo-reactant dye. Cells were imaged after pole separation began, which is coordinated with anaphase onset (sister chromatid separation) in these cells (Su et al., 2016). We collected 58 consecutive image planes per cell volume (0.35 nm spacing) in two channels at up to 60 cell volumes/min (see **Methods**). To generate 3D reconstructions, the datasets were processed using a multistep approach that included deskew, deconvolution, and intensity-based alignment (see **Methods**) (Chen et al., 2014).

We generated a maximum intensity projection on a plane incident with the spindle pole-to-pole axis (**Fig. 4.2 A** and **B**). We examined cells at different stages of anaphase, indicated by different pole-to-pole distances. Halo-PRC1 signal intensity was highest near the center of the spindle (**Fig. 4.2 A** and **B**). The width of signal intensity narrowed with increasing pole-to-pole distance, consistent with a reduction in microtubule overlap length seen in electron micrographs (Mastronarde, 1993). These data are consistent with our

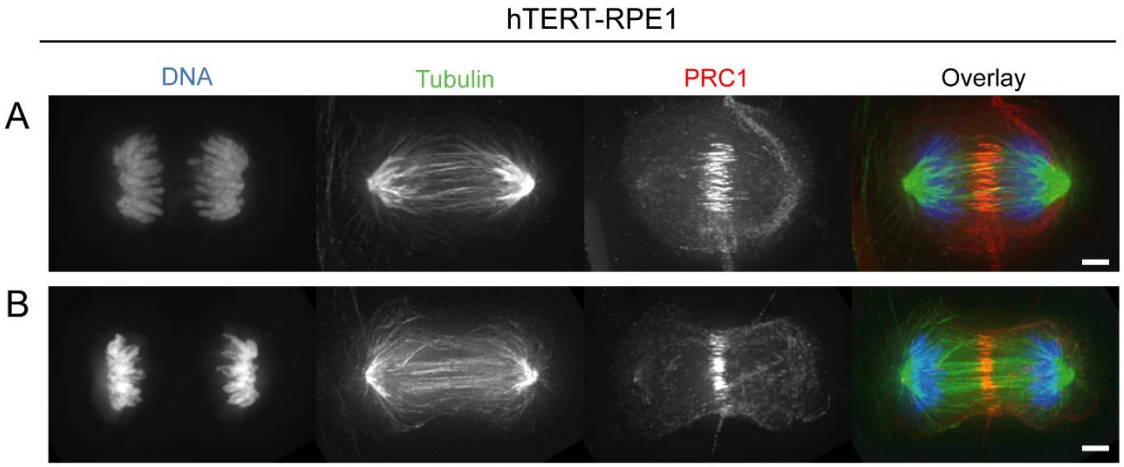

Figure 4.1. Immunofluorescence analysis of PRC1 localization in hTERT-RPE1 anaphase cells.

(A-B) Single channel images and overlays show chromosomes (blue), tubulin (green), and PRC1 (red) in a mid-anaphase (A) and late anaphase (B) cell. Scale bar, 3 μm.

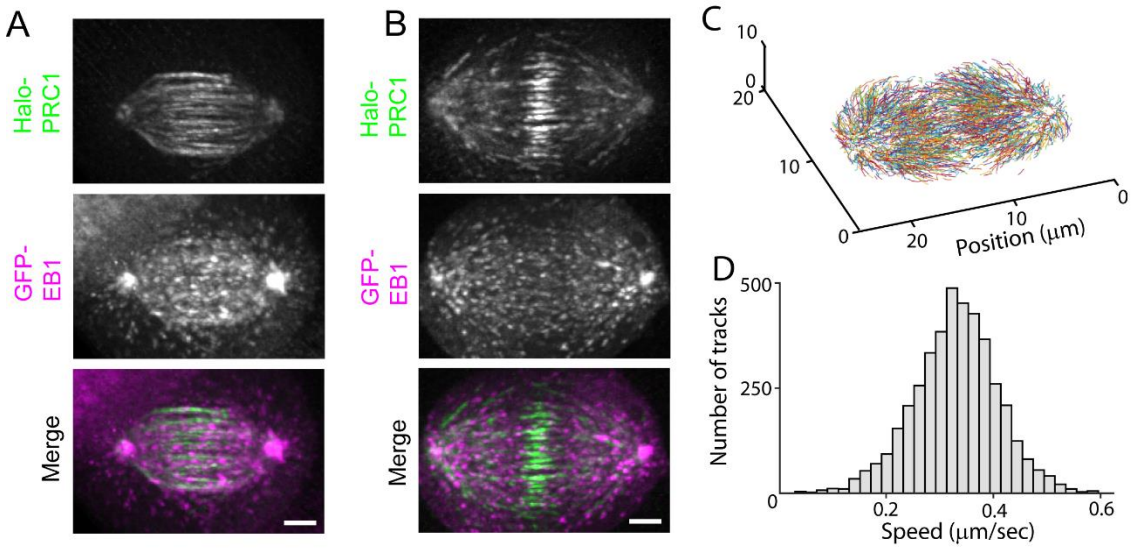

Figure 4.2. 3D tracking of GFP-EB1 spots in dividing cells.

(A-B**)** Near-simultaneous two-color lattice light sheet microscopy was used to image Halo-PRC1 and GFP-EB1 in hTERT-RPE1 cells. Images were captured at 1 sec intervals. A single frame (maximum intensity projections) from two different cells in early (A) or late (B) anaphase are shown. Single channel images and overlays show Halo-PRC1 (green) and GFP-EB1 (magenta). Scale bar, 3 μm. (C) GFP-EB1 trajectories generated by automated 3D comet tracking. (D) Histogram of GFP-EB1 track velocities during anaphase. Data were pooled from from n = 3 cells. Mean velocity: 0.33 +/- 0.08 μm/sec (+/- SD).

immunofluorescence staining of hTERT-RPE1 control cells (**Fig. 4.1 A**) and previous studies of fixed cells (Jiang et al., 1998; Mollinari et al., 2002; Zhu et al., 2006; Subramanian et al., 2013). GFP-EB1 intensity was highest near the poles and appeared as at the ends of interpolar and astral microtubules, as expected (Akhmanova and Steinmetz, 2008). We performed three-dimensional tracking of EB1 comets over time (**Fig. 4.2 C**) and found that the distribution of track velocities (**Fig. 4.2 D**) (mean: 0.33 +/- 0.08 μm/sec, +/- SD) was similar to that reported in a previous study (Yamashita et al., 2015).

We examined cross-sectional slices of the midzone and selected the plane equidistant from both spindle poles (**Fig. 4.3 A**) (hereafter, the "midplane") for further examination (**Fig. 4.3 B**). Halo-PRC1 and GFP-EB1 both appear as spots of signal intensity (**Fig. 4.3 C**). Two-color overlays showed that PRC1-tagged microtubules and dynamic, EB1-tagged microtubules coexist in a dense network in the spindle midzone (**Fig. 4.3 C**).

Previous studies have indicated that the total tubulin in polymer is constant from metaphase through anaphase as the spindle elongates (Zhai and Borisy, 1994). This change in end-to-end could result in compression and reduce the spacing between microtubules near the center. We examined PRC1 spots in cross-sections and found that these spots frequently appeared to change shape between sequential frames (**Fig 4.3 D**). Occasionally, we observed spots appear to approach one another in consecutive image frames (**Fig. 4.3 E**). These spots subsequently appeared to fuse, forming a single spot with higher signal density (**Fig 4.3 E**). Such events could typically be detected once every few frames (~10 s). We rarely observed events in which spots appeared to split. These data suggest that both dynamic and non-dynamic filaments in the spindle midzone undergo changes on similar timescales (~10s of seconds).

Figure 4.3. Examining PRC1 and EB1 localization in cross-sectional planes of dividing cells.

(**A-B**) Cartoons of anaphase spindles show PRC1 and EB1 decoration in maximum intensity projections (**A**) or in cross-section (**B**). The position of the spindle "midplane", the plane equidistant from the two spindle poles and perpendicular to the spindle long axis, is indicated (dashed line). (**B**) Inset shows schematic of nearest neighbor distances measured between two PRC1 spots (dashed line), two EB1 spots (dotted line) or between one PRC1 and one EB1 spot (solid line). (**C**) Cross-sectional view of the spindle midplane for the cell shown in Fig. 4.2 B at three selected time points. T = 0 s indicates the start of imaging. Scale bar, 3 μm. (**D**) Contrast-enhanced images from the spindle midplane of an hTERT-RPE1 expressing GFP-PRC1 at select time points. Time = 0 s was assigned to the frame immediately prior to pole separation (see Methods). Scale bar, 3 μm. (**E**) Inset from yellow boxes in (**D**), magnified 5.3x. The position of two GFP-PRC1 "spots" in consecutive frames are indicated (yellow circles).

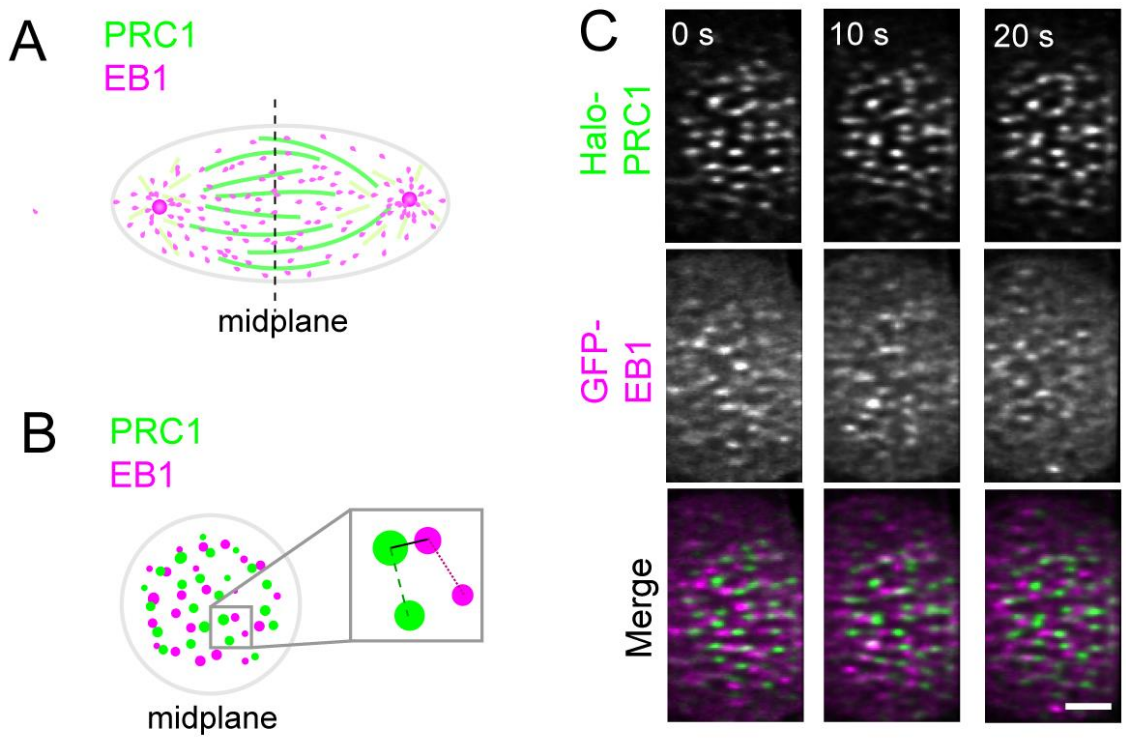
A
PRC1
EB1
midplane
B
PRC1
EB1
midplane
C
0 s
10 s
20 s
Halo-PRC1
GFP-EB1
Merge

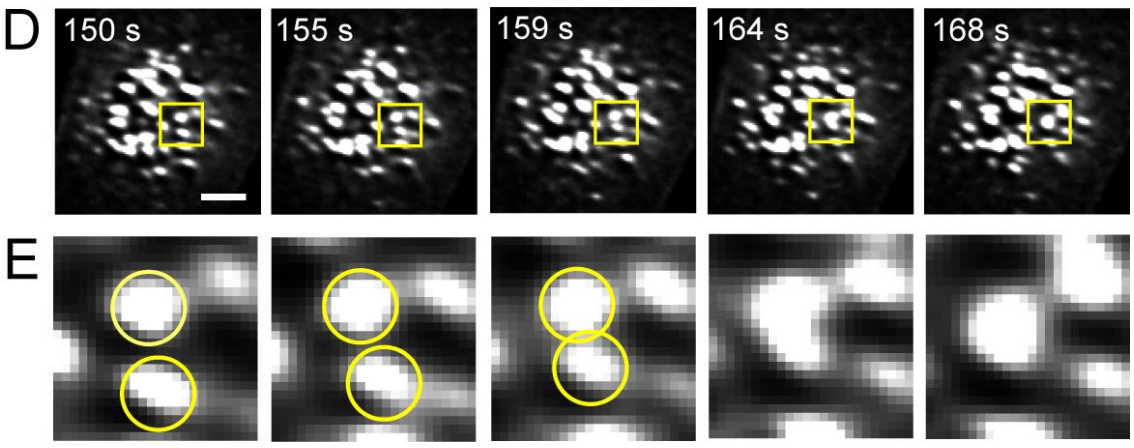
D
150 s
155 s
159 s
164 s
168 s
E

In metaphase, the number of PRC1-tagged microtubule bundles is set by the number of chromosome pairs (Polak et al., 2017) and likely corresponds to the number of bundles at the start of anaphase. In hTERT-RPE1 cells, which have 46 chromosomes, as little as 5 fusion events could decrease the number of bundles by ~ 10%. To investigate this possibility, we examined LLSM movies of GFP-PRC1 alone. GFP- PRC1 localization was similar to endogenous localization of PRC1 in immunofluorescence images of fixed control cells (**Fig. 4.1 A**). We performed watershed analysis on segmented LLSM images of GFP-PRC1 in the midplane and counted the number of spots in each frame (**Fig. 4.4 A**). The total number of spots fluctuated in consecutive image frames but on average did not decrease (**Fig. 4.4 B**). This suggested that fusion between bundles is compensated by the assembly of additional microtubule bundles, consistent with previous reports that midzone microtubule bundles can assemble in the absence of pre-anaphase microtubules (Canman et al., 2000).

The assembly of additional bundles in anaphase could impact the organization of the midzone by decreasing the spacing between microtubule in the midzone. To examine this possibility, we performed 2D localization analysis on GFP-EB1 and Halo-PRC1 spots and measured the nearest-neighbor distance between spots (**Fig. 4.3 B**). The average nearest-neighbor distance between PRC1 spots was ~1 μm and did not change over the course of the movie (100 frames at 1 frame/sec) (**Fig. 4.4 C**). We observed a similar trend for GFP-EB1 spots (**Fig. 4.4 D**). The average nearest-neighbor distance between PRC1 and EB1 spots was smaller, ~0.6-0.7 μm (**Fig. 4.4 E**). We pooled the data from the first 30 frames of each movie and plotted the average measurement for each cell (n = 3 cells) (**Fig. 4.4 F**) and found this difference to be significant ($p < 0.02$). Importantly, the S.D. of this

Figure 4.4. Analysis of PRC1 and EB1 spots in cross-sectional planes of dividing cells

(**A**) Cross-sectional plane of an hTERT-RPE1 expressing GFP-PRC1 signal at select time points after watershed image processing. Scale bar, 3 μm. (**B**) Number of "spots" in watershed-processed images in each frame (1 frame/4.4 s) (average +/- S.D.). (**C**-**E**) Nearest-neighbor distances show average +/- S.D for each frame of the movie for the cell shown in Fig. 4.2 B and Fig. 4.3 C. Measurements between pairs of PRC1 spots (**C**), pairs of EB1 spots (**D**), and PRC1 and EB1 spots (**E**) are shown. (**F**) Average nearest-neighbor distance measurements, pooled from the first 30 frames of each movie (n = 3 cells) (PRC1-PRC1: 1.03 +/- 0.12 μm; EB1-EB1: 1.04 +/- 0.09 μm; PRC1-EB1: 0.71 +/- 0.06 μm; **p < 0.02; ***p < 0.004).

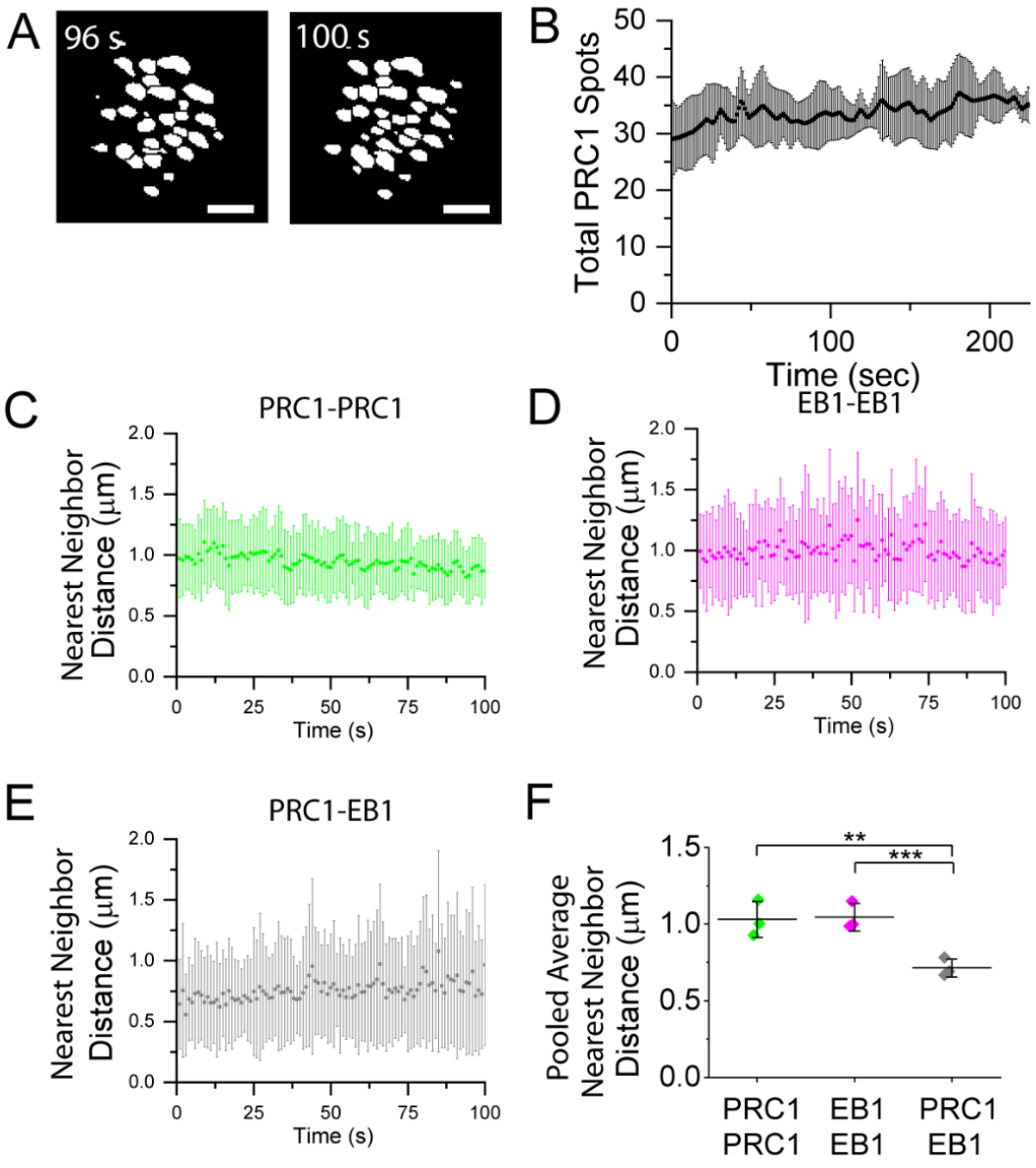
A
96 s
100 s
B
Total PRC1 Spots
Time (sec)
C
PRC1-PRC1
Nearest Neighbor Distance (μm)
Time (s)
D
EB1-EB1
Nearest Neighbor Distance (μm)
Time (s)
E
PRC1-EB1
Nearest Neighbor Distance (μm)
Time (s)
F
Pooled Average Nearest Neighbor Distance (μm)
**
***
PRC1 PRC1
EB1 EB1
PRC1 EB1

measurement was small, indicating that each of these measurements was similar for cells at different stages of anaphase, regardless of the length of microtubule overlap. Our observations suggest that the rules that specify spindle midzone architecture are independent of spindle length.

Analysis of microtubule overlap length in individual PRC1-tagged microtubule bundles in dividing cells

The length of microtubule overlap decreases during anaphase (Mastronarde, 1993). To examine the dynamics of this process and relate it to chromosome segregation distance, we used hTERT-RPE1 cells stably expressing GFP-PRC1 and treated the cells with a far-red DNA dye. As PRC1 has been shown to exhibit selectivity of binding to antiparallel overlaps over parallel overlaps or single filaments, we reasoned that the length of PRC1 decoration on midzone microtubules can be used as a readout of antiparallel overlap length in cells (Bieling et al., 2010; Subramanian et al., 2010). LLSM allowed near-simultaneous two-color imaging of whole cell volumes (101 frames at 0.4 nm spacing) at up to 20 cell volumes/min. We generated 3D reconstructions following a similar process as that done for GFP-EB1/Halo-PRC1 cells (see **Methods**). T = 0 was assigned to the frame immediately before the frame with detectable chromatid separation. Maximum intensity projections showed GFP-PRC1 localization in between the segregating chromosomes that increased in intensity with increasing chromosome segregation distance (**Fig. 4.5 A**). We observed some GFP-PRC1 signal between spindle poles and the cell cortex (**Fig. 4.5 A** panel **ii**), likely corresponding to "end-tags" on astral microtubules (Subramanian et al,

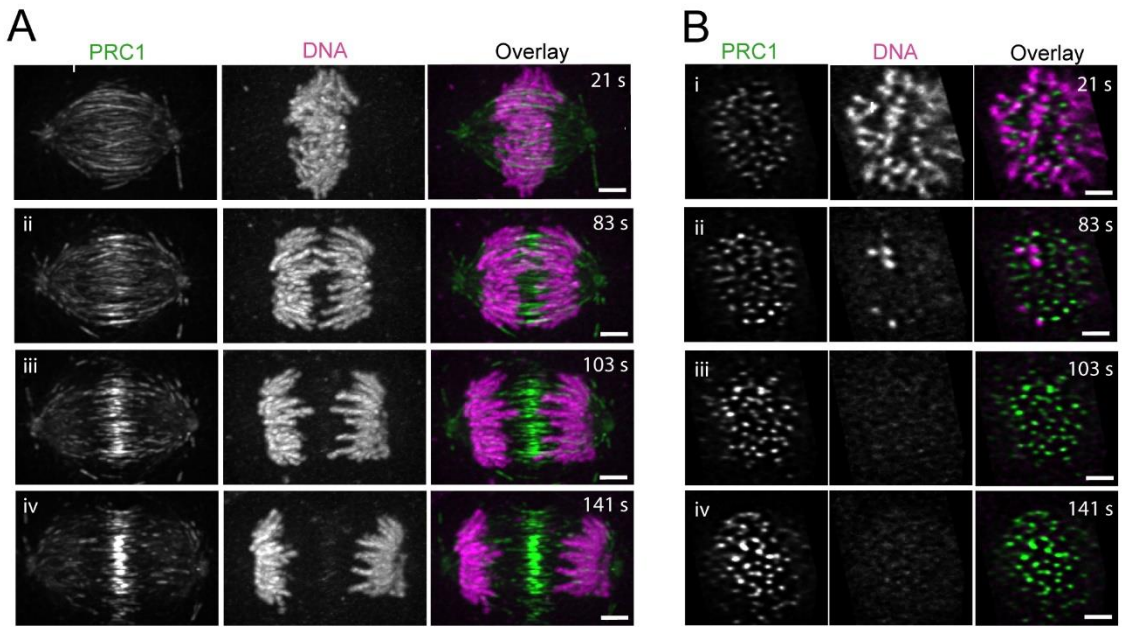

Figure 4.5. Near-simultaneous two-color imaging of GFP-PRC1 and chromosomes in dividing cells.

(**A-B**) Near-simultaneous two-color lattice light sheet imaging was used to track GFP-PRC1 and chromosomes during anaphase in hTERT-RPE1 cells. Images were captured at 3 sec intervals. T = 0 was assigned to the frame immediately prior to that with detectable chromatid separation. Single channel images and overlays from selected time points show GFP-PRC1 (green) and chromosomes (magenta). Scale bar, 3 μm. (**A**) Maximum intensity projections. (**B**) Single image planes corresponding to the spindle midplane for the same time points of the cell shown in (**A**). Scale bar, 3 μm.

2013). In the midplane, GFP-PRC1 was observed throughout anaphase, but chromosome signal was only observed for the first ~90 s, as expected (**Fig. 4.5 B**).

To identify individual bundles, we processed the LLSM image data using a multistep approach that included 3D watershed and segmentation (see **Methods** for details). Fusion events precluded tracking of single microtubule bundles over time. Therefore, we examined the average microtubule overlap length in each frame of each movie (n = 5 cells) (**Fig. 4.6 A**). At anaphase onset, overlap length was ~ 4.5 µm, which spans ~40% of the total spindle length. After ~50 s, the length of microtubule overlap began to decrease over time and reached a final length by ~210 s into anaphase.

We then examined the distribution of bundles lengths by pooling the data from each cell at select time points (**Fig. 4.6 B**). We found that while we could observe a statistically significant decrease in the average bundle length, the distribution of individual bundle lengths was broad. At t = 12 s, the average microtubule bundle length is 4.2 +/- 2.2 µm (n = 168 +/- SD), which decreases to 3.3 +/- 2.8 µm at t = 102 s (n = 213 +/- SD, $p<0.0002$), then to 2.4 +/- 1.4 µm at t = 188 s (n = 248, $p<0.0002$). Most of the bundle length change occurs between T = 50 - 150 s, corresponding to a rate of change of ~ 1 µm/min. As midzone plus-ends have been shown to be non-dynamic (Hu et al., 2011), the change in bundle length likely corresponds to the extent of microtubule sliding.

We then measured chromosome segregation distance in each frame (see **Methods**) (**Fig. 4.6 C**). Chromosome segregation speed was determined by fitting a line to data in different time intervals (from T = 50 - 250 s, 50 s bin size) ($R^2 > 0.98$) (**Fig. 4.6 D**). The fastest rate of chromosome movement (relative to position immediately before anaphase

Figure 4.6. Analysis of microtubule overlap length of individual PRC1-tagged microtubule bundles in dividing cells.

(**A**) Average bundle length over time. Each point represents the average bundle length in one cell at the indicated time in anaphase. Data from select time points are highlighted (green points). T = 0 was assigned to the frame immediately prior to that with detectable chromatid separation. Data from n = 5 cells are shown. (**B**) Dot and box plot showing the microtubule overlap length for individual microtubule bundles in n = 5 cells. Bundle lengths are 4.2 +/- 2.2 μm (t = 12 s, n = 168 +/- SD), 3.3 +/- 2.8 μm (t = 102 s, n = 213 +/- SD), and 2.4 +/- 1.4 μm (t = 188 s, n = 248) (average +/- SD) (**p < 0.002). (**C**) Chromosome position over time, measured as the distance moved relative to position at T = 0. Data from one of the two chromosome masses are shown. (**D**) Chromosome segregation rates at different time intervals following anaphase onset. (**E**) Spinning disk confocal images of GFP-PRC1 in an hTERT-RPE1 cell. Time relative to photobleaching. Scale bar, 3 μm. (**F**) Plot of normalized recovery for bleached GFP-PRC1 signal (red) and unbleached control signal (gray). Data were fit to the following equation: $f(x) = A[1-e^{(-kx)}]$. k = 0.035 (95% confidence bounds: 0.023, 0.047)).

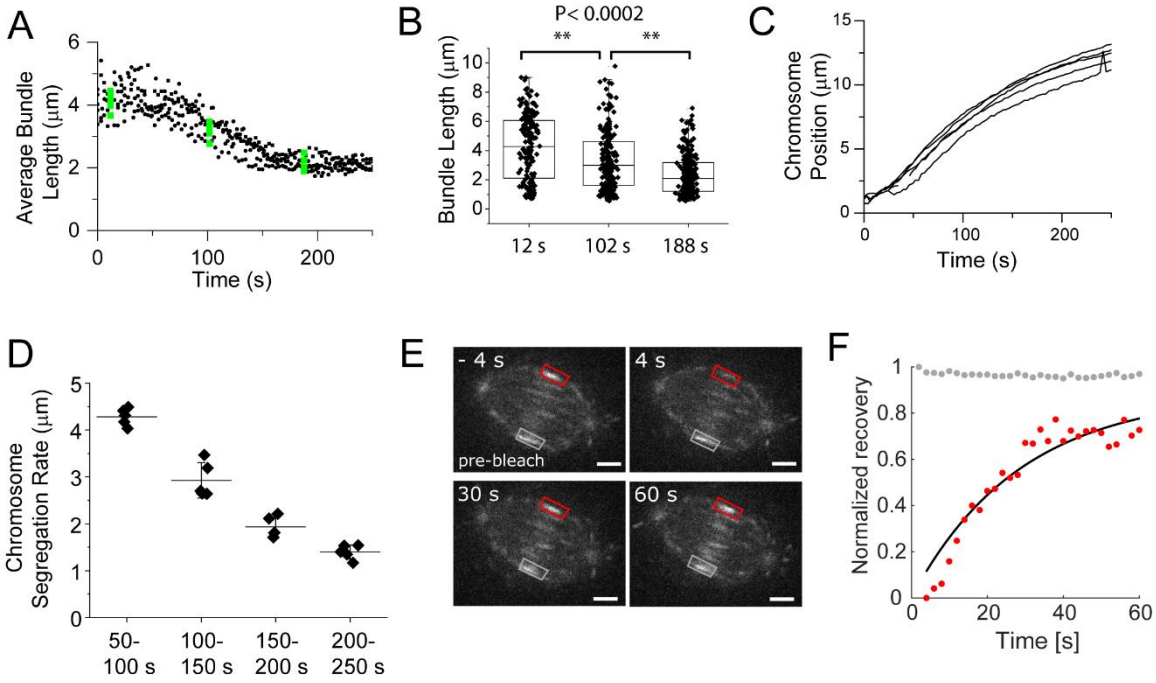
A
Average Bundle Length (μm)
Time (s)
B
P< 0.0002
**
**
Bundle Length (μm)
12 s
102 s
188 s
C
Chromosome Position (μm)
Time (s)
D
Chromosome Segregation Rate (μm)
50-100 s
100-150 s
150-200 s
200-250 s
E
- 4 s
4 s
pre-bleach
30 s
60 s
F
Normalized recovery
Time [s]

onset) occurred between 50 - 100 s (4.3 +/- 0.2 μm/min, n = 5 cells), and decreased with time. These analyses revealed that the rate of chromosome separation was ~ 4x faster than the rate of overlap length shortening (~ 1 μm/min). Furthermore, chromosomes separate by up to 8 μm by T = 150 s, whereas microtubule overlap length decreases by only ~2 μm. After this time, a further reduction in bundle length is not observed, but chromosomes continue to separate up to an inter-chromosome distance of 12.3 +/- 0.8 μm at T = 250 s, when cleavage furrow ingression became apparent in each cell examined (n = 5 cells). These data suggest that relative sliding in midzone microtubule bundles can account for only ~15% of chromosome motion in anaphase, suggesting that chromosome separation is unlikely to be the primary function of the mammalian spindle midzone.

We examined the dynamics of PRC1 cross-linkers within microtubule bundles during early-mid anaphase, when the length of overlap decreases. We used fluorescence recovery after photobleaching (FRAP) analysis to determine the turnover of GFP-PRC1 molecules in bundles (**Fig. 4.6 E**). In the absence of chromosome markers, we estimated time in anaphase based on the length of PRC1-tagged bundles. We selected cells that had microtubule bundles between 2-3.5 μm in length. The t½ of GFP-PRC1 turnover was 36 +/- 9 s (n = 5 cells,+/- SD) (**Fig. 4.6 F**). This relatively high turnover rate of PRC1 suggests that it is unlikely to function as a gas-like brake, as has been hypothesized for Ase1 (Braun et al., 2011; Lansky et al., 2015). Together, these data suggest that the spindle midzone is both robust and flexible, allowing it to maintain a constant organization throughout anaphase while accommodating turnover of its components.

PRC1 knockdown results in increased chromosome segregation rates and leads to chromosome "hyper-segregation"

If relative sliding within microtubule bundles contributed to chromosome motion, we reasoned that disruption of microtubule bundles through knockdown of PRC1 would decrease chromosome segregation distance. We adopted an inducible shRNA-based approach as irreversible knockout leads to cumulative defects that result in senescence (McKinley and Cheeseman, 2017). Western blots of metaphase-arrested cell lysates showed that efficiency of PRC1 knockdown was 95 +/- 1% (n = 3 blots, +/- SD) in HeLa cells ~72 hr after shRNA induction (hereafter, "shPRC1") (**Fig. 4.7 A**). The mitotic index in these cells (4.3% +/- 1.6%, n = 1225 cells, +/- SD) was not significantly different from that in HeLa controls (HeLa lacking the shRNA construct) (5.8% +/- 2.0%, n = 2944 cells, +/- SD, $p > 0.2$) (**Fig. 4.7 B**). Consistent with PRC1's role in completion of cell division, a substantial fraction of cells in this population appeared to have more than one nucleus, indicating at least one cell division failure (**Fig. 4.7 C**).

We next used immunofluorescence and microscopy-based analyses to examine PRC1 knockdown during anaphase. In control cells, endogenous PRC1 localizes to microtubules between segregating chromosomes, similar to that observed in hTERT-RPE1 cells (**Fig. 4.7 D**). PRC1 signal was detected on 100% of anaphase spindles in control cells (n = 77 cells), indicated by a peak in signal intensity at the center of the spindle in linescans drawn across the pole-to-pole axis. In contrast, PRC1 signal was not detected over background in 32 out of 35 shPRC1 anaphase (**Fig 4.7 E**). Anaphase cells were detected at a similar frequency (~10%) in both shPRC1 and control cells.

Figure 4.7. Western blot and immunofluorescence analysis of HeLa cells expressing shRNA to PRC1.

(**A**) Western blot analysis of cell lysates of HeLa control cells (lanes 1 and 4), and HeLa cells containing shRNA to PRC1 before (lanes 2 and 5) and after (lanes 3 and 6) tetracycline induction of shRNA construct. Antibodies against α tubulin and PRC1 are indicated. Expected position of PRC1 protein is indicated (red asterisk). (**B**) Mitotic index for HeLa cells (control: 5.8% +/- 2.0%, n = 2944 cells) and HeLa cells expressing shRNA to PRC1 (shRNA: shRNA: 4.3% +/- 1.6%, n = 1225 cells) ($p > 0.2$). Average +/- SD. (**C**-**E**) Immunofluorescence analysis of fixed cells. (**C**) Overlay image of fixed HeLa cells 72 hr after induction of shRNA expression show tubulin (green) and DNA (blue). Cells with >1 nucleus are indicated (yellow asterisk). Scale bar, 50 μm. (**D**-**E**) Single channel images and overlays show chromosomes (blue), tubulin (green), and PRC1 (red) in control (**D**) and shRNA-expressing (**E**) cell. Scale bar, 3 μm.

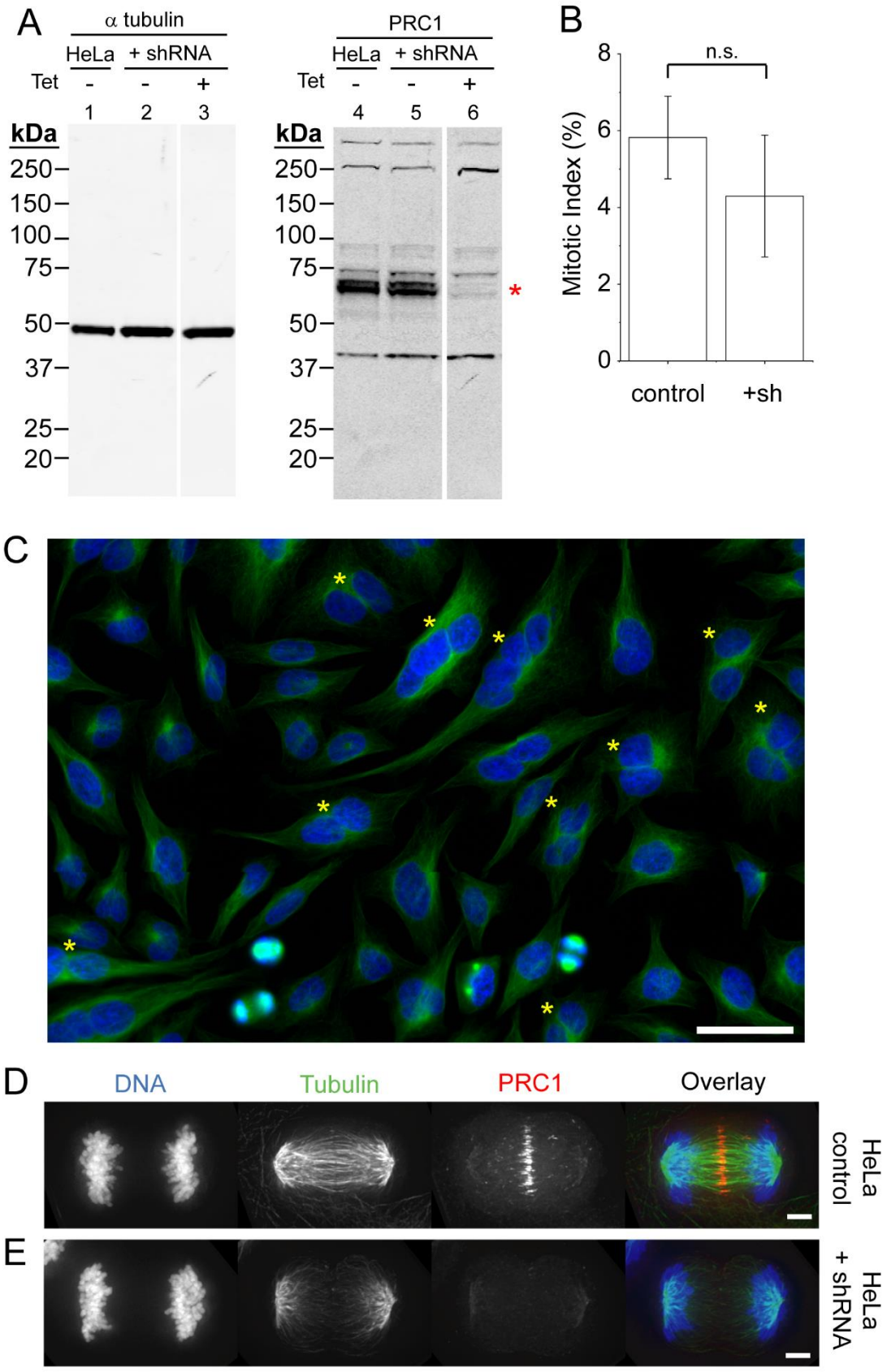
A
α tubulin
HeLa
+ shRNA
Tet
-
-
+
1
2
3
kDa
250
150
100
75
50
37
25
20
PRC1
HeLa
+ shRNA
Tet
-
-
+
4
5
6
kDa
250
150
100
75
50
37
25
20
*
B
n.s.
Mitotic Index (%)
8
6
4
2
0
control
+sh
C
*
D
DNA
Tubulin
PRC1
Overlay
HeLa
control
E
HeLa
+ shRNA

To examine the consequence of PRC1 knockdown on chromosome position in anaphase, we performed live cell imaging using a spinning disk confocal setup. We used differential interference contrast (DIC) and fluorescence microscopy to monitor cell morphology and chromosome position, respectively (**Fig. 4.8 A-D**). To confirm that the defects associated with PRC1 knockdown were specific, we generated "addback" cells expressing both shRNA to endogenous PRC1 and shRNA-resistant GFP-PRC1 (hereafter, "GFP-PRC1") (see **Methods**). In GFP-PRC1 cells, we also monitored GFP fluorescence (**Fig 4.8 C**). In each cell line, furrow ingression initiated at a similar time following anaphase onset (**Fig. 4.8 A-C**). We did not detect an increased incidence of lagging chromosomes in shPRC1 cells (**Fig. 4.8 B**). GFP-PRC1 cells appeared morphologically similar to control cells (**Fig. 4.8 C**).

We first tracked chromosome position, taken as the centroid of the chromosome mask (**Fig. 4.8 D**, yellow squares), to monitor inter-chromosome distance (**Fig. 4.9 A**). Almost immediately after anaphase onset, we noticed that the distance between chromosomes was consistently larger in shPRC1 cells (n = 19) (**Fig. 4.9 A**, blue trace) compared to control (n = 15) (**Fig. 4.9 A**, black trace) or GFP-PRC1 cells (n = 14) (**Fig. 4.9 A**, gray trace). We examined cells at T = 5 mins which precedes furrow ingression in >90% of cells and according to our LLS data is after PRC1-tagged microtubule bundles reach an equilibrium length. Chromosomes in shPRC1 cells had segregated 20% further than control cells by this time (14.5 +/- 1.4 μm and 11.9 +/- 1.5 μm, respectively, +/- SD) (**Fig. 4.9 B**). This "hyper-segregation" defect was statistically significant ($p < 0.003$, two-tailed T-test). Expression of GFP-PRC1 rescued this defect (12.1 +/- 1.5 μm, +/- SD) (**Fig. 4.9 B**).

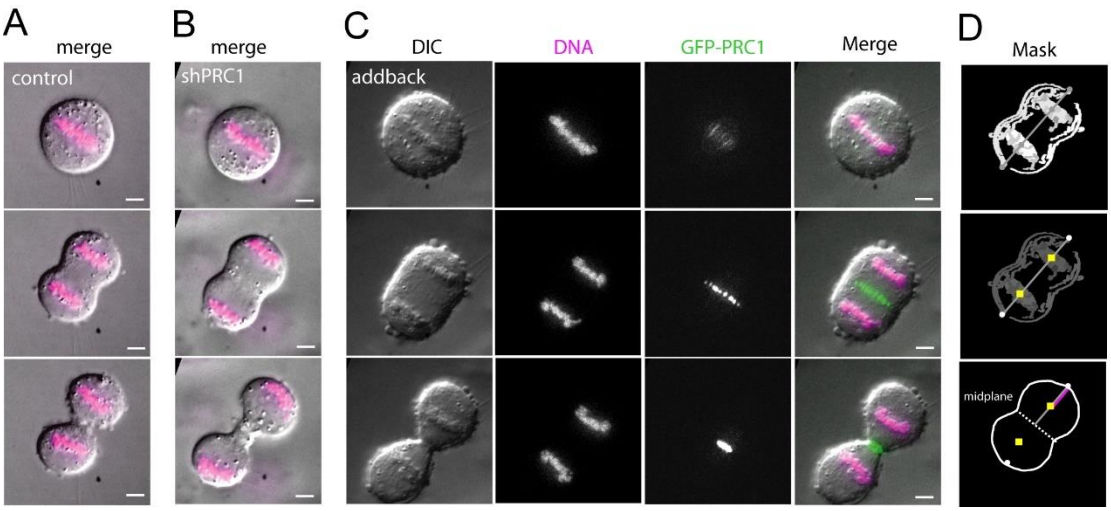

Figure 4.8. Live cell imaging of HeLa cells expressing shRNA to PRC1

(**A-C**) Live cell imaging of HeLa cells. Single channel (single z slice) and overlay images show differential interference contrast (DIC) images (gray), chromosomes (magenta), and GFP-PRC1 (green) in HeLa control (**A**), shPRC1 (**B**) and GFP-PRC1 (**C**) cells. T = 0 was assigned to the frame immediately prior to that with detectable chromatid separation. Scale bar, 3 μm. (**D**) Segmented binary image showing outline of cortex and chromosome mask corresponding to images shown in (**B**). Overlay shows the position of chromosome centroid (yellow squares), the position of the midplane (dotted line), the axis of chromosome segregation (gray line), and the distance from chromosome to cortex (pink line) are indicated.

Figure 4.9. PRC1 knockdown results in increased chromosome segregation rates and leads to chromosome "hyper-segregation".

(**A-H**) Analysis of chromosome and cortical position in HeLa control (black), shRNA (blue), and GFP-PRC1 (grey) cells. Average +/- SD. (**A-B**) Inter-chromosome distance over time (**A**) and at T = 5 min (**B**) (control: 14.5 +/- 1.4 μm; shPRC1: 11.9 +/- 1.5 μm; GFP-PRC1: 12.1 +/- 1.5 μm). ($p < 0.003$). (**C-D**) Cell length over time (**C**) and at T = 5 min (**D**) (control: 23.9 +/- 1.4 μm; shPRC1: 22.8 +/- 1.4 μm; GFP-PRC1: 24.3 +/- 1.3 μm) ($p > 0.07$). (**E-F**) Chromosome-to-cortex distance over time (**E**) and at T = 5 min (**F**) (control: 6.0 +/- 0.9 μm; shPRC1: 4.2 +/- 0.5 μm; GFP-PRC1: 5.9 +/- 0.7 μm) ($p << 0.0001$). (**G-H**) Fraction chromosome distance to cortex over time (**G**) and at T = 5 min (**H**) (control: 0.50 +/- 0.06; shPRC1: 0.63 +/- 0.04; GFP-PRC1: 0.50 +/- 0.06) ($p << 0.0001$).

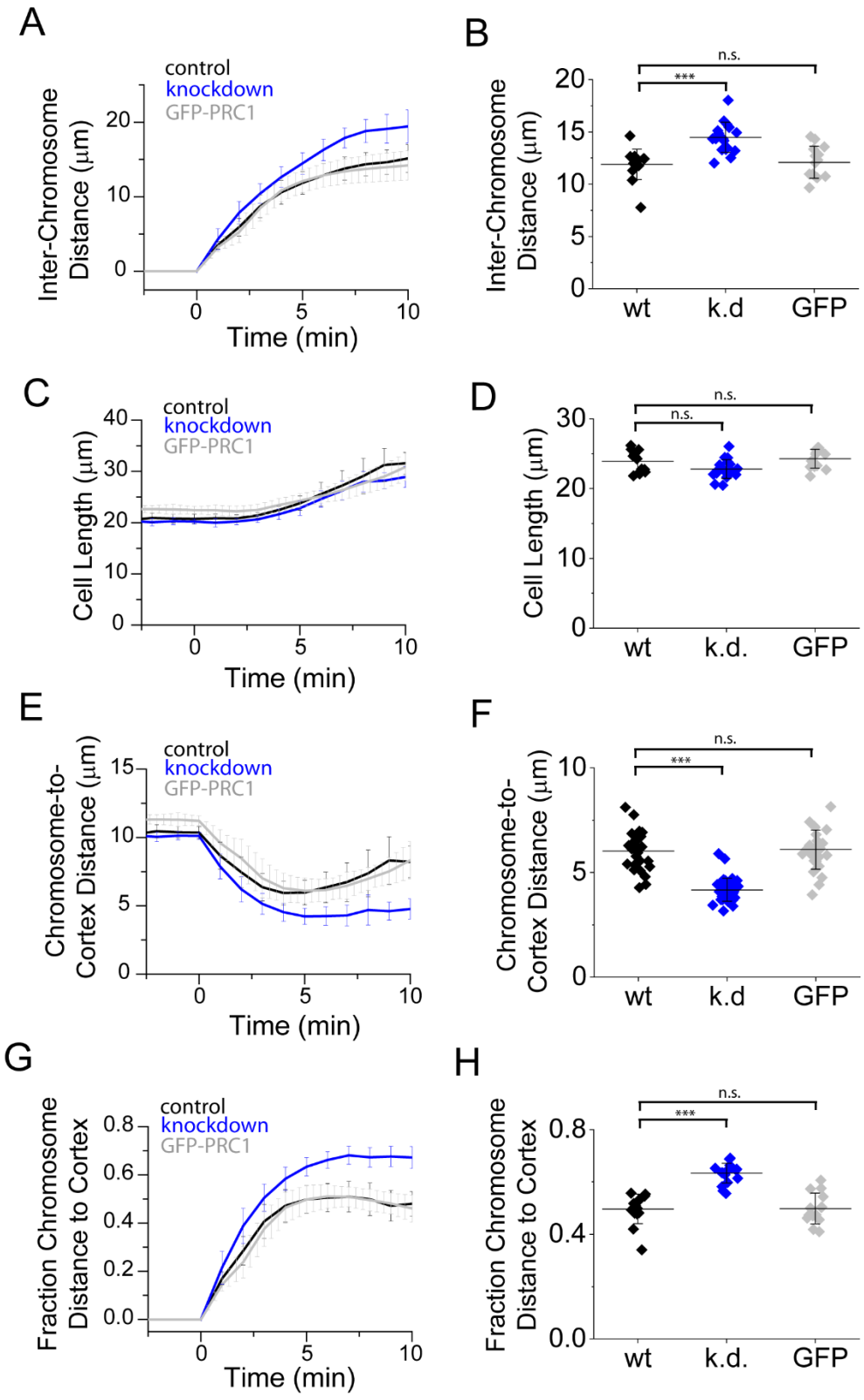
A
control
knockdown
GFP-PRC1
Inter-Chromosome Distance (μm)
Time (min)
B
n.s.
***
Inter-Chromosome Distance (μm)
wt
k.d
GFP
C
control
knockdown
GFP-PRC1
Cell Length (μm)
Time (min)
D
n.s.
n.s.
Cell Length (μm)
wt
k.d.
GFP
E
control
knockdown
GFP-PRC1
Chromosome-to-Cortex Distance (μm)
Time (min)
F
n.s.
***
Chromosome-to-Cortex Distance (μm)
wt
k.d
GFP
G
control
knockdown
GFP-PRC1
Fraction Chromosome Distance to Cortex
Time (min)
H
n.s.
***
Fraction Chromosome Distance to Cortex
wt
k.d.
GFP

To exclude the possibility that shPRC1 cells are simply larger and thereby are less restrictive of spindle elongation, we examined the length of cells during anaphase. Cell elongation in all three cell lines and began ~3 μm after anaphase onset (**Fig 4.9 C**). We found that the average length of shPRC1 cells at 5 mins was similar to control cells (22.8 +/- 1.4 μm and 23.9 +/- 1.4 μm, respectively; $p > 0.07$) (**Fig. 4.9 D**). These data suggest that PRC1 levels do not impact cell elongation during anaphase.

We next examined the distance between chromosomes and the cell cortex (**Fig. 4.9 E**). Control and GFP-PRC1 cells showed a characteristic decrease in chromosome-to-cortex distance from anaphase onset to ~5 mins, followed by an increase. This increase after ~5 mins was not observed in shPRC1 cells. Compared to control cells, chromosomes in shPRC1 cells were positioned closer to the cortex by 5 mins into anaphase (4.2 +/- 0.5 μm and 6.0 +/- 0.9 μm, respectively; +/- SD) and this difference was significant ($p << 0.0001$) (**Fig. 4.9 F**). The expression of GFP-PRC1 rescued this defect.

This defect was more apparent when we examined the fraction distance to the cortex, measured as the distance between the chromosomes and the cortex (**Fig 4.8 D**, magenta line) divided by the distance between the midplane and the cortex (**Fig 4.8 D**, gray line). The chromosomes in control and GFP-PRC1 cells segregated until reaching ~50% of the distance between the midplane and the cortex, while those in knockdown cells moved a larger fractional distance (**Fig 4.9 G**). By 5 mins, this fractional distance was 0.50 +/- 0.06 and 0.63 +/- 0.04 for control and knockdown cells, respectively, (+/- SD) and this difference was significant ($p << 0.0001$) (**Fig 4.9 H**). Together, these data suggest that the function of the spindle midzone is to act as a "brake" in anaphase to restrict chromosome segregation speed and distance.

PRC1 knockdown increases rates of pole separation but not kinetochore-to-pole movement

To examine how PRC1 knockdown impacts the rate of chromosome segregation, we simultaneously tracked centrosomes and pole position in anaphase spindles. We used hTERT-RPE1 cells expressing GFP-Centrin and GFP-CENP-A (hereafter, control cells) and compared these rates to those expressing shRNA to PRC1 (hereafter, shPRC1). The efficiency of knockdown was 80 +/- 8% and PRC1 signal was absent or below the level of detected in 85% of anaphase cells (n = 13 cells). We imaged live cells using a spinning disc confocal setup which allowed simultaneous monitoring of spindle poles and centrosomes (**Fig. 4.10 A-D**), as has been extensively done (refs) (Magidson et al., 2011).

In control cells, GFP fluorescence could be detected on centrosomes and near spindle poles (**Fig. 4.10 A** and **B**). A similar profile of fluorescence localization was observed in shPRC1 cells (**Fig. 4.10 C** and **D**). We could often detect two distinct spots near spindle poles, likely indicating position of mother and daughter centriole (**Fig. 4.10 A** and **C**, yellow arrows). Examination of single image planes over time highlight the position of centrosomes on sister chromatids during the first 60 s of anaphase (**Fig. 4.10 B** and **D**, orange and yellow circles). Kymographs generated by drawing linescans across the pole-to-pole axis from the time lapse sequences in **Figures 4.10 A** and **C** showed that chromosomes in shPRC1 cells segregated without an increased incidence of lagging chromosomes compared to control (**Fig. 4.10 E** and **F**).

Figure 4.10. PRC1 knockdown increases rates of pole separation but not kinetochore-to-pole movement.

(**A-D**) Analysis of centromere and pole position by live cell fluorescence microscopy of hTERT-RPE1 cells co-expressing GFP-centrin and GFP-CENP-A. Select images from time series are shown. (**A-B**) A control cell. (**C-D**) A cell expressing shRNA targeting PRC1. (**A** and **C**) Maximum intensity projections. Mother and daughter centrioles are observed as two proximal spots (yellow arrows). (**B** and **D**) Single image planes showing consecutive images (15s intervals) from a single cell at anaphase. Selected kinetochore pairs are highlighted (orange and yellow circles). (**E** and **F**) Kymograph ... pole-to-pole axis from cells shown in (**A**) or (**C**). Horizontal scale bar, 3 um. Vertical scale bar, 2 mins. (**G-H**) Analysis of normalized kinetochore-to-pole distance. Traces from individual kinetochores from a representative cell in each condition are shown. Average of all traces is shown in bold. Error bars are S.D. (**G**) Representative control cell. (**H**) Representative knockdown cell. (**I**) Box and whisker plots with corresponding data fit to a gaussian of kinetochore-to-pole velocity. Data were pooled data from all experiments (n = 59 and 111 kinetochores for control and knockdown cells, respectively). (**J**) Plots of pole-to-pole distance for control (black traces) and knockdown (red traces) cells (n = 12 and 21 cells, respectively). (**K**) Plot of pole separation distance, ΔLength, normalized to the pole-to-pole distance at T = 0. (**L**) Pole separation velocity for control and knockdown cells (*** = $p < 0.003$).

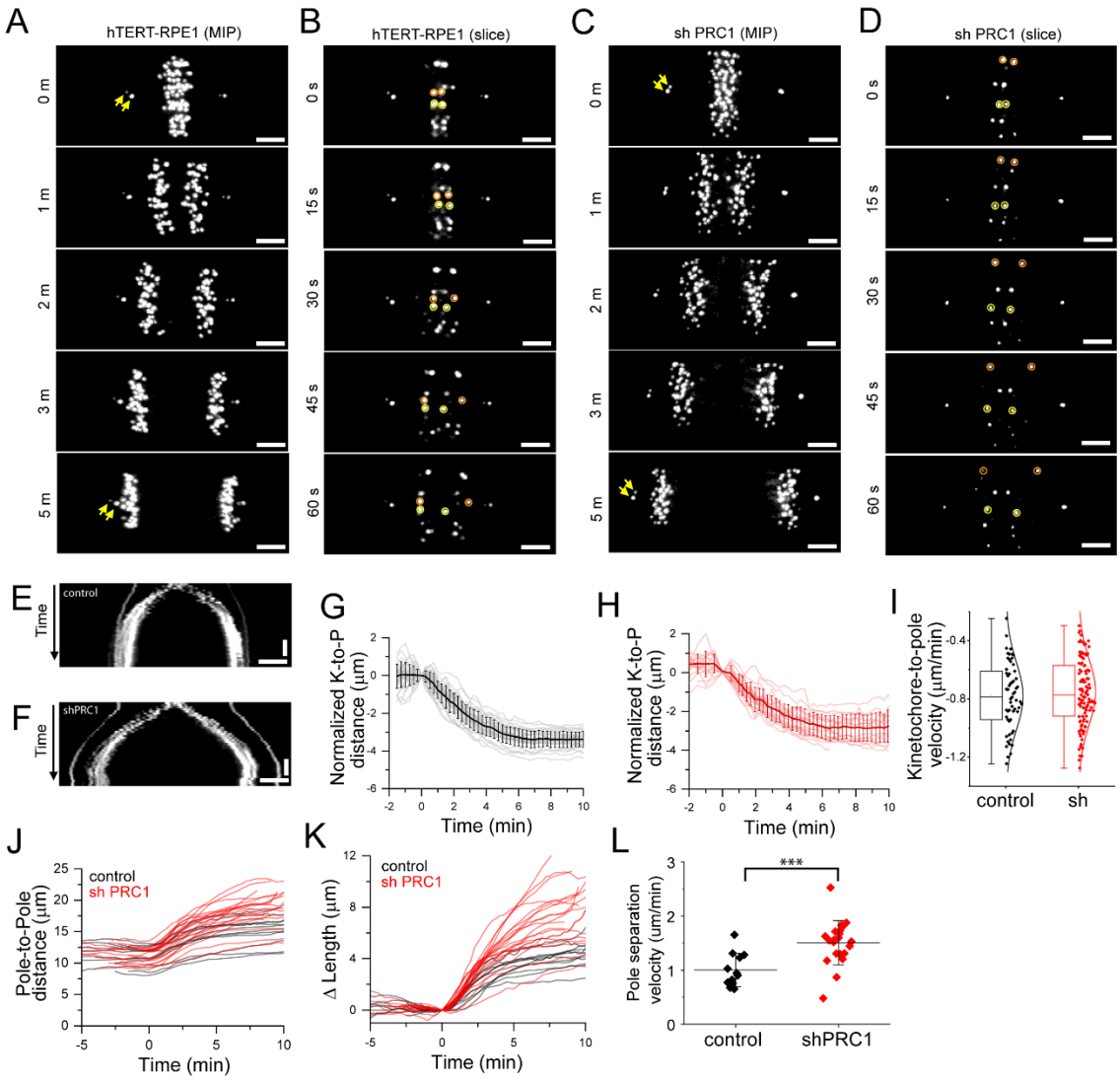
A
hTERT-RPE1 (MIP)
0 m
1 m
2 m
3 m
5 m
B
hTERT-RPE1 (slice)
0 s
15 s
30 s
45 s
60 s
C
sh PRC1 (MIP)
0 m
1 m
2 m
3 m
5 m
D
sh PRC1 (slice)
0 s
15 s
30 s
45 s
60 s
E
Time
control
F
Time
shPRC1
G
Normalized K-to-P distance (µm)
Time (min)
H
Normalized K-to-P distance (µm)
Time (min)
I
Kinetochore-to-pole velocity (µm/min)
control
sh
J
Pole-to-Pole distance (µm)
control
sh PRC1
Time (min)
K
Δ Length (µm)
control
sh PRC1
Time (min)
L
Pole separation velocity (um/min)
***
control
shPRC1

We reasoned that the observed increase in chromosome segregation speed could be due to an increase in anaphase A kinetochore-to-pole shrinkage rates or due to an increase in anaphase B pole separation rates. To distinguish between these possibilities, we first examined kinetochore-to-pole distance over time using a 3D localization and tracking algorithm (see Methods). We were able to track kinetochore position from anaphase onset through kinetochore release, identified by a synchronous increase in kinetochore-to-pole distance. In control cells, tracks of individual kinetochores revealed a decrease in kinetochore-to-pole distance over time (**Fig. 4.10 G**) which was mirrored in PRC1 knockdown cells (**Fig. 4.10 H**). To determine the average rate of kinetochore-to-pole movement, we focused on the T = 0.5-3 min time window when this rate is reported to be fastest (Su et al., 2016). We pooled the rates for individual kinetochore tracks that had fits with R-squared values >= 0.85 (**Fig 4.10 I**). The average rate of kinetochore-to-pole movement for parental cells, 0.78 +/- 0.23 μm/min (n = 59 kinetochores, +/- SD), was not significantly different than that for PRC1 knockdown cells, 0.75 +/- 0.23 μm/min (n = 111 kinetochores, +/- SD; p>0.1). Thus, PRC1 knockdown does not impact the average rate of anaphase A kinetochore-to-pole movement.

We next tracked the pole-to-pole distance as a function of time (**Fig. 4.10 J**). In control cells, the pole-to-pole distance began to increase immediately after anaphase onset in control (**Fig. 4.10 J**, black traces) and PRC1 knockdown cells (**Fig. 4.10 J**, red traces). Traces for all control and knockdown cells are shown (n = 12 and 21 cells, respectively). A plot of the change in anaphase spindle length, ΔLength, as a function of time highlighted differences in the rate of pole separation (**Fig. 4.10 K**). Examination of first derivative plots of pole-to-pole distances over time revealed that 94% of spindles underwent maximum

pole separation velocities between 1-3 mins after anaphase onset (n = 33 cells). We therefore determined the pole-to-pole separation rates by fitting the data from T = 1 to T = 3 to a line for each cell (**Fig 4.10 L**). Spindles in control cells elongated at an average rate of 0.98 +/- 0.31 μm/min (n = 11 cells, +/- SD) whereas spindles in knockdown cells elongated ~50% faster at 1.51 +/- 0.41 μm/min (n = 21 cells, +/- SD, $p < 0.003$). Thus, the rates of anaphase B spindle elongation is substantially increased as a result of PRC1 knockdown. Together, these data show that the midzone brake functions by limiting the rate of pole separation.

Mutations in PRC1 that reduce microtubule binding affinity can form microtubule bundles but cannot rescue chromosome hyper-segregation defects

The midzone braking function is likely due to a convolution of microtubule overlap length and bundle number. We therefore attempted to find conditions where we could selectively perturb overlap length control in the spindle without impacting bundle number. Structural studies have revealed the molecular basis for PRC1-microtubule cross-linking (Kellogg et al., 2016; Subramanian et al., 2010, 2013). We generated two mutant constructs, one with point mutations K387A and K390A in the spectrin domain (hereafter, GFP-PRC1^{AA}), and one with a truncation of the terminal 464-620 residues in the unstructured C-terminus (hereafter, GFP-PRC1$^{\Delta C}$). The point mutations in GFP-PRC1^{AA} are unlikely to disrupt binding to MAPs but reduce microtubule binding affinity ~4-fold. The truncation in GFP-PRC1$^{\Delta C}$ reduces microtubule binding affinity ~5-fold and also likely disrupts interaction with some MAPs that interact with PRC1 at the C-terminus.

These constructs have been previously examined *in vitro* and have been shown to dimerize, a necessary prerequisite for microtubule cross-linking (Subramanian et al., 2010, 2013).

To reveal the function of mutant PRC1 in cells, we knocked down endogenous PRC1 using our shRNA-based system and expressed shRNA-resistant PRC1 constructs. We examined three constructs, full-length GFP-PRC1 (hereafter, GFP-PRC1^{FL}) and our two mutant constructs, GFP-PRC1^{AA} and GFP-PRC1$^{\Delta C}$. Western blot analysis of metaphase-arrested cell lysates showed that the expression levels of the GFP constructs were comparable to endogenous PRC1 in control cells (GFP-PRC1^{FL}: 69 +/- 44%, n = 3; GFP-PRC1^{AA}: 140 +/- 95%, n = 4) and knockdown efficiency was high (GFP-PRC1^{FL}: 94 +/- 1%, n = 3; GFP-PRC1^{AA} : 93 +/- 3%, n = 4) (**Fig. 4.11 A**). Knockdown efficiency of GFP-PRC1$^{\Delta C}$ could not be reliably measured because GFP-PRC1$^{\Delta C}$ ran at a similar distance as the endogenous PRC1 protein. However, western blots revealed a GFP-reactant band in the expected position, indicating that the protein was expressed in cells (**Fig. 4.11 B**). Immunofluorescence analysis of fixed cells showed that the decoration of GFP-PRC1^{FL} appeared similar to unmodified control cells (**Fig. 4.12 A**). GFP-PRC1^{AA} decorated microtubules in the midzone in anaphase cells (**Fig. 4.12 B**). Despite substantial levels of GFP-PRC1$^{\Delta C}$ overexpression, we did not detect PRC1 signal above background on any anaphase cells (**Fig. 4.12 C**). These cells looked morphologically similar to knockdown alone (**Fig. 4.7 E**) and we did not examine this line further.

When comparing cells with equivalent chromosome segregation distances, we noticed that the decoration of GFP-PRC1^{AA} tended to be wider than that of GFP-PRC1^{FL}. To quantify this distribution, we measured the full-width at half-maximum signal across

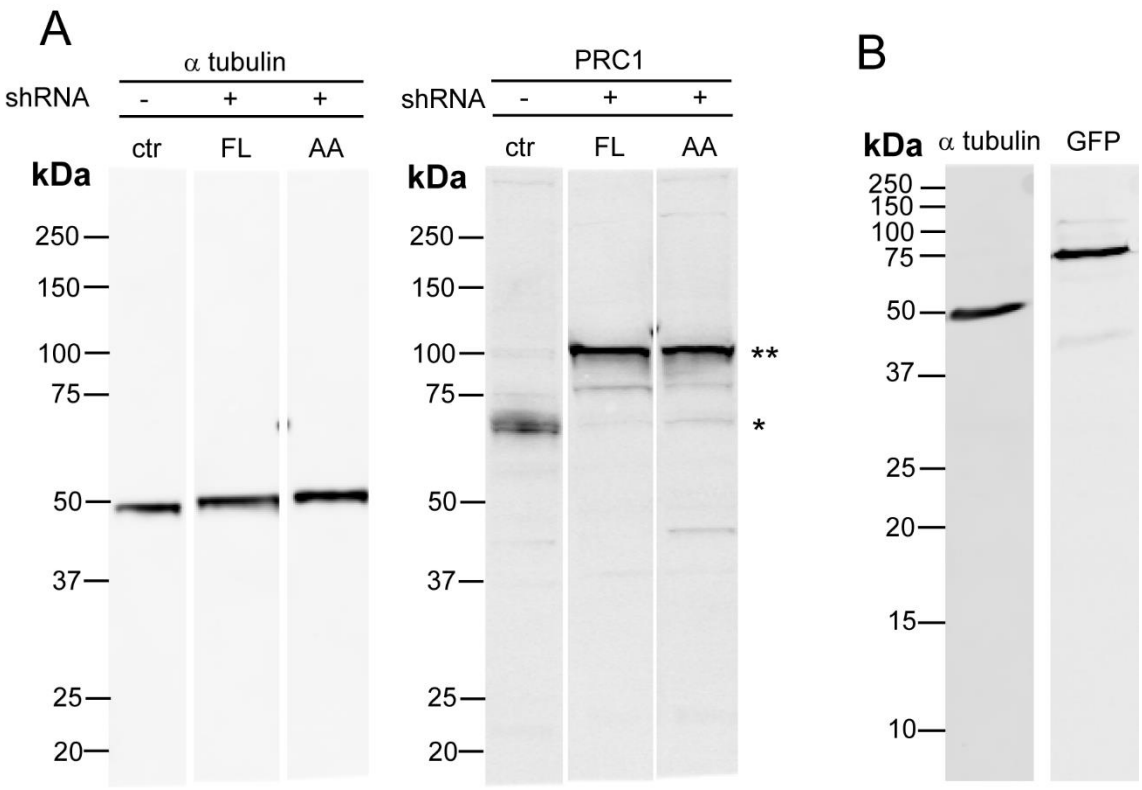

Figure 4.11. Western blot analysis of HeLa cells expressing shRNA to PRC1 and shRNA-resistant GFP-PRC1 constructs.

(A-B) Western blot analysis of metaphase-arrested cell lysates from HeLa cell lines. (**A**) Samples from HeLa control cells (ctr), HeLa cells expressing shRNA to PRC1 and GFP-PRC1^{FL} (FL) or GFP-PRC1^{AA} (AA) 72 hrs after adding tetracycline. Antibodies against α tubulin and PRC1 are indicated. Expected position of endogenous PRC1 (single asterisk) and GFP-tagged PRC1 (double asterisk) is indicated. (**B**) Samples from HeLa cells expressing shRNA to PRC1 and GFP-PRC1$^{\Delta C}$ 72 hrs after adding tetracycline. Antibodies against α tubulin and GFP are indicated.

Figure 4.12. Mutations in PRC1 that reduce microtubule binding affinity can form microtubule bundles but cannot rescue chromosome hyper-segregation defects.

(**A-C**) Immunofluorescence analysis of anaphase cells. Single channel images (maximum intensity projections) and overlays show chromosomes (blue), PRC1 (red) and tubulin (green). GFP fluorescence (maximum intensity projection) is shown as reference (gray). HeLa cells co-expressing shRNA to endogenous PRC1 and shRNA-resistant GFP-PRC1^{FL} (**A**), GFP-PRC1^{AA} (**B**), or GFP-PRC1$^{\Delta C}$ (**C**). Scale bar, 3 μm. (**D-E**) Analysis of GFP-PRC1 signal intensity. Plots show intensity of PRC1 signal in linescans drawn across the pole-to-pole axis. Data were fit to a gaussian (red traces) to determine the full-width at half-maximum (FWHM) signal. Example traces from cells expressing GFP-PRC1^{FL} (**D**) and GFP-PRC1^{AA} are shown. (**F-G**) Data from cells expressing GFP-PRC1^{FL} (gray) and GFP-PRC1 ^{AA} (red) are shown. (**F**) Bar chart of average FWHM, binned by inter-chromosome distances. Error bars are SD. (**G**) Histogram of the number of anaphase cells with a given inter-chromosome distance. n = 53 (GFP-PRC1^{FL}) and 28 (GFP-PRC1^{AA}) cells.

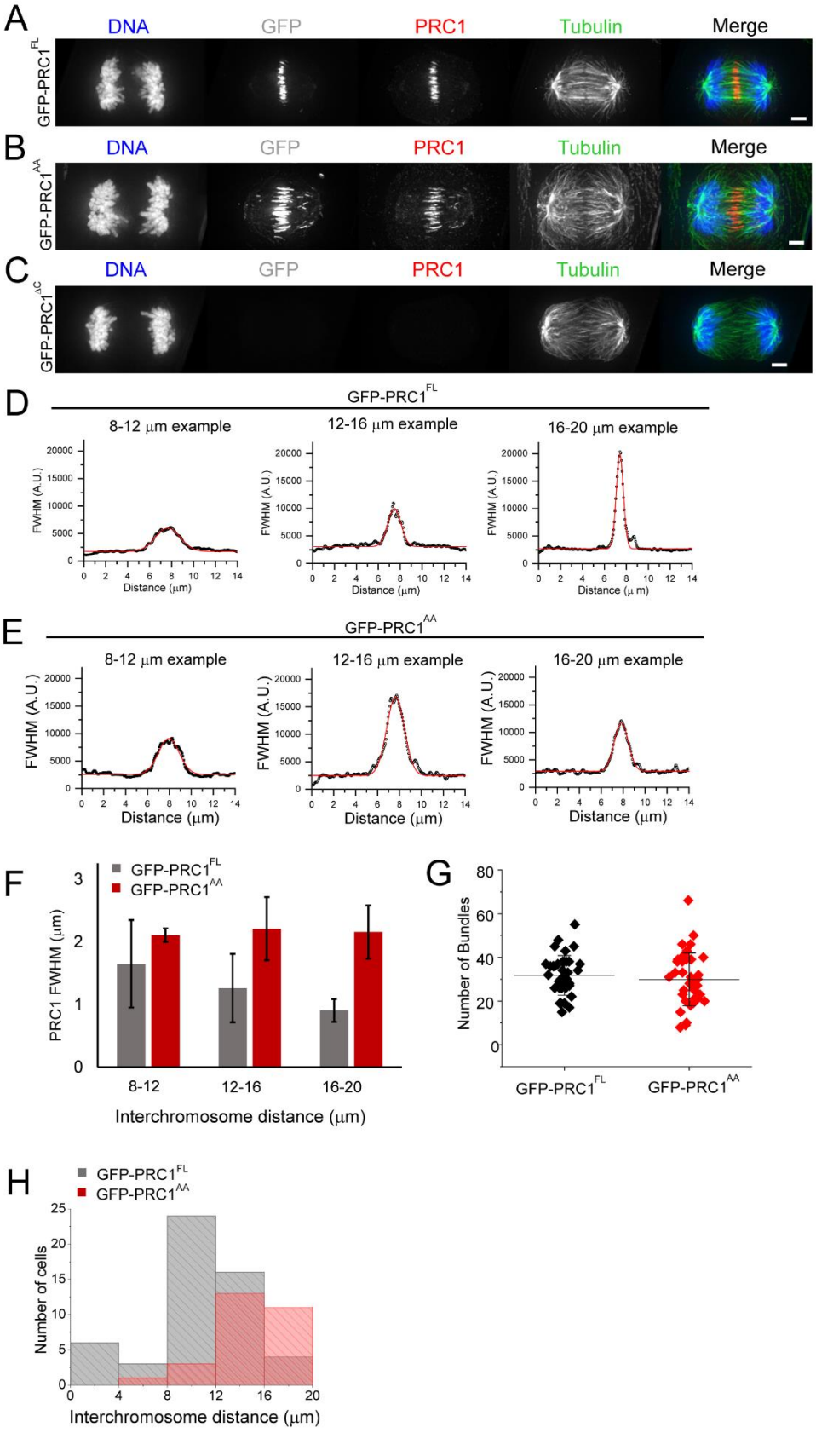
A
DNA
GFP
PRC1
Tubulin
Merge
GFP-PRC1FL
B
GFP-PRC1AA
C
GFP-PRC1ΔC
D
GFP-PRC1FL
8-12 μm example
12-16 μm example
16-20 μm example
FWHM (A.U.)
Distance (μm)
E
GFP-PRC1AA
F
GFP-PRC1FL
GFP-PRC1AA
PRC1 FWHM (μm)
8-12
12-16
16-20
Interchromosome distance (μm)
G
Number of Bundles
GFP-PRC1FL
GFP-PRC1AA
H
GFP-PRC1FL
GFP-PRC1AA
Number of cells
Interchromosome distance (μm)

the pole-to-pole axis from maximum intensity images of fixed cells. Gaussian fits with R2 values > 0.90 were selected. As cell-to-cell expression levels were variable, this filter also excluded cells with little to no detectable GFP fluorescence (manual inspection showed that excluded cells typically had SNR values below 2). In each cell, we also measured the inter-chromosome distance, and used this to separate the data into 4-μm bins. Example plots for cells expressing GFP-PRC1^{FL} (**Fig. 4.12 D**) and GFP-PRC1^{AA} (**Fig. 4.12 E**) are shown. The FWHM signal of GFP-PRC1^{FL} decreased with increasing inter-chromosome distance, indicating a reduction in the length of microtubule overlap (**Fig. 4.12 F**, gray). This trend was not observed in cells expressing GFP-PRC1^{AA} . Instead, the FWHM measurement was similar for cells with different inter-chromosome distances (**Fig. 4.12 F**, red), indicating that microtubule overlap length did not decrease as chromosomes separated. Together, these data suggest that midzone microtubule overlap length can be decoupled from chromosome segregation distance by tuning the affinity of PRC1 to microtubules.

Our analyses indicate that the control of microtubule overlap length is impaired in cells expressing GFP-PRC1^{AA} . We next asked whether the cross-sectional organization was also disrupted. We examined cells in mid-late anaphase (chromosome segregation distance 12-16 μm) and determined the number of microtubule bundles in GFP-PRC1^{FL} and GFP-PRC1^{AA} cells. The average number of microtubule bundles was similar (GFP-PRC1^{FL}: 32 +/- 9, GFP-PRC1^{AA} : 30 +/- 12, +/- SD, $p > 0.4$) (**Fig. 4.12 G**). These data suggest that GFP-PRC1^{AA} does not prevent the assembly of microtubule bundles.

We next examined the distribution of chromosome segregation distance in anaphase cells expressing detectable GFP-PRC1^{FL} and GFP-PRC1^{AA} (**Fig. 4.12 H**). Only

a small fraction (<10%) of anaphase cells expressing GFP-PRC1^{FL} were found to exhibit inter-chromosome distances greater than 16 um, suggesting that this is the upper limit to chromosome segregation distance. (**Fig. 4.12 H**, gray). By contrast, numerous cells expressing GFP-PRC1^{AA} were observed with this inter-chromosome distances greater than 16 µm, some up to 20 µm (**Fig. 4.12 H**, red). This chromosome "hyper-segregation" defect was similar to that observed in PRC1 knockdown cells alone (**Fig. 4.8 E-F**). Given that PRC1 knockdown does not prolong the onset of furrow ingression (**Fig. 4.8 A-C**), this result is unlikely to be explained simply by extending the time of anaphase. Together, these data suggest that the reduction of overlap length between filament in midzone microtubule bundles is required to function as a "brake" to control chromosome segregation during anaphase.

4.4 Discussion

Our data show that PRC1-dependent spindle midzone assembly is required for proper chromosome segregation. In early anaphase, PRC1-tagged microtubule bundles can push sister chromatids apart when the connection to one spindle pole is severed (Vukušić et al., 2017). Our data show that when PRC1 is knocked down, midzone microtubule bundle assembly is impaired and the speed of chromosome segregation is increased. This suggests that PRC1-tagged microtubule bundles can also act as a "brake" to restrict chromosome movement in anaphase. We express a mutant PRC1 construct with reduced microtubule binding affinity that impacts microtubule overlap length without impacting microtubule bundle number. Overlap length does not decrease during anaphase and chromosome "hyper-segregation" defects are observed. This suggest that the reduction of microtubule overlap length is required for the braking activity of the spindle midzone.

Our lattice light sheet imaging data reveal that the average microtubule overlap length shrinks after anaphase onset until reaching a stable length that persists for several minutes. However, the distribution of bundle lengths was broad, even in early anaphase, suggesting that both short (< 2 μm) and long (> 4 μm) bundles are present throughout anaphase. Examination of individual bundles revealed apparent "fusion" events and fluctuations in bundle number that precluded automated tracking of all bundles. However, manual tracking of a subset of microtubule bundles near the outer periphery of the spindle revealed that long (> 4 μm) overlap typically decreased in length faster than what we predicted from the bulk data. Recent studies have revealed that PRC1-tagged microtubule bundles in metaphase show a one-to-one association with sister k-fibers (Polak et al., 2017). We predict that fusion events in anaphase could cause the network of PRC1-tagged

microtubule bundles and k-fibers to increase in complexity such that a single bundle could become associated with multiple k-fibers during anaphase. Indeed, electron micrograph studies have revealed that the minus ends of microtubules in a single midzone bundle often terminate in several different k-fibers on one side of the half-spindle (Mastronarde, 1993). Together, these data suggest that microtubule bundles in the spindle midzone are flexible enough to accommodate chromosome segregation but robust enough to maintain its structure.

How can midzone bundles act as a brake in the face of changing overlap? Budding yeast Ase1 can concentrate in microtubule overlap regions as the length of overlap decreases, creating an "entropic expansion" force that can resist filament sliding (Braun et al., 2011; Lansky et al., 2015). This activity likely depends on a low molecular off-rate of Ase1 in overlap (Braun et al., 2011). Our FRAP analysis of GFP-PRC1 in early-mid anaphase spindles shows that GFP-PRC1 turnover is relatively fast (t ½ = 36 +/- 9 s), at least 10x faster than that observed for GFP-Ase1 in the budding yeast midzone (Schuyler et al., 2003), suggesting that PRC1 is unlikely to undergo an Ase1-like compaction. PRC1 (620 aa) and Ase1 (883 aa) are both members of the same conserved protein family, but have a low degree of sequence similarity with only 23% identity over a stretch of 331 amino acids (Jiang et al., 1998; Mollinari et al., 2002; Schuyler et al., 2003). Divergence between Ase1 and PRC1 activity in the midzone is likely a result of functional specialization of Ase1 in the yeast lineage. Together, these data suggest that PRC1 likely works in concert with other molecules to provide the vertebrate midzone braking activity.

PRC1 mediates the recruitment of midzone-associated proteins including kinases, non-motor microtubule associated proteins (MAPs), and motor MAPs (Roostalu et al.,

2010). Eg5, a homotetrameric Kinesin-5 family member, is recruited to the midzone in a PRC1-dependent manner (Ferenz et al., 2010). Eg5 can slide antiparallel microtubules apart and is required in human cells to establish spindle bipolarity in metaphase (Ferenz et al., 2010). Inhibition of this protein in anaphase does not cause spindle collapse, suggesting that antiparallel sliding activity is not critical for maintaining the spindle midzone. *In vitro* data has revealed that Eg5 can also resist filament sliding, an activity that scales with number of molecules and length of overlap (Shimamoto et al., 2015). Our data reveal that cells expressing mutant PRC1 form microtubules bundles with longer overlap length, thus providing more binding sites to Eg5, which would predict an increase in braking. However, we observe the opposite effect as chromosomes in these cells still "hyper-segregate" as observed in the knockdown alone, suggesting that the midzone brake is not functional. This suggests that the mechanism of PRC1-dependent midzone braking is unlikely to be due to an Eg5-like brake.

In vitro, PRC1 forms a complex with Kif4 and together these proteins can function in two ways: to suppress microtubule dynamics and to slide microtubules apart. When the minus-ends of microtubules are anchored (preventing filament displacement), PRC1/Kif4 can form stable microtubule overlaps through Kif4-dependent inhibition of microtubule plus-end dynamics (Bringmann et al., 2004; Bieling et al., 2010). This activity is likely important in cells, as Kif4 is required to suppress plus-end dynamics of midzone microtubules (Hu et al., 2011). Recently, experiments using unanchored, non-dynamic microtubules have shown that PRC1-Kif4 complexes can generate relative movement of antiparallel microtubules (Wijeratne and Subramanian, 2018). Kif4 alone does not promote antiparallel microtubule cross-linking, suggesting that the formation of a sliding competent

complex depends on PRC1 interaction with microtubules to move one filament while the motor walks on the other. To examine the impact of reducing PRC1 affinity for microtubules, we expressed a mutant PRC1 and examined cells in anaphase. In these cells, antiparallel microtubules overlap length does not reduce during anaphase, suggesting that relative filament sliding is impaired. According to the above model, a reduction in PRC1-microtubule binding affinity would likely results in a lower "sliding efficiency" as each step of the kinesin would not translate to an equivalent distance moved if PRC1 were not simultaneously bound to the second MT. These data suggest that the coupling between antiparallel microtubules is reduced, resulting in a dissipation of forces (both pushing and breaking) generated in antiparallel overlaps.

How might microtubule in bundles interact with spindle elements that contact the poles? The minus-ends of midzone bundles are distal to the site of microtubule overlap and are thought to be inhibited by capping proteins that block polymerization. Part of the challenge in identifying the position of minus ends in dividing cells is the lack of minus-end markers. Calmodulin-regulated spectrin-associated protein (CAMSAP)-family members have been shown to stabilize minus ends and protect them from kinesin-13 mediated depolymerization in interphase Drosophila S2 cells and in controlled *in vitro* assays (Goodwin and Vale, 2010; Hendershott and Vale, 2014). Knockdown of Patronin leads to mitotic defects in Drosophila S2 cells (Goshima et al., 2007). However, mitotic defects were not observed in HeLa cells following knockdown of mammalian CAMSAP2, perhaps due to functional redundancy with other expressed CAMSAP proteins (Jiang et al., 2014). Furthermore, direct interaction with minus ends of any of these proteins in dividing cells has not been shown. Other candidate minus-end interacting molecules

include dynein/dynactin and NuMA which form a complex in dividing cells and together promote minus-end focusing and pole formation. Newly formed minus ends generated by laser cutting are capped by this complex within 15 s (Elting et al., 2014). Dynein generates forces on spindles through minus-end directed pulling on astral microtubules from cortically anchored position, which is dependent on NuMA. Knockdown of either dynein or NuMA results in metaphase spindle defects thus acute chemical inhibition-based approaches are needed in order to dissect their anaphase-specific functions.

In summary, our data reveal that PRC1-dependent microtubule bundle formation is required for midzone braking. We further show that this activity depends on the reduction in microtubule overlap length. Microtubule bundles are found in diverse cell contexts and the recruitment of cross-linking proteins in these arrays is likely to be tightly controlled in these contexts as well. Additional work will be needed to examine how other features, such as the number or packing of filaments in bundles, impact the function of microtubule bundles.

Chapter 5: Outlook and Future Directions

5.1 Overview

Microtubule dynamic instability is a fundamental property of microtubules required for proper microtubule function in diverse cellular activities including cell division. During anaphase, a subset of microtubules are selectively stabilized and cross-linked, forming the spindle midzone. Understanding the mechanism of dynamic instability is a prerequisite for understanding how microtubule-associated proteins modulate dynamics and in turn control microtubule architecture in cells. In my PhD work, I first examined microtubule dynamics assembled from purified human tubulin *in vitro* and then examined midzone function during anaphase in dividing human cells.

5.2 Open questions in dynamic instability

Both α and β tubulin are conserved proteins found in all eukaryotes studied to date, with most organisms expressing multiple isotypes of each tubulin. Current studies suggest that tubulin isotypes, in combination with post-translational modifications, regulate tubulin dynamics and function in cells (Verhey and Gaertig, 2007; Janke, 2014). Recent advances in molecular biology have enabled the purification of recombinant tubulin heterodimers (discussed in chapters 2 and 3), which opens the door to dissect how variations in this code control microtubule assembly *in vitro*. However, we still do not know how specific sequence alterations impact microtubule dynamics or interactions with MAPs in cells.

What is the sequence-structure-function relationship for each isotype? In chapter 2, I show that that two neuronally expressed β tubulin isotypes have distinct polymerization dynamics. Studies in mice have revealed the non-interchangeability of β tubulin isotypes (Saillour et al., 2014). Briefly, knockout of the β tubulin βIII leads to defects in cortical development that cannot be fully rescued by expression of βIIB and other isotypes. What property of βIII is required for proper cortical development? In chapter 2, I generate chimeric β tubulins that have the C-terminal tails swapped and show that microtubules assembled with these chimeric tubulins exhibit polymerization properties similar to the wild-type construct with the identical 'core'. With this information in hand, experiments could be designed whereby different chimeric constructs could be expressed in place of specific tubulin isotypes. For example, Crispr/Cas9-mediated gene editing could be used to replace βIII with the chimera with the βIII core/βIIB tail or the chimera with the βIII tail/ βIIB core could help resolve which part of the protein is more important for βIII function.

The phenotype of tubulin isotype knockdown can manifest in two ways. First, it can impact the total tubulin level in the cell. Each α tubulin associates with a single β tubulin to form a stable dimer, so the total amount of the less abundant subunit determines the number of heterodimers that can form. In support of this, mutations in human β tubulins have been identified that reduce the capacity of heterodimers to polymerize into microtubules (Tischfield et al., 2010). This could impact the effective concentration of free tubulin that can assemble into filaments. Similarly, tubulin overexpression is not tolerated in many cell types, suggesting that the total tubulin concentration in cells is resistant to perturbation. Second, the loss of a specific tubulin isotype could impact the ratio of tubulin isotypes in the cell. In chapter 2, I show that by varying the ratio of βIIB to βIII tubulin, the polymerization properties of these mixed microtubules can be tuned. However, we don't know whether similar modifications of the ratio of tubulin isotypes can manifest changes in polymerization dynamics in cells.

Currently, we do not know how tubulin isotypes are spatially regulated in cells and whether microtubules with distinct isotype composition can form within the same cell. Previous studies have shown that different tubulin isotypes can indiscriminately assemble into interphase and spindle microtubules (Lewis et al., 1987). However, these studies were limited to HeLa cells, which do not normally express all tubulin isotypes. For example, βII and βIII are normally expressed in post-mitotic neurons, but their sub-cellular localization in these cells has not been examined. Furthermore, the observation that two isotypes can co-polymerize does not necessarily mean that all microtubules in a cell that expresses those isotypes would be composed of the same mixture of tubulins. For example, work using antibodies specific to de-tyrosinated α-tubulin has shown that two populations of

microtubules (tyrosinated and de-tyrosinated) co-exist within higher ordered arrays during interphase and mitosis (Gundersen and Bulinski, 1986). Detyrosination protects microtubules from kinesin-13-mediated depolymerization, providing a possible explanation for how these filaments are stabilized in cells (Peris et al., 2009; Sirajuddin et al., 2014). A recent study from our lab has shown that microtubules assembled from βIIB are more resistant to MCAK and chTOG-mediated depolymerization than those assembled from βIII, suggesting that such a mechanism may also act to stabilize microtubules enriched in this isotype in cells (Ti et al., 2018). Examination of fixed cells such as neurons by immunofluorescence using antibodies that can discriminate between different tubulin isotypes will help resolve these questions.

Structural studies of cells from various organisms has revealed the plethora of microtubule arrays that can form (Chaaban et al., 2017). Textbooks portray a canonical 9+2 array of microtubules in the axoneme, but the organization of microtubules in many organisms have diverged substantially. For example, in the sperm of the matidfly *M. perla*, microtubules assemble with 40 protofilaments (Chaaban et al., 2017). What are the rules that specify such noncanonical microtubule assembly? These microtubule structures are likely guided by interactions with various MAPs expressed in the tissue. Exactly how MAPs specify the architecture and organization of such structures remains unexplored.

5.3. Open questions in midzone assembly and function

In chapter 4, I combine live cell imaging with protein knockdown to investigate the contribution of the vertebrate spindle midzone to chromosome movement in anaphase. Using lattice light sheet microscopy, I show that the cross-sectional organization of PRC1-tagged microtubule bundles in the midzone appears similar in early and late anaphase. Specifically, the nearest-neighbor distance between PRC1 spots remains constant even as the spindle elongates up to 50% of its metaphase length. This is observed despite apparent fusion events between bundles. What drives these fusion events, and how is the average nearest-neighbor distance established? One way to probe this process is to inhibit late mitotic events such as cytokinesis and examine how the organization of microtubule bundles responds. We can do this using chemical inhibitors such as Latrunculin to inhibit the polymerization of actin filaments, thereby inhibiting furrow ingression.

I use shRNA-mediated protein knockdown to reduce PRC1 expression in two human cell lines (HeLa and hTERT-RPE1). The results from both cell lines were similar: chromosomes segregate faster and further in cells following PRC1 knockdown, revealing that in vertebrates, the midzone acts as a brake to restrict chromosome movement. What is the consequence of these altered chromosome dynamics? We did not observe an increase in lagging chromosome frequency, suggesting that the fidelity of chromosome segregation is preserved. However, differences could manifest more clearly in the context of perturbed chromosome segregation. For example, a recent study has shown that the presence of microtubule bundles negatively regulates nuclear envelope reformation (NER) (Liu et al., 2018). Consequently, lagging chromosomes that are positioned closer to the midzone following NER initiation are defective in NER. This effect can be reversed by treatment

with nocodazole to disassemble microtubules in early anaphase. PRC1 knockdown decreases the density of microtubules in the midzone, suggesting that the total polymer level is decreased. This could therefore impact the kinetics of NER, although this has not been explored.

Following shRNA-mediated PRC1 knockdown, I express PRC1 constructs that are shRNA-resistant and see distinct phenotypes. Full-length GFP-tagged PRC1 rescues the defect in chromosome segregation speed and distance. Expression of a mutant PRC1 construct ($PRC1^{AA}$) that has reduced binding affinity to microtubules shows a phenotype intermediate between that observed in knockdown and control cells. In $PRC1^{AA}$ cells, microtubule bundle assembly is restored, but the chromosome hyper-segregation defect associated with PRC1 knockdown persists. This could be a consequence of two activities. First, chromosome hyper-segregation could result from an increased *rate* of chromosome segregation, similar to what we observed in knockdown alone. Second, it could result from a prolonged *period* of chromosome segregation. To resolve this question, examination of chromosome segregation rates in live cells is therefore a top priority.

Cells expressing mutant $PRC1^{AA}$ assemble microtubule bundles that do not decrease in length during anaphase. This could be a consequence of two activities. First, microtubule sliding between filaments in these bundles could be inhibited. Second, if plus-end dynamics of filaments in bundles are not suppressed, filaments would continue to grow and sliding could proceed without a corresponding decrease in overlap length. The use of a photoactivatable tubulin would be a good tool to probe this question. Using this construct, we could selectively photoactivate tubulin in microtubule bundles between a pair of segregating chromosomes in early anaphase and examine the fluorescent “spot”. If

microtubule sliding occurs, then the spot should separate into two spots as filaments are slid apart, as has been shown previously (Vukušić et al., 2017). Resolving this question will be important next step.

In cells, I also examined a second PRC1 mutant construct ($PRC1^{\Delta C}$) that has a similarly reduced binding affinity compared to the mutant mentioned above. However, cells expressing this construct do not form midzone microtubule bundles and look morphologically similar to knockdown alone. Why this discrepancy? The construct lacks the unstructured C-terminal tail of PRC1 but is capable of cross-linking microtubules (Subramanian et al., 2010). The C-terminal tail of PRC1 mediates interactions with a subset of binding partners including the kinase Plk1 (Neef et al., 2007) and contains multiple Cdk1 consensus sites whose phosphorylation state is thought to regulate PRC1 activity (Jiang et al., 1998; Zhu et al., 2006). The impact on midzone assembly due to reduced microtubule binding affinity may therefore be compounded by effects associated with disrupted protein recruitment to the midzone. For example, the *C. elegans* PRC1 homolog was originally isolated in a screen for temperature-sensitive cell division defects and it was later shown that the allele, Oj5, harbors a mutation in the centralspindlin binding domain, which is in a different region than the microtubule binding domain (O'Connell et al., 1998; Verbrugghe and White, 2004). In the first division of the *C. elegans* embryo, the direct interaction between PRC1 and centralspindlin is thought to reinforce mechanical resilience of the central spindle and prevent the two half-spindles from breaking apart, a phenotype associated with PRC1 knockdown in many organisms (Lee et al., 2015). Therefore, to fully characterize the impact of mutant PRC1 expression in cells, it will be important to

determine the localization of other key midzone-associated proteins, for example centralspindlin, Aurora B or Kif4.

Materials and Methods

Purification of recombinant human tubulin

The cDNA encoding *Homo sapiens* α tubulin 1B (NP_006073.2) and β tubulin 2B (BC001352) or β tubulin 3 (NP_006077.2) were cloned into pFastBac Dual vector (Life Technologies). For affinity purification, a sequence encoding a Tobacco Etch Virus (TEV) protease site and hexa-histidine tag was fused to the 3' end of the β tubulin isotype 2B or β tubulin isotype 3 cDNA sequence. We used the Bac-to-Bac system (Life Technologies) to generate recombinant baculovirus. High Five cells (Life Technologies), grown to 3.0-3.5x10^6 cells/ml in Sf-900 II SFM (Life Technologies 10902-096) supplemented with 1X Antibiotic-Antimyocotic (Life Technologies 15240-062), were infected with P3 viral stocks at a multiplicity of infection (MOI) of 50. Cells were cultured in suspension at 27 ºC and harvested at 60 hours after infection. The following steps were performed on ice or at 4 ºC. We lysed cells in an equal volume of lysis buffer (50 mM HEPES, 20 mM Imidazole, 100 mM KCl, 1 mM $MgCl_2$, 0.5 mM DTT, 0.1 mM GTP, 3 U/ml benzonase, 1X protease inhibitor Roche Complete EDTA-free, pH 7.2) by dounce homogenizer (20 strokes) and centrifuged the homogenate at 55,000 rpm in a Ti70 rotor (Beckman Coulter) for 1 hour. The supernatant was then filtered through a 0.22 μm Millex-GP PES membrane (Millipore SLGP033RS) and loaded at 0.8 ml/min onto a 1 ml HisTrap HP column (GE life science 17-5247-01) pre-equilibrated with lysis buffer. The column was washed with 25 ml lysis buffer and then eluted with nickel elution buffer (1X BRB80 (80 mM PIPES, 1mM $MgCl_2$, 1mM EGTA), 500 mM imidazole, 0.1 mM GTP, 1 mM DTT, pH 6.8). The fractions containing proteins were pooled, diluted 10-fold with TOG-column buffer (1X BRB80, 1 mM DTT, 0.2 mM GTP, pH 6.8), mixed with 6 mg TEV protease and incubated

for 1 hour on ice. The TEV-digested protein solution was loaded at 1 ml/min onto tandem chromatography columns consisting of a 1 ml HiTrap SP Sepharose FF column (GE life science 17-5054-01) and a 1 ml TOG-affinity column (Widlund et al., 2012) and washed with 10 ml TOG column buffer. We removed the 1 ml HiTrap SP Sepharose FF column and washed the 1 ml TOG-affinity column with 20 ml of wash buffer 1 (1X BRB80 1 mM DTT, 0.1 mM GTP, 10 mM $MgCl_2$, 5 mM ATP, pH 6.8), 20 ml of wash buffer 2 (1X BRB80, 1 mM DTT, 0.1 mM GTP, 0.1 % Tween-20, 10% glycerol, pH 6.8) and 10 ml of TOG column buffer. The tubulin was eluted with TOG elution buffer (1X BRB80, 500 mM $(NH_4)_2SO_4$, 1 mM DTT, 0.2 mM GTP, pH 6.8). The eluate containing tubulin was pooled, quickly exchanged into storage buffer (1X BRB80, 5% glycerol, 1 mM DTT, 0.2 mM GTP, pH 6.8), and concentrated to at least 3 mg/ml with an Amicon Ultra 50K MWCO centrifugal filter (Millipore UFC901024). A typical preparation yielded 1.5 mg of protein from one liter of cultured insect cells, an amount sufficient for biochemical analyses and studies of polymerization dynamics. The purified tubulin was snap frozen with liquid nitrogen and stored at -80 ºC.

Mass spectrometry analysis

Mass spectrometry was performed essentially as described previously (Li et al., 2012). Dried protein samples were resuspended in LDS sample buffer (Life Technologies), reduced and alkylated, and separated on a 4–12% Bis-Tris gradient gel (Life Technologies), followed by in-gel trypsin digestion. Tryptic peptides were purified and analyzed on an LTQ-Orbitrap XL mass spectrometer (Thermo Scientific). To quantify the relative amounts of human and insect alpha tubulin in the final protein, we compared the

signal intensities for each pair of peptides that differ by one amino acid and took the average for all of the peptide pairs (indicating approximately equimolar amounts of human and insect alpha tubulin. To examine the possibility of insect beta tubulin co-purifying in our final protein, we used a similar approach. Insect beta tubulin was detected at low abundance, indicating that it is not a major contaminant of our final recombinant protein. We estimate this fraction of insect tubulin to constitute ~4% of the total beta tubulin.

Microtubule sedimentation assay in the presence of allocolchicine

Allocolchicine was synthesized by following the established method (Fernholz, 1950). Purified tubulin was pre-clarified by high-speed centrifugation in a TLA120.1 rotor (Beckman Coulter) at 90,000 rpm for 10 minutes at 4 °C. Solutions of pre-clarified tubulin (13 □M) were prepared in assay buffer (1X BRB80, 33.33% (v/v) glycerol, 1 mM GTP and 1 mM TCEP) containing 3 % DMSO and 60 μM allocolchicine or 3 % DMSO alone. The reactions were incubated at room temperature for 30 minutes, followed by another 30-minute incubation at 37 °C, and then subjected to high-speed centrifugation in a TLA 120.1 rotor (Beckman Coulter) at 90,000 rpm for 10 minutes at 30 °C. The supernatant was removed and saved for SDS-PAGE analysis. The pellet was rinsed with 40 μl warm wash buffer (1X BRB80, 60% (v/v) glycerol and 1 mM TCEP), and then resuspended in 1X Laemmli sample buffer for SDS-PAGE analysis.

The binding of allocolchicine to tubulin

Purified tubulin was pre-clarified by high-speed centrifugation in a TLA120.1 rotor (Beckman Coulter) at 90,000 rpm for 10 minutes at 4°C. Pre-clarified tubulin (3 μM) was

mixed with increasing concentrations of allocolchicine (0, 1.3, 2.6, 3.9, 5.2, 7.8, 15.6, 31.2 or 62.4 μM) in assay buffer (1X BRB80, 5% (v/v) glycerol, 1 mM GTP and 1 mM TCEP). After 2 hours of incubation at room temperature, the emission spectra of the reactions were collected from 360 nm to 420 nm with 5 nm increments using excitation at 310 nm. The measured fluorescence intensity at 400 nm was plotted on the vertical axis versus allocolchicine concentration on the horizontal axis. To determine the affinity of tubulin for allocolchicine, the unnormalized equilibrium binding curves were fitted with the following equation:

$$\text{Fluorescence intensity at 400 nm}$$

$$= \frac{(K_d + [\text{Allo}] + [\text{Tubulin}]) - \sqrt{(K_d + [Allo] + [\text{Tubulin}])^2 - 4 \times [\text{Allo}] \times [\text{Tubulin}]}}{2 \times [\text{Tubulin}]}$$

$$\times (F_{max} - F_{Background}) + F_{Background}$$

Where K_d represents the dissociation constant for allocolchicine binding, F_{max} represents the fluorescence intensity at plateau, and $F_{background}$ represents the background fluorescence intensity.

***In vitro* fluorescence microscopy**

All experiments were performed on a Nikon Eclipse Ti microscope equipped with a NA-1.49 100X Plan Apo TIRF objective (Nikon). The microscope setup included a 3-axis piezo-electric stage (Mad City LabsNano LP-200), an EM-CCD camera (Andor iXon DU-897), and two-color TIRF imaging optics (lasers: 488 nm (Spectra-physics) and 561 nm (Cobalt); Filters: Emission (Semrock FF01-520/35 and FF01-609/54), Dichroic

(Semrock Di01-R488/561)). Sample chambers were prepared by first cleaning 18x18 mm glass coverslips (Gold Seal Cover Glass, thickness No.1) and 27x46 mm slides (Buehler 40-80000-01). To prevent nonspecific surface sticking, we then coated the surface of slides with nonbiotinylated PEG and the surface of coverslips with a mixture of biotinylated PEG and nonbiotinylated PEG following standard protocols. To build flow chambers, we apply two strips of double-sided tape to a microscope slide and apply the coverslip. Sample chamber volumes were approximately 6-8 μL.

To generate seeds for templated microtubule growth, we polymerized the recombinant tubulins at 12 μM concentration along with 8 mol% Alexa-488 and biotin labeled bovine tubulin in the presence of 2.5 mM GMPCPP. The polymerized GMPCPP 'seeds' were immobilized on a coverslip by first coating the surface with NeutrAvidin. After a 5 min incubation with κ-casein to block nonspecific binding to the surface, a mixture of recombinant tubulin and 4 mol% X-rhodamine labeled bovine tubulin was flowed into the TIRF chamber maintained at 30 ºC. Time-lapse images were acquired at a rate of 1 frame every 10 seconds for 15 minutes. All assays with dynamic microtubules were done in buffer containing 1X BRB80, 1 mM GTP, 4% glycerol, 0.2 mg/ml κ-casein, 0.2% methylcellulose, and oxygen scavenging mix (25 mM glucose, 40 mg/ml glucose oxidase, 35 mg/ml catalase and 0.5% β-mercaptoethanol final concentration in reaction).

To test MAPs binding, recombinant human tubulin was mixed with 8 mol% X-rhodamine and biotinylated tubulin and polymerized in the presence of 10 μM Taxol. We prepared the TIRF imaging chamber and immobilized the Taxol-stabilized microtubules as described above. Assays were done in buffer containing 1X BRB80, 5% sucrose, 1 mM $MgCl_2$, 1 mM TCEP, 10 μM Taxol, 0.25 mg/mL κ-casein, oxygen scavenging mix. 2 mM

Mg-ATP was added in the buffer for motor MAPs, and 80 mM KCl was added in the buffer for kinesin-5-GFP. Experiments using the non-motor MAPs (16 nM GFP-PRC1-SC or 20 nM NuMA tail-II-GFP) were incubated on microtubules for 5 min before imaging. Experiments using the motor MAPs (0.7 nM kinesin-1ΔC-GFP or 0.6 nM kinesin-5-GFP) were imaged immediately after flowing the reaction mixture into the chamber. Time-lapse images were acquired at a rate of 1 frame/5 sec for 25 sec. All MAPs binding experiments were carried out at room temperature.

Image analysis was performed by creating kymographs from the time lapse TIRF images of microtubules using ImageJ. The data were quantified by measuring the slope of the growing microtubule extension and using this to determine the average growth speed for each filament. The mean polymerization rate was calculated from all microtubules analyzed for each condition. The mean and standard deviation are reported in the figures. To determine catastrophe frequency, we divided the total number of catastrophe events for all filaments by the total polymerization time (the sum of the amount of time that each filament was observed with a microtubule extension growing off of a visible GMPCPP seed). The standard deviation was estimated as the catastrophe frequency divided by the square root of the number of catastrophe events. This assumes that catastrophe events are Poisson processes.

Estimating the average length of microtubules

We used a model that described the probability of finding a microtubule of a given length at any time, and assumes the four dynamic instability parameters: v_g (velocity of growth), v_s (velocity of shrinkage), f_{cat} (frequency of catastrophe), f_{res} (frequency of rescue) (Verde et al., 1992).

The length probability distribution can be described as:

$$\mathrm{p(x)} = \frac{1}{\mathrm{L}} \times e^{-\frac{x}{L}}$$

Where *L* is the characteristic length.

From their derivations, *L* is given by:

$$\mathrm{L} = \frac{v_s v_g}{(v_s f_{cat}) - (v_g f_{res})}$$

We make the simplifying assumption that $f_{res} = 0$; as we rarely observe rescue events. This simplifies to:

$$\mathrm{L} = \frac{v_s v_g}{v_s f_{cat}} = \frac{v_g}{f_{cat}}$$

At 10.5 μM tubulin concentration, the growth rates of α/βIIB microtubules and α/βIII microtubules are approximately equal and the catastrophe frequencies are such that:

$$f_{cat\_\alpha/\beta\mathrm{IIB}} = \frac{1}{3} f_{cat\_\alpha/\beta\mathrm{III}}$$

This implies that the length of α/βIIB microtubules would be approximately 3-fold greater than that of α/βIII microtubules.

At 10.5 μM tubulin concentration, the measured differences in growth rate and catastrophe frequency for microtubules assembled from mutant βIII tubulin are:

$$v_{g(\beta III-D417H)} = 1.7 \times v_{g(\beta III)}$$

$$f_{cat(\beta III)} = 4 \times f_{cat(\beta III-D417H)}$$

$$f_{cat(\beta III)} = 3 \times f_{cat(\beta III-R262H)}$$

This implies that:

$$L_{\beta III-D417H} \sim = 7 \times L_{\beta III} \text{ and } L_{\beta III-D417H} \sim = 3 \times L_{\beta III}$$

Estimating the fraction of microtubule-bound MAPs *in vivo*

In cells, the concentration of tubulin is ~10 μM and up to 80% can be in the polymerized form. To estimate the fraction of microtubule-bound MAPs in vivo, we used the following simple binding principle that describes the dissociation constant (K_D):

$$K_D = \frac{[MAPs] \times [MT]}{[MAPs\_MT]} = \frac{([MAPs]_0 - [MAPs_{MT}]) \times ([MT]_0 - [MAPs\_MT])}{[MAPs\_MT]}$$

When the number of binding sites on microtubules is much larger than the [MAPs], we make the simplifying assumption that $[MT]_0$ - [MAPs_MT] = $[MT]_0$. The equation is then simplified to:

$$K_D = \frac{([MAPs]_0 - [MAPs_{MT}]) \times [MT]_0}{[MAPs\_MT]}, \quad \frac{K_D}{[MT]_0} = \frac{[MAPs]_0}{[MAPs\_MT]} - 1,$$

$$\text{Fraction of microtubule-bound MAPs} = \frac{[MAPs\_MT]}{[MAPs]_0} = \frac{[MT]_0}{K_D + [MT]_0}$$

When $[MT]_0$ is 10 mM, and the K_D of MAPs for wild-type microtubule is 0.1 μM and for mutant microtubule is 0.5 μM, the fraction of microtubule-bound MAPs on wild-type and mutant filaments is 0.99 and 0.95, respectively.

Purification of MAPs

We purified GST-tagged TOG1/2 and GFP-tagged recombinant kinesin-1ΔC, kinesin-5, PRC1-SC and NuMA tail II according to published protocols (Friedman and Vale, 1999; Weinger et al., 2011; Widlund et al., 2012; Subramanian et al., 2013; Forth et al., 2014).

Cell lines used for LLSM imaging

Stable hTERT-RPE1 cells expressing GFP-PRC1 were generated by retroviral transduction as described previously (Subramanian Cell 2013).

Stable HeLa Trex Flp-in cells expressing N-terminally tagged Halo-PRC1 were generated following standard Invitrogen protocol. The HaloTag sequence (Promega) was introduced at the N-terminus of human PRC1 isoform II coding sequence. The construct was cloned into the pCDNA5/FRO/TO (Invitrogen) expression plasmid. Expression of Halo-PRC1 was induced by adding 2 ug/ml tetracycline into the media 48 hrs before imaging.

Cell lines used for PRC1 knockdown and confocal imaging

To allow for tetracycline-inducible expression of the shRNA construct in hTERT-RPE1 cells, we first cloned the TetR sequence into the pMSCVblast expression vector. We

generated cells constitutively expressing the tet repressor protein via retroviral transduction. The plasmid was first transfected into Ampho-293 cells for retrovirus production. The media was then harvested and added directly to hTERT-RPE1 cells in the presence of 4 ug/ml polybrene after filtering through a 0.45 um filter. Blasticidin (XXX company) was used to select for cells that had stably incorporated the construct into the genomic DNA.

We selected the shRNA target sequence in PRC1 (5' - GTGATTGAGGC**A**AT**T**CG**A**G - 3') which had been previously shown to suppress PRC1 in cells (Voets et al. 2015). We generated double stranded oligomers encoding sense and antisense target sequence separated by a 9-bp hairpin sequence. The oligomers were cloned into the pSuperior.retro.puro (Oligoengine) backbone between the BglII and HindIII restriction sites. To generate HeLa and RPE1 cells with tetracycline-inducible control of PRC1 shRNA expression, we introduced the shRNA construct by retroviral transduction into the appropriate cell lines as described above. Puromycin (Sigma) was used to to select for cells that had stably incorporated the construct into the genomic DNA. To induce shRNA expression, 2 um/ml tetracycline was added 72 hrs before imaging. The media was replaced with fresh tetracycline once 24 hrs before imaging.

We generated an shRNA-resistant PRC1 construct by introducing three silent mutations into the coding sequence for human PRC1 isoform II (REF #XX) (A888C, T891A, and A894G, noted as bold letters in the target sequence above). We introduced a GFP tag at the N-terminus of PRC1 coding sequence and cloned this construct into the pCDNA5/FRT expression plasmid (Invitrogen). To generate HeLa cells constitutively expressing shRNA-resistant GFP-PRC1, we transfected the construct into HeLa T-Rex

Flp-in cells that had already stably incorporated the PRC1 shRNA construct following standard Invitrogen protocol. Hygromycin B (Invitrogen) was used to select for cells that had stably incorporated the construct into the engineered Flp-in site.

Tissue culture

HeLa T-Rex Flp-in cells were cultured in DMEM (Gibco) media supplemented with 10% fetal bovine serum (Sigma) and 2 mM L-Glutamine (Gibco) and incubated in 5% CO_2 at 37°C. hTERT-RPE1 cells were cultured in DMEM/F-12 GlutaMAX (Gibco) media supplemented with 10% fetal bovine serum (Sigma) and incubated in 5% CO_2 at 37°C.

Immunological methods

Cells were grown on 12 mm diameter glass coverslips for 2 days prior to fixation. Cells were fixed in a buffer containing formaldehyde (100 mM PIPES, 1 mM MgCl2, 10 mM EGTA, 0.2% Triton-X, 4% Formaldehyde, pH 6.8) prewarmed to 37°C for 20 mins. Cells were blocked in 1X PHEM + 2% BSA (60 mM K-pipes, 25 mM HEPES, 10 mM EGTA, 4 mM MgSO4, 2% bovine serum albumin, pH 6.9) for 2 hrs at room temperature or overnight at 4°C. Coverslips were then incubated with anti-PRC1 antibody (raised against PRC1 (aa 341-466) in rabbit, affinity purified and used at 0.5 ug/ml) overnight at 4°C. After 3 washes with 1XPHEM for 5 mins at room temperature, the coverslips were incubated for 2 hrs at room temperature with FITC-conjugated mouse anti-tubulin monoclonal antibody (Sigma # F2168; 1:1000 dilution). After 3 washes, coverslips were incubated in donkey anti-rabbit Texas red conjugated secondary antibody (Jackson

Immunoresearch; 1:1000 dilution) in 1X PHEM + 6% donkey serum. After 3 washes, DNA was stained with 1 um/ml DAPI for 10 mins at room temperature, mounted (20 mM Tris pH 8, 0.5% propyl gallate, 90% glycerol) and sealed with nail polish.

For Western blot analysis, the anti-PRC1 antibody was used at 0.5 mg/ml and monoclonal anti-alpha tubulin antibody was used at 1:1000 dilution (Sigma #T6199). Dye-conjugated secondary antibodies raised in donkey were purchased from LI-COR.

Fixed cell analysis

Images of fixed cells were acquired as z stacks with 0.2 mm spacing using a 100x, 1.35NA objective on a DeltaVision Image Restoration Microscope (Applied Precision Instruments and Olympus). The immunofluorescence micrographs were processed by iterative constrained deconvolution (SoftWoRx, Applied Precision Instruments). Maximum-intensity projections were converted to tiff files and linescans were generated using Fiji software (Schindelin et al., 2012).

Live cell imaging using lattice light sheet microscopy

Cells were cultured on 5-mm diameter coverslips (Warner Instruments, 64-0700). hTERT-RPE1 cells expressing GFP-PRC1 were incubated in 500 nM SiR-DNA in standard culture media for 30-60 minutes prior to imaging. HeLa TRex Flp-in cells expressing Images were collected on a custom-built instrument. Cells were imaged in Leibovitz's L-15 media (Gibco) supplemented with 10% fetal bovine serum (Sigma) and 2 mM L-glutamine (Gibco) at 37°C. Dividing cells were selected and the exposure time for each channel was adjusted to optimize the signal-to-noise ratio and ranged from 10-40

ms. Cells were excited sequentially using a 488 nm laser to visualize GFP-PRC1 and a 642 nm laser to visualize chromosomes. Three-dimensional stacks consisting of 101 optical sections spaced 400 nm apart were captured in each channel. The cells were imaged at a rate of up to 20 cell volumes/min.

Live cell imaging using spinning disk confocal

Cells were cultured on 22-mm square coverslips and mounted in a custom Rose chamber or grown on 35 mm glass-bottomed plates. Cells were imaged in Leibovitz's L-15 media (Gibco) supplemented with 10% fetal bovine serum (Sigma) and 2 mM L-glutamine (Gibco) at 35-37°C.

Confocal GFP fluorescence micrographs of hTERT-RPE1 cells expressing GFP-Centrin/GFP-CENP-A were acquired using a Nikon TE2000 microscope (Morrell Instruments) with a 100x oil objective (PlanApo, 1.4 NA) equipped with a z piezo stage. 0.4 um spacing between z planes were taken through the entire cell with a PerkinElmer Wallac UltraView confocal head, 488 nm excitation laser (Coherent). Images were acquired with an sCMOS Prime95B camera (Photometrics) using NIS-Elements software (Nikon).

Confocal fluorescence and DIC micrographs were acquired using an Inverted Zeiss Axiovert 200 microscope (Zeiss/Perkin-Elmer) with a 100x oil objective (PlanApo, 1.4 NA). Images consisting of single z planes were taken with a PerkinElmer Wallac UltraView confocal head using solid-state 491 and/or 644 lasers for excitation (Spectral Applied). Images were acquired with an EMCCD iXon camera (Andor) using Metamorph software (MDS Analytical Technologies).

Fluorescence recovery after photobleaching

FRAP experiments were performed on an inverted Axiovert 200 (Zeiss) equipped with a spinning disk confocal head (UltraView Perkin-Elmer). hTERT-RPE1 cells expressing GFP-PRC1 were excited with a 491 nm solid state laser (Spectral applied) and imaged with an NA 1.49 oil immersion 100X objective lens. Fluorescence was detected onto an EMCCD camera (iXon Andor). The regions of interest covering bleached areas were defined with a micromirror array system (Mosaic ® digital diaphragm system Photonics, Inc.). Bleaching was performed with a 2 - 3 s pulse and recovered fluorescence was collected every 3 s with a 200 - 300 ms exposure time. Fluorescence recovery, R(t), was normalized and fit to the following equation to determine the recovery constant, k : $R(t) = A*(1-\exp(-k*t))$, where A is a constant. All acquisition parameters were controlled with MetaMorph software.

Data Analysis on LLSM images

After image acquisition, several processing steps were necessary before quantitative analyses could be performed. First, due to the geometry of the excitation/emission objective pair, the raw image data was deskewed in order to obtain image stacks in the reference frame of the cell. Data were then deconvolved using a Richardson-Lucy algorithm and the system's point-spread function, measured in independent experiments using 100 nm diameter fluorescent beads. We next compensated for spindle rotation and translation within the imaging window by applying a rigid transform using MATLAB's imregtform function. This transform was defined and applied between subsequent frames in the PRC1 channel and then applied to each DNA-channel

frame. We then translated and rotated the data such that the long axis of the spindle was aligned to the X axis and centered in the image window. To describe the geometry of single microtubule bundles, LLSM data sets were first denoised using third-party bandpass function in MATLAB. Next, a watershed routine was applied to segment individual bundles and object geometry was extracted using MATLAB's regionprops3 function.

References

Aist, J.R., and Berns, M.W. (1981). Mechanics of chromosome separation during mitosis in Fusarium (Fungi imperfecti): new evidence from ultrastructural and laser microbeam experiments. J. Cell Biol. *91*, 446–458.

Aist, J.R., Bayles, C.J., Taof, W., and Berns, M.W. (1991). Direct experimental evidence for the existence, structural basis and function of astral forces during anaphase B in vivo. 10.

Akhmanova, A., and Steinmetz, M.O. (2008). Tracking the ends: a dynamic protein network controls the fate of microtubule tips. Nat. Rev. Mol. Cell Biol. *9*, 309–322.

Akhmanova, A., and Steinmetz, M.O. (2010). Microtubule +TIPs at a glance. J Cell Sci *123*, 3415–3419.

Akhmanova, A., and Steinmetz, M.O. (2015). Control of microtubule organization and dynamics: two ends in the limelight. Nat. Rev. Mol. Cell Biol. *16*, 711–726.

Al-Bassam, J., Breugel, M. van, Harrison, S.C., and Hyman, A. (2006). Stu2p binds tubulin and undergoes an open-to-closed conformational change. J Cell Biol *172*, 1009–1022.

Allen, C., and Borisy, G.G. (1974). Structural polarity and directional growth of microtubules of Chlamydomonas flagella. J. Mol. Biol. *90*, 381–402.

Alushin, G.M., Lander, G.C., Kellogg, E.H., Zhang, R., Baker, D., and Nogales, E. (2014). High-Resolution Microtubule Structures Reveal the Structural Transitions in αβ-Tubulin upon GTP Hydrolysis. Cell *157*, 1117–1129.

Arnal, I., Metoz, F., DeBonis, S., and Wade, R.H. (1996). Three-dimensional structure of functional motor proteins on microtubules. Curr. Biol. *6*, 1265–1270.

Asbury, C.L. (2017). Anaphase A: Disassembling Microtubules Move Chromosomes toward Spindle Poles. Biology *6*.

Aumeier, C., Schaedel, L., Gaillard, J., John, K., Blanchoin, L., and Théry, M. (2016). Self-repair promotes microtubule rescue. Nat. Cell Biol. *18*, 1054–1064.

Ayaz, P., Ye, X., Huddleston, P., Brautigam, C.A., and Rice, L.M. (2012). A TOG:αβ-tubulin Complex Structure Reveals Conformation-Based Mechanisms For a Microtubule Polymerase. Science *337*, 857–860.

Banerjee, A., Roach, M.C., Wall, K.A., Lopata, M.A., Cleveland, D.W., and Ludueña, R.F. (1988). A monoclonal antibody against the type II isotype of beta-tubulin. Preparation of isotypically altered tubulin. J. Biol. Chem. *263*, 3029–3034.

Banerjee, A., Roach, M.C., Trcka, P., and Ludueña, R.F. (1992). Preparation of a monoclonal antibody specific for the class IV isotype of beta-tubulin. Purification and assembly of alpha beta II, alpha beta III, and alpha beta IV tubulin dimers from bovine brain. J. Biol. Chem. *267*, 5625–5630.

Bieling, P., Telley, I.A., and Surrey, T. (2010). A Minimal Midzone Protein Module Controls Formation and Length of Antiparallel Microtubule Overlaps. Cell *142*, 420–432.

Bowne-Anderson, H., Zanic, M., Kauer, M., and Howard, J. (2013). Microtubule dynamic instability: A new model with coupled GTP hydrolysis and multistep catastrophe. BioEssays *35*, 452–461.

Braun, M., Lansky, Z., Fink, G., Ruhnow, F., Diez, S., and Janson, M.E. (2011). Adaptive braking by Ase1 prevents overlapping microtubules from sliding completely apart. Nat. Cell Biol. *13*, 1259–1264.

Bringmann, H., Skiniotis, G., Spilker, A., Kandels-Lewis, S., Vernos, I., and Surrey, T. (2004). A Kinesin-like Motor Inhibits Microtubule Dynamic Instability. Science *303*, 1519–1522.

Brinkley, B.R., and Cartwright, J. (1971). ULTRASTRUCTURAL ANALYSIS OF MITOTIC SPINDLE ELONGATION IN MAMMALIAN CELLS IN VITRO: Direct Microtubule Counts. J. Cell Biol. *50*, 416–431.

Cande, W.Z. (1982). Nucleotide requirements for anaphase chromosome movements in permeabilized mitotic cells: Anaphase B but not anaphase a requires ATP. Cell *28*, 15–22.

Cande, W.Z., and McDonald, K. (1986). Physiological and ultrastructural analysis of elongating mitotic spindles reactivated in vitro. J. Cell Biol. *103*, 593–604.

Cande, W.Z., and McDonald, K.L. (1985). In vitro reactivation of anaphase spindle elongation using isolated diatom spindles. Nature *316*, 168–170.

Canman, J.C., Hoffman, D.B., and Salmon, E.. (2000). The role of pre- and post-anaphase microtubules in the cytokinesis phase of the cell cycle. Curr. Biol. *10*, 611–614.

Caplow, M., and Shanks, J. (1990). Mechanism of the microtubule GTPase reaction. J. Biol. Chem. *265*, 8935–8941.

Caplow, M., and Shanks, J. (1996). Evidence that a single monolayer tubulin-GTP cap is both necessary and sufficient to stabilize microtubules. Mol. Biol. Cell *7*, 663–675.

Caplow, M., Ruhlen, R.L., and Shanks, J. (1994). The free energy for hydrolysis of a microtubule-bound nucleotide triphosphate is near zero: all of the free energy for hydrolysis is stored in the microtubule lattice. J. Cell Biol. *127*, 779–788.

Cassimeris, L., Pryer, N.K., and Salmon, E.D. (1988). Real-time observations of microtubule dynamic instability in living cells. J. Cell Biol. *107*, 2223–2231.

Chaaban, S., Brouhard, G.J., and Bement, W. (2017). A microtubule bestiary: structural diversity in tubulin polymers. Mol. Biol. Cell *28*, 2924–2931.

Chaaban, S., Jariwala, S., Hsu, C.-T., Redemann, S., Kollman, J.M., Müller-Reichert, T., Sept, D., Bui, K.H., and Brouhard, G.J. (2018). The Structure and Dynamics of C. elegans Tubulin Reveals the Mechanistic Basis of Microtubule Growth. Dev. Cell.

Chang-Jie, J., and Sonobe, S. (1993). Identification and preliminary characterization of a 65 kDa higher-plant microtubule-associated protein. 11.

Chen, B.-C., Legant, W.R., Wang, K., Shao, L., Milkie, D.E., Davidson, M.W., Janetopoulos, C., Wu, X.S., Hammer, J.A., Liu, Z., et al. (2014). Lattice light-sheet microscopy: Imaging molecules to embryos at high spatiotemporal resolution. Science *346*, 1257998.

Chrétien, D., and Wade, R.H. (1991). New data on the microtubule surface lattice. Biol. Cell *71*, 161–174.

Chrétien, D., Fuller, S.D., and Karsenti, E. (1995). Structure of growing microtubule ends: two-dimensional sheets close into tubes at variable rates. J. Cell Biol. *129*, 1311–1328.

Cole, D.G., Saxton, W.M., Sheehan, K.B., and Scholey, J.M. (1994). A "slow" homotetrameric kinesin-related motor protein purified from Drosophila embryos. J. Biol. Chem. *269*, 22913–22916.

Collins, E., Mann, B.J., and Wadsworth, P. (2014). Eg5 restricts anaphase B spindle elongation in mammalian cells. Cytoskeleton *71*, 136–144.

Coombes, C.E., Yamamoto, A., Kenzie, M.R., Odde, D.J., and Gardner, M.K. (2013). Evolving Tip Structures Can Explain Age-Dependent Microtubule Catastrophe. Curr. Biol. *23*, 1342–1348.

David-Pfeuty, T., Erickson, H.P., and Pantaloni, D. (1977). Guanosinetriphosphatase activity of tubulin associated with microtubule assembly. Proc. Natl. Acad. Sci. *74*, 5372–5376.

Desai, A., and Mitchison, T.J. (1997). Microtubule Polymerization Dynamics. Annu. Rev. Cell Dev. Biol. *13*, 83–117.

Dimitrov, A., Quesnoit, M., Moutel, S., Cantaloube, I., Poüs, C., and Perez, F. (2008). Detection of GTP-Tubulin Conformation in Vivo Reveals a Role for GTP Remnants in Microtubule Rescues. Science *322*, 1353–1356.

Ding, R., McDonald, K.L., and McIntosh, J.R. (1993). Three-dimensional reconstruction and analysis of mitotic spindles from the yeast, Schizosaccharomyces pombe. J. Cell Biol. *120*, 141–151.

Drechsel, D.N., and Kirschner, M.W. (1994). The minimum GTP cap required to stabilize microtubules. Curr. Biol. *4*, 1053–1061.

Drechsler, H., and McAinsh, A.D. (2016). Kinesin-12 motors cooperate to suppress microtubule catastrophes and drive the formation of parallel microtubule bundles. Proc. Natl. Acad. Sci. *113*, E1635–E1644.

Drechsler, H., McHugh, T., Singleton, M.R., Carter, N.J., and McAinsh, A.D. (2014). The Kinesin-12 Kif15 is a processive track-switching tetramer. ELife *3*, e01724.

Elting, M.W., Hueschen, C.L., Udy, D.B., and Dumont, S. (2014). Force on spindle microtubule minus ends moves chromosomes. J Cell Biol *206*, 245–256.

Enos, A.P., and Morris, N.R. (1990). Mutation of a gene that encodes a kinesin-like protein blocks nuclear division in A. nidulans. Cell *60*, 1019–1027.

Euteneuer, U., and McIntosh, J.R. (1980). Polarity of midbody and phragmoplast microtubules. J. Cell Biol. *87*, 509–515.

Euteneuer, U., Jackson, W.T., and McIntosh, J.R. (1982). Polarity of spindle microtubules in Haemanthus endosperm. J. Cell Biol. *94*, 644–653.

Fan, J., Griffiths, A.D., Lockhart, A., Cross, R.A., and Amos, L.A. (1996). Microtubule Minus Ends can be Labelled with a Phage Display Antibody Specific to Alpha-Tubulin. J. Mol. Biol. *259*, 325–330.

Ferenz, N.P., Paul, R., Fagerstrom, C., Mogilner, A., and Wadsworth, P. (2009). Dynein Antagonizes Eg5 by Crosslinking and Sliding Antiparallel Microtubules. Curr. Biol. *19*, 1833–1838.

Ferenz, N.P., Gable, A., and Wadsworth, P. (2010). Mitotic Functions of Kinesin-5. Semin. Cell Dev. Biol. *21*, 255–259.

Fink, G., Schuchardt, I., Colombelli, J., Stelzer, E., and Steinberg, G. (2006). Dynein-mediated pulling forces drive rapid mitotic spindle elongation in Ustilago maydis. EMBO J. *25*, 4897–4908.

Forth, S., Hsia, K.-C., Shimamoto, Y., and Kapoor, T.M. (2014). Asymmetric Friction of Nonmotor MAPs Can Lead to Their Directional Motion in Active Microtubule Networks. Cell *157*, 420–432.

Friedman, D.S., and Vale, R.D. (1999). Single-molecule analysis of kinesin motility reveals regulation by the cargo-binding tail domain. Nat. Cell Biol. *1*, 293–297.

Fu, C., Ward, J.J., Loiodice, I., Velve-Casquillas, G., Nedelec, F.J., and Tran, P.T. (2009). Phospho-Regulated Interaction between Kinesin-6 Klp9p and Microtubule Bundler Ase1p Promotes Spindle Elongation. Dev. Cell *17*, 257–267.

Gaillard, J., Neumann, E., Van Damme, D., Stoppin-Mellet, V., Ebel, C., Barbier, E., Geelen, D., and Vantard, M. (2008). Two Microtubule-associated Proteins of Arabidopsis MAP65s Promote Antiparallel Microtubule Bundling. Mol. Biol. Cell *19*, 4534–4544.

Galjart, N. (2010). Plus-End-Tracking Proteins and Their Interactions at Microtubule Ends. Curr. Biol. *20*, R528–R537.

Gard, D.L., and Kirschner, M.W. (1987). A microtubule-associated protein from Xenopus eggs that specifically promotes assembly at the plus-end. J. Cell Biol. *105*, 2203–2215.

Gardner, M.K., Zanic, M., and Howard, J. (2013). Microtubule catastrophe and rescue. Curr. Opin. Cell Biol. *25*, 14–22.

Gell, C., Friel, C.T., Borgonovo, B., Drechsel, D.N., Hyman, A.A., and Howard, J. (2011). Purification of Tubulin from Porcine Brain. In Microtubule Dynamics: Methods and Protocols, A. Straube, ed. (Totowa, NJ: Humana Press), pp. 15–28.

Geyer, E.A., Burns, A., Lalonde, B.A., Ye, X., Piedra, F.-A., Huffaker, T.C., and Rice, L.M. (2015). A mutation uncouples the tubulin conformational and GTPase cycles, revealing allosteric control of microtubule dynamics. ELife *4*, e10113.

Gigant, B., Curmi, P.A., Martin-Barbey, C., Charbaut, E., Lachkar, S., Lebeau, L., Siavoshian, S., Sobel, A., and Knossow, M. (2000). The 4 Å X-Ray Structure of a Tubulin:Stathmin-like Domain Complex. Cell *102*, 809–816.

Glotzer, M. (2009). The 3Ms of central spindle assembly: microtubules, motors and MAPs. Nat. Rev. Mol. Cell Biol. *10*, 9–20.

Goodwin, S.S., and Vale, R.D. (2010). Patronin Regulates the Microtubule Network by Protecting Microtubule Minus Ends. Cell *143*, 263–274.

Goshima, G., Wollman, R., Goodwin, S.S., Zhang, N., Scholey, J.M., Vale, R.D., and Stuurman, N. (2007). Genes Required for Mitotic Spindle Assembly in Drosophila S2 Cells. Science *316*, 417–421.

Green, R.A., Paluch, E., and Oegema, K. (2012). Cytokinesis in Animal Cells. Annu. Rev. Cell Dev. Biol. *28*, 29–58.

Grill, S.W., Gönczy, P., Stelzer, E.H.K., and Hyman, A.A. (2001). Polarity controls forces governing asymmetric spindle positioning in the *Caenorhabditis elegans* embryo. Nature *409*, 630–633.

Grill, S.W., Howard, J., Schäffer, E., Stelzer, E.H.K., and Hyman, A.A. (2003). The Distribution of Active Force Generators Controls Mitotic Spindle Position. Science *301*, 518–521.

Grimstone, A.V., and Klug, A. (1966). Observations on the Substructure of Flagellar Fibres. J. Cell Sci. *1*, 351–362.

Gruneberg, U., Neef, R., Li, X., Chan, E.H.Y., Chalamalasetty, R.B., Nigg, E.A., and Barr, F.A. (2006). KIF14 and citron kinase act together to promote efficient cytokinesis. J. Cell Biol. *172*, 363–372.

Gundersen, G.G., and Bulinski, J.C. (1986). Distribution of tyrosinated and nontyrosinated alpha-tubulin during mitosis. J. Cell Biol. *102*, 1118–1126.

Hagan, I., and Yanagida, M. (1990). Novel potential mitotic motor protein encoded by the fission yeast cut7+ gene. Nature *347*, 563–566.

Hagan, I., and Yanagida, M. (1992). Kinesin-related cut 7 protein associates with mitotic and meiotic spindles in fission yeast. Nature *356*, 74–76.

Haren, L., and Merdes, A. (2002). Direct binding of NuMA to tubulin is mediated by a novel sequence motif in the tail domain that bundles and stabilizes microtubules. J. Cell Sci. *115*, 1815–1824.

Hastie, S.B. (1989). Spectroscopic and kinetic features of allocolchicine binding to tubulin. Biochemistry *28*, 7753–7760.

Heald, R., and Khodjakov, A. (2015). Thirty years of search and capture: The complex simplicity of mitotic spindle assembly. J Cell Biol *211*, 1103–1111.

Heidemann, S.R., and McIntosh, J.R. (1980). Visualization of the structural polarity of microtubules. Nature *286*, 517–519.

Hendershott, M.C., and Vale, R.D. (2014). Regulation of microtubule minus-end dynamics by CAMSAPs and Patronin. Proc. Natl. Acad. Sci. *111*, 5860–5865.

Hirokawa, N., Noda, Y., Tanaka, Y., and Niwa, S. (2009). Kinesin superfamily motor proteins and intracellular transport. Nat. Rev. Mol. Cell Biol. *10*, 682–696.

Hirose, K., Fan, J., and Amos, L.A. (1995). Re-examination of the Polarity of Microtubules and Sheets Decorated with Kinesin Motor Domain. J. Mol. Biol. *251*, 329–333.

Hogan, C.J., Wein, H., Wordeman, L., Scholey, J.M., Sawin, K.E., and Cande, W.Z. (1993). Inhibition of anaphase spindle elongation in vitro by a peptide antibody that recognizes kinesin motor domain. Proc. Natl. Acad. Sci. *90*, 6611–6615.

Honnappa, S., Cutting, B., Jahnke, W., Seelig, J., and Steinmetz, M.O. (2003). Thermodynamics of the Op18/Stathmin-Tubulin Interaction. J. Biol. Chem. *278*, 38926–38934.

Horio, T., and Hotani, H. (1986). Visualization of the dynamic instability of individual microtubules by dark-field microscopy. Nature *321*, 605–607.

Howard, J., and Hyman, A.A. (2007). Microtubule polymerases and depolymerases. Curr. Opin. Cell Biol. *19*, 31–35.

Hoyle, H.D., and Raff, E.C. (1990). Two Drosophila beta tubulin isoforms are not functionally equivalent. J. Cell Biol. *111*, 1009–1026.

Hoyt, M.A., He, L., Loo, K.K., and Saunders, W.S. (1992). Two Saccharomyces cerevisiae kinesin-related gene products required for mitotic spindle assembly. J. Cell Biol. *118*, 109–120.

Hu, C.-K., Coughlin, M., Field, C.M., and Mitchison, T.J. (2011). KIF4 Regulates Midzone Length during Cytokinesis. Curr. Biol. *21*, 815–824.

Hu, C.-K., Özlü, N., Coughlin, M., Steen, J.J., and Mitchison, T.J. (2012). Plk1 negatively regulates PRC1 to prevent premature midzone formation before cytokinesis. Mol. Biol. Cell *23*, 2702–2711.

Huxley, H.E. (1963). Electron microscope studies on the structure of natural and synthetic protein filaments from striated muscle. J. Mol. Biol. *7*, 281-IN30.

Huxley, H.E. (1969). The Mechanism of Muscular Contraction. Science *164*, 1356–1366.

Hyman, A.A., Salser, S., Drechsel, D.N., Unwin, N., and Mitchison, T.J. (1992). Role of GTP hydrolysis in microtubule dynamics: information from a slowly hydrolyzable analogue, GMPCPP. Mol. Biol. Cell *3*, 1155–1167.

Inoué, S., and Sato, H. (1967). Cell Motility by Labile Association of Molecules: The nature of mitotic spindle fibers and their role in chromosome movement. J. Gen. Physiol. *50*, 259–292.

Janke, C. (2014). The tubulin code: Molecular components, readout mechanisms, and functions. J Cell Biol *206*, 461–472.

Janson, M.E., Loughlin, R., Loïodice, I., Fu, C., Brunner, D., Nédélec, F.J., and Tran, P.T. (2007). Crosslinkers and Motors Organize Dynamic Microtubules to Form Stable Bipolar Arrays in Fission Yeast. Cell *128*, 357–368.

Jiang, Y.Q., and Oblinger, M.M. (1992). Differential regulation of βIII and other tubulin genes during peripheral and central neuron development. J. Cell Sci. *103*, 643–651.

Jiang, K., Hua, S., Mohan, R., Grigoriev, I., Yau, K.W., Liu, Q., Katrukha, E.A., Altelaar, A.F.M., Heck, A.J.R., Hoogenraad, C.C., et al. (2014). Microtubule Minus-End Stabilization by Polymerization-Driven CAMSAP Deposition. Dev. Cell *28*, 295–309.

Jiang, W., Jimenez, G., Wells, N.J., Hope, T.J., Wahl, G.M., Hunter, T., and Fukunaga, R. (1998). PRC1: A Human Mitotic Spindle–Associated CDK Substrate Protein Required for Cytokinesis. Mol. Cell 9.

Jordan, M.A., Wendell, K., Gardiner, S., Derry, W.B., Copp, H., and Wilson, L. (1996). Mitotic Block Induced in HeLa Cells by Low Concentrations of Paclitaxel (Taxol) Results in Abnormal Mitotic Exit and Apoptotic Cell Death. Cancer Res. *56*, 816–825.

Kajtez, J., Solomatina, A., Novak, M., Polak, B., Vukušić, K., Rüdiger, J., Cojoc, G., Milas, A., Šumanovac Šestak, I., Risteski, P., et al. (2016). Overlap microtubules link sister k-fibres and balance the forces on bi-oriented kinetochores. Nat. Commun. *7*, 10298.

Kapitein, L.C., and Hoogenraad, C.C. (2015). Building the Neuronal Microtubule Cytoskeleton. Neuron *87*, 492–506.

Kapitein, L.C., Peterman, E.J.G., Kwok, B.H., Kim, J.H., Kapoor, T.M., and Schmidt, C.F. (2005). The bipolar mitotic kinesin Eg5 moves on both microtubules that it crosslinks. Nature *435*, 114–118.

Kapoor, T.M., Mayer, T.U., Coughlin, M.L., and Mitchison, T.J. (2000). Probing Spindle Assembly Mechanisms with Monastrol, a Small Molecule Inhibitor of the Mitotic Kinesin, Eg5. J. Cell Biol. *150*, 975–988.

Kashlna, A.S., Baskin, R.J., Cole, D.G., Wedaman, K.P., Saxton, W.M., and Scholey, J.M. (1996). A bipolar kinesin. Nature *379*, 270–272.

Kellogg, E.H., Howes, S., Ti, S.-C., Ramírez-Aportela, E., Kapoor, T.M., Chacón, P., and Nogales, E. (2016). Near-atomic cryo-EM structure of PRC1 bound to the microtubule. Proc. Natl. Acad. Sci. *113*, 9430–9439.

Kerssemakers, J.W.J., Laura Munteanu, E., Laan, L., Noetzel, T.L., Janson, M.E., and Dogterom, M. (2006). Assembly dynamics of microtubules at molecular resolution. Nature *442*, 709–712.

Khmelinskii, A., and Schiebel, E. (2008). Assembling the spindle midzone in the right place at the right time. Cell Cycle *7*, 283–286.

Khmelinskii, A., Roostalu, J., Roque, H., Antony, C., and Schiebel, E. (2009). Phosphorylation-Dependent Protein Interactions at the Spindle Midzone Mediate Cell Cycle Regulation of Spindle Elongation. Dev. Cell *17*, 244–256.

Khodjakov, A., La Terra, S., and Chang, F. (2004). Laser Microsurgery in Fission Yeast: Role of the Mitotic Spindle Midzone in Anaphase B. Curr. Biol. *14*, 1330–1340.

Kirschner, M.W., Williams, R.C., Weingarten, M., and Gerhart, J.C. (1974). Microtubules from Mammalian Brain: Some Properties of Their

Depolymerization Products and a Proposed Mechanism of Assembly and Disassembly. Proc. Natl. Acad. Sci. U. S. A. *71*, 1159–1163.

Kollman, J.M., Merdes, A., Mourey, L., and Agard, D.A. (2011). Microtubule nucleation by γ-tubulin complexes. Nat. Rev. Mol. Cell Biol. *12*, 709–721.

Kozlowski, C., Srayko, M., and Nedelec, F. (2007). Cortical Microtubule Contacts Position the Spindle in C. elegans Embryos. Cell *129*, 499–510.

Kurasawa, Y., Earnshaw, W.C., Mochizuki, Y., Dohmae, N., and Todokoro, K. (2004). Essential roles of KIF4 and its binding partner PRC1 in organized central spindle midzone formation. EMBO J. *23*, 3237–3248.

Laan, L., Pavin, N., Husson, J., Romet-Lemonne, G., van Duijn, M., López, M.P., Vale, R.D., Jülicher, F., Reck-Peterson, S.L., and Dogterom, M. (2012). Cortical dynein controls microtubule dynamics to generate pulling forces that position microtubule asters. Cell *148*, 502–514.

Lansky, Z., Braun, M., Lüdecke, A., Schlierf, M., ten Wolde, P.R., Janson, M.E., and Diez, S. (2015). Diffusible Crosslinkers Generate Directed Forces in Microtubule Networks. Cell *160*, 1159–1168.

Leandro-García, L.J., Leskelä, S., Landa, I., Montero-Conde, C., López-Jiménez, E., Letón, R., Cascón, A., Robledo, M., and Rodríguez-Antona, C. (2010). Tumoral and tissue-specific expression of the major human β-tubulin isotypes. Cytoskeleton *67*, 214–223.

Leandro-García, L.J., Leskelä, S., Inglada-Pérez, L., Landa, I., Cubas, A.A. de, Maliszewska, A., Comino-Méndez, I., Letón, R., Gómez-Graña, Á., Torres, R., et al. (2012). Hematologic β-Tubulin VI Isoform Exhibits Genetic Variability That Influences Paclitaxel Toxicity. Cancer Res. *72*, 4744–4752.

Leduc, C., Padberg-Gehle, K., Varga, V., Helbing, D., Diez, S., and Howard, J. (2012). Molecular crowding creates traffic jams of kinesin motors on microtubules. Proc. Natl. Acad. Sci. *109*, 6100–6105.

Lee, K.-Y., Esmaeili, B., Zealley, B., and Mishima, M. (2015). Direct interaction between centralspindlin and PRC1 reinforces mechanical resilience of the central spindle. Nat. Commun. *6*, 7290.

Leslie, R.J., and Pickett-Heapes, J.D. (1983). Ultraviolet microbeam irradiations of mitotic diatoms: investigation of spindle elongation. J. Cell Biol. *96*, 548–561.

Lewis, S.A., Gu, W., and Cowan, N.J. (1987). Free intermingling of mammalian β-tubulin isotypes among functionally distinct microtubules. Cell *49*, 539–548.

Liu, J., Wang, Z., Jiang, K., Zhang, L., Zhao, L., Hua, S., Yan, F., Yang, Y., Wang, D., Fu, C., et al. (2009). PRC1 Cooperates with CLASP1 to Organize Central Spindle Plasticity in Mitosis. J. Biol. Chem. *284*, 23059–23071.

Liu, S., Kwon, M., Mannino, M., Yang, N., Renda, F., Khodjakov, A., and Pellman, D. (2018). Nuclear envelope assembly defects link mitotic errors to chromothripsis. Nature *561*, 551–555.

Loïodice, I., Staub, J., Setty, T.G., Nguyen, N.-P.T., Paoletti, A., and Tran, P.T. (2005). Ase1p Organizes Antiparallel Microtubule Arrays during Interphase and Mitosis in Fission Yeast. Mol. Biol. Cell *16*, 1756–1768.

Lu, Q., and Ludueña, R.F. (1994). In vitro analysis of microtubule assembly of isotypically pure tubulin dimers. Intrinsic differences in the assembly properties of alpha beta II, alpha beta III, and alpha beta IV tubulin dimers in the absence of microtubule-associated proteins. J. Biol. Chem. *269*, 2041–2047.

Ludueña, R.F. (2013). A Hypothesis on the Origin and Evolution of Tubulin. In International Review of Cell and Molecular Biology, K.W. Jeon, ed. (Academic Press), pp. 41–185.

Ludueña, R.F., and Banerjee, A. (2008). The Isotypes of Tubulin. In The Role of Microtubules in Cell Biology, Neurobiology, and Oncology, T. Fojo, ed. (Totowa, NJ: Humana Press), pp. 123–175.

Magidson, V., O'Connell, C.B., Lončarek, J., Paul, R., Mogilner, A., and Khodjakov, A. (2011). The Spatial Arrangement of Chromosomes during Prometaphase Facilitates Spindle Assembly. Cell *146*, 555–567.

Mandelkow, E.M., Mandelkow, E., and Milligan, R.A. (1991). Microtubule dynamics and microtubule caps: a time-resolved cryo-electron microscopy study. J. Cell Biol. *114*, 977–991.

Mastronarde, D.N. (1993). Interpolar spindle microtubules in PTK cells. J. Cell Biol. *123*, 1475–1489.

Maton, G., Edwards, F., Lacroix, B., Stefanutti, M., Laband, K., Lieury, T., Kim, T., Espeut, J., Canman, J.C., and Dumont, J. (2015). Kinetochore components are required for central spindle assembly. Nat. Cell Biol. *17*, 697–705.

Maurer, S.P., Fourniol, F.J., Bohner, G., Moores, C.A., and Surrey, T. (2012). EBs Recognize a Nucleotide-Dependent Structural Cap at Growing Microtubule Ends. Cell *149*, 371–382.

Mayer, T.U., Kapoor, T.M., Haggarty, S.J., King, R.W., Schreiber, S.L., and Mitchison, T.J. (1999). Small Molecule Inhibitor of Mitotic Spindle Bipolarity Identified in a Phenotype-Based Screen. Science *286*, 971–974.

McDonald, K., Pickett-Heaps, J.D., McIntosh, J.R., and Tippit, D.H. (1977). On the mechanism of anaphase spindle elongation in Diatoma vulgare. J. Cell Biol. *74*, 377–388.

McDonald, K.L., O'Toole, E.T., Mastronarde, D.N., and McIntosh, J.R. (1992). Kinetochore microtubules in PTK cells. J. Cell Biol. *118*, 369–383.

McIntosh, J.R., and Euteneuer, U. (1984). Tubulin hooks as probes for microtubule polarity: an analysis of the method and an evaluation of data on microtubule polarity in the mitotic spindle. J. Cell Biol. *98*, 525–533.

McIntosh, J.R., and Landis, S.C. (1971). The Distribution of Spindle Microtubules During Mitosis in Cultured Human Cells. J. Cell Biol. *49*, 468–497.

Mcintosh, J.R., Hepler, P.K., and Wie, D.G.V. (1969). Model for Mitosis. Nature *224*, 659–663.

McIntosh, J.R., Roos, U.P., Neighbors, B., and McDonald, K.L. (1985). Architecture of the microtubule component of mitotic spindles from Dictyostelium discoideum. J. Cell Sci. *75*, 93–129.

McKinley, K.L., and Cheeseman, I.M. (2017). Large-Scale Analysis of CRISPR/Cas9 Cell-Cycle Knockouts Reveals the Diversity of p53-Dependent Responses to Cell-Cycle Defects. Dev. Cell *40*, 405-420.e2.

Medrano, F.J., Andreu, J.M., Gorbunoff, M.J., and Timasheff, S.N. (1989). Roles of colchicine rings B and C in the binding process to tubulin. Biochemistry *28*, 5589–5599.

Melki, R., Carlier, M.F., Pantaloni, D., and Timasheff, S.N. (1989). Cold depolymerization of microtubules to double rings: geometric stabilization of assemblies. Biochemistry *28*, 9143–9152.

Minoura, I., Hachikubo, Y., Yamakita, Y., Takazaki, H., Ayukawa, R., Uchimura, S., and Muto, E. (2013). Overexpression, purification, and functional analysis of recombinant human tubulin dimer. FEBS Lett. *587*, 3450–3455.

Mishima, M., Kaitna, S., and Glotzer, M. (2002). Central Spindle Assembly and Cytokinesis Require a Kinesin-like Protein/RhoGAP Complex with Microtubule Bundling Activity. Dev. Cell *2*, 41–54.

Mitchison, T.J. (1993). Localization of an exchangeable GTP binding site at the plus end of microtubules. Science *261*, 1044–1047.

Mitchison, T., and Kirschner, M. (1984). Dynamic instability of microtubule growth. Nature *312*, 237–242.

Mohan, R., Katrukha, E.A., Doodhi, H., Smal, I., Meijering, E., Kapitein, L.C., Steinmetz, M.O., and Akhmanova, A. (2013). End-binding proteins sensitize microtubules to the action of microtubule-targeting agents. Proc. Natl. Acad. Sci. *110*, 8900–8905.

Mollinari, C., Kleman, J.-P., Jiang, W., Schoehn, G., Hunter, T., and Margolis, R.L. (2002). PRC1 is a microtubule binding and bundling protein essential to maintain the mitotic spindle midzone. J. Cell Biol. *157*, 1175–1186.

Mollinari, C., Kleman, J.-P., Saoudi, Y., Jablonski, S.A., Perard, J., Yen, T.J., and Margolis, R.L. (2005). Ablation of PRC1 by Small Interfering RNA Demonstrates that Cytokinetic Abscission Requires a Central Spindle Bundle in Mammalian Cells, whereas Completion of Furrowing Does Not. Mol. Biol. Cell *16*, 1043–1055.

Morris, N.R. (1975). Mitotic mutants of Aspergillus nidulans. Genet. Res. *26*, 237–254.

Nawrotek, A., Knossow, M., and Gigant, B. (2011). The Determinants That Govern Microtubule Assembly from the Atomic Structure of GTP-Tubulin. J. Mol. Biol. *412*, 35–42.

Neef, R., Gruneberg, U., Kopajtich, R., Li, X., Nigg, E.A., Sillje, H., and Barr, F.A. (2007). Choice of Plk1 docking partners during mitosis and cytokinesis is controlled by the activation state of Cdk1. Nat. Cell Biol. *9*, 436–444.

Nicklas, R.B. (1965). CHROMOSOME VELOCITY DURING MITOSIS AS A FUNCTION OF CHROMOSOME SIZE AND POSITION. J. Cell Biol. *25*, 119–135.

Nicklas, R.B. (1983). Measurements of the force produced by the mitotic spindle in anaphase. J. Cell Biol. *97*, 542–548.

Nislow, C. (1990). A monoclonal antibody to a mitotic microtubule-associated protein blocks mitotic progression. J. Cell Biol. *111*, 511–522.

Nislow, C., Lombillo, V.A., Kuriyama, R., and Mclntosh, J.R. (1992). A plus-end-directed motor enzyme that moves antiparallel microtubules in vitro localizes to the interzone of mitotic spindles. Nature *359*, 543–547.

Niwa, S., Takahashi, H., and Hirokawa, N. (2013). β-Tubulin mutations that cause severe neuropathies disrupt axonal transport. EMBO J. *32*, 1352–1364.

Nogales, E. (2000). Structural Insights into Microtubule Function. Annu. Rev. Biochem. *69*, 277–302.

Nogales, E., and Kellogg, E.H. (2017). Challenges and opportunities in the high-resolution cryo-EM visualization of microtubules and their binding partners. Curr. Opin. Struct. Biol. *46*, 65–70.

Nogales, E., and Zhang, R. (2016). Visualizing microtubule structural transitions and interactions with associated proteins. Curr. Opin. Struct. Biol. *37*, 90–96.

Nogales, E., Wolf, S.G., and Downing, K.H. (1998). Structure of the αβ tubulin dimer by electron crystallography. Nature *391*, 199–203.

O'Brien, E.T., Voter, W.A., and Erickson, H.P. (1987). GTP hydrolysis during microtubule assembly. Biochemistry *26*, 4148–4156.

O'Connell, K.F., Leys, C.M., and White, J.G. (1998). A genetic screen for temperature-sensitive cell-division mutants of Caenorhabditis elegans. Genetics *149*, 1303–1321.

Odde, D.J., Cassimeris, L., and Buettner, H.M. (1995). Kinetics of microtubule catastrophe assessed by probabilistic analysis. Biophys. J. *69*, 796–802.

Oosawa, F. (1970). Size distribution of protein polymers. J. Theor. Biol. *27*, 69–86.

Oosawa, F. (1975). Thermodynamics of the polymerization of protein (London ; New York: Academic Press).

Panda, D., Miller, H.P., Banerjee, A., Ludueña, R.F., and Wilson, L. (1994). Microtubule dynamics in vitro are regulated by the tubulin isotype composition. Proc. Natl. Acad. Sci. U. S. A. *91*, 11358–11362.

Pecqueur, L., Duellberg, C., Dreier, B., Jiang, Q., Wang, C., Plückthun, A., Surrey, T., Gigant, B., and Knossow, M. (2012). A designed ankyrin repeat protein selected to bind to tubulin caps the microtubule plus end. Proc. Natl. Acad. Sci. U. S. A. *109*, 12011–12016.

Pellman, D. (1995). Two microtubule-associated proteins required for anaphase spindle movement in Saccharomyces cerevisiae [published erratum appears in J Cell Biol 1995 Oct;131(2):561]. J. Cell Biol. *130*, 1373–1385.

Peris, L., Wagenbach, M., Lafanechère, L., Brocard, J., Moore, A.T., Kozielski, F., Job, D., Wordeman, L., and Andrieux, A. (2009). Motor-dependent microtubule disassembly driven by tubulin tyrosination. J. Cell Biol. *185*, 1159–1166.

Pierson, G.B., Burton, P.R., and Himes, R.H. (1978). Alterations in number of protofilaments in microtubules assembled in vitro. J. Cell Biol. *76*, 223–228.

Pipeleers, D.G., Pipeleers-Marichal, M.A., and Kipnis, D.M. (1977). Physiological regulation of total tubulin and polymerized tubulin in tissues. J. Cell Biol. *74*, 351–357.

Polak, B., Risteski, P., Lesjak, S., and Tolić, I.M. (2017). PRC1-labeled microtubule bundles and kinetochore pairs show one-to-one association in metaphase. EMBO Rep. *18*, 217–230.

Rappaport, R. (1996). Cytokinesis in Animal Cells by R. Rappaport.

Ravelli, R.B.G., Gigant, B., Curmi, P.A., Jourdain, I., Lachkar, S., Sobel, A., and Knossow, M. (2004). Insight into tubulin regulation from a complex with colchicine and a stathmin-like domain. Nature *428*, 198–202.

Rice, L.M., Montabana, E.A., and Agard, D.A. (2008). The lattice as allosteric effector: Structural studies of αβ- and γ-tubulin clarify the role of GTP in microtubule assembly. Proc. Natl. Acad. Sci. U. S. A. *105*, 5378–5383.

Ris, H. (1943). A quantitative study of anaphase movement in the aphid tamalia. Biol. Bull. *85*, 164–178.

Ris, H. (1949). The anaphase movement of chromosomes in the spermatocytes of the grasshopper. Biol. Bull. *96*, 90–106.

Rizk, R.S., DiScipio, K.A., Proudfoot, K.G., and Gupta, M.L. (2014). The kinesin-8 Kip3 scales anaphase spindle length by suppression of midzone microtubule polymerization. J Cell Biol *204*, 965–975.

Roll-Mecak, A. (2019). How cells exploit tubulin diversity to build functional cellular microtubule mosaics. Curr. Opin. Cell Biol. *56*, 102–108.

Roll-Mecak, A., and McNally, F.J. (2010). Microtubule-severing enzymes. Curr. Opin. Cell Biol. *22*, 96–103.

Roof, D.M., Meluh, P.B., and Rose, M.D. (1992). Kinesin-related proteins required for assembly of the mitotic spindle. J. Cell Biol. *118*, 95–108.

Roostalu, J., Schiebel, E., and Khmelinskii, A. (2010). Cell cycle control of spindle elongation. Cell Cycle *9*, 1084–1090.

Saillour, Y., Broix, L., Bruel-Jungerman, E., Lebrun, N., Muraca, G., Rucci, J., Poirier, K., Belvindrah, R., Francis, F., and Chelly, J. (2014). Beta tubulin isoforms are not interchangeable for rescuing impaired radial migration due to Tubb3 knockdown. Hum. Mol. Genet. *23*, 1516–1526.

Saunders, W.S., and Hoyt, M.A. (1992). Kinesin-related proteins required for structural integrity of the mitotic spindle. Cell *70*, 451–458.

Saunders, A.M., Powers, J., Strome, S., and Saxton, W.M. (2007). Kinesin-5 acts as a brake in anaphase spindle elongation. Curr. Biol. *17*, R453–R454.

Sawin, K.E., LeGuellec, K., Philippe, M., and Mitchison, T.J. (1992). Mitotic spindle organization by a plus-end-directed microtubule motor. Nature *359*, 540–543.

Saxton, W.M., and McIntosh, J.R. (1987). Interzone microtubule behavior in late anaphase and telophase spindles. J. Cell Biol. *105*, 875–886.

Schaedel, L., John, K., Gaillard, J., Nachury, M.V., Blanchoin, L., and Théry, M. (2015). Microtubules self-repair in response to mechanical stress. Nat. Mater. *14*, 1156–1163.

Schek, H.T., Gardner, M.K., Cheng, J., Odde, D.J., and Hunt, A.J. (2007). Microtubule Assembly Dynamics at the Nanoscale. Curr. Biol. *17*, 1445–1455.

Schindelin, J., Arganda-Carreras, I., Frise, E., Kaynig, V., Longair, M., Pietzsch, T., Preibisch, S., Rueden, C., Saalfeld, S., Schmid, B., et al. (2012). Fiji: an open-source platform for biological-image analysis. Nat. Methods *9*, 676–682.

Scholey, J.M., Civelekoglu-Scholey, G., and Brust-Mascher, I. (2016). Anaphase B. Biology *5*.

Schrader, F. (1949). Mitosis. The movements of chromosomes in cell division. Mitosis Mov. Chromosom. Cell Div.

Schuyler, S.C., Liu, J.Y., and Pellman, D. (2003). The molecular function of Ase1p: evidence for a MAP-dependent midzone-specific spindle matrix. J. Cell Biol. *160*, 517–528.

Seetapun, D., Castle, B.T., McIntyre, A.J., Tran, P.T., and Odde, D.J. (2012). Estimating the Microtubule GTP Cap Size In Vivo. Curr. Biol. *22*, 1681–1687.

Sharp, D.J., Yu, K.R., Sisson, J.C., Sullivan, W., and Scholey, J.M. (1999). Antagonistic microtubule-sliding motors position mitotic centrosomes in *Drosophila* early embryos. Nat. Cell Biol. *1*, 51–54.

Shimamoto, Y., Forth, S., and Kapoor, T.M. (2015). Measuring Pushing and Braking Forces Generated by Ensembles of Kinesin-5 Crosslinking Two Microtubules. Dev. Cell *34*, 669–681.

Sirajuddin, M., Rice, L.M., and Vale, R.D. (2014). Regulation of microtubule motors by tubulin isotypes and post-translational modifications. Nat. Cell Biol. *16*, 335–344.

Slangy, A., Lane, H.A., d'Hérin, P., Harper, M., Kress, M., and Niggt, E.A. (1995). Phosphorylation by p34cdc2 regulates spindle association of human Eg5, a kinesin-related motor essential for bipolar spindle formation in vivo. Cell *83*, 1159–1169.

Song, Y.H., and Mandelkow, E. (1993). Recombinant kinesin motor domain binds to beta-tubulin and decorates microtubules with a B surface lattice. Proc. Natl. Acad. Sci. U. S. A. *90*, 1671–1675.

Sosa, H., Dias, D.P., Hoenger, A., Whittaker, M., Wilson-Kubalek, E., Sablin, E., Fletterick, R.J., Vale, R.D., and Milligan, R.A. (1997). A Model for the Microtubule-Ncd Motor Protein Complex Obtained by Cryo-Electron Microscopy and Image Analysis. Cell *90*, 217–224.

Su, K.-C., Barry, Z., Schweizer, N., Maiato, H., Bathe, M., and Cheeseman, I.M. (2016). A Regulatory Switch Alters Chromosome Motions at the Metaphase-to-Anaphase Transition. Cell Rep. *17*, 1728–1738.

Su, X., Arellano-Santoyo, H., Portran, D., Gaillard, J., Vantard, M., Thery, M., and Pellman, D. (2013). Microtubule sliding activity of a kinesin-8 promotes spindle assembly and spindle length control. Nat. Cell Biol. *15*, 948–957.

Subramanian, R., and Kapoor, T.M. (2012). Building Complexity: Insights into Self-organized Assembly of Microtubule-based Architectures. Dev. Cell *23*, 874–885.

Subramanian, R., Wilson-Kubalek, E.M., Arthur, C.P., Bick, M.J., Campbell, E.A., Darst, S.A., Milligan, R.A., and Kapoor, T.M. (2010). Insights into Antiparallel Microtubule Crosslinking by PRC1, a Conserved Nonmotor Microtubule Binding Protein. Cell *142*, 433–443.

Subramanian, R., Ti, S.-C., Tan, L., Darst, S.A., and Kapoor, T.M. (2013). Marking and Measuring Single Microtubules by PRC1 and Kinesin-4. Cell *154*, 377–390.

Tao, L., Fasulo, B., Warecki, B., and Sullivan, W. (2016). Tum/RacGAP functions as a switch activating the Pav/kinesin-6 motor. Nat. Commun. *7*, 11182.

Telzer, B.R., and Haimo, L.T. (1981). Decoration of spindle microtubules with Dynein: evidence for uniform polarity. J. Cell Biol. *89*, 373–378.

Ti, S.-C., Pamula, M.C., Howes, S.C., Duellberg, C., Cade, N.I., Kleiner, R.E., Forth, S., Surrey, T., Nogales, E., and Kapoor, T.M. (2016). Mutations in Human Tubulin Proximal to the Kinesin-Binding Site Alter Dynamic Instability at Microtubule Plus- and Minus-Ends. Dev. Cell *37*, 72–84.

Ti, S.-C., Alushin, G.M., and Kapoor, T.M. (2018). Human β-Tubulin Isotypes Can Regulate Microtubule Protofilament Number and Stability. Dev. Cell.

Tikhonenko, I., Nag, D.K., Martin, N., and Koonce, M.P. (2008). Kinesin-5 is not essential for mitotic spindle elongation in Dictyostelium. Cell Motil. Cytoskeleton *65*, 853–862.

Tischfield, M.A., Baris, H.N., Wu, C., Rudolph, G., Van Maldergem, L., He, W., Chan, W.-M., Andrews, C., Demer, J.L., Robertson, R.L., et al. (2010). Human TUBB3 Mutations Perturb Microtubule Dynamics, Kinesin Interactions, and Axon Guidance. Cell *140*, 74–87.

Tischfield, M.A., Cederquist, G.Y., Gupta, M.L., and Engle, E.C. (2011). Phenotypic spectrum of the tubulin-related disorders and functional implications of disease-causing mutations. Curr. Opin. Genet. Dev. *21*, 286–294.

Tolić-Nørrelykke, I.M., Sacconi, L., Thon, G., and Pavone, F.S. (2004). Positioning and Elongation of the Fission Yeast Spindle by Microtubule-Based Pushing. Curr. Biol. *14*, 1181–1186.

Tran, P.T., Walker, R.A., and Salmon, E.D. (1997). A Metastable Intermediate State of Microtubule Dynamic Instability That Differs Significantly between Plus and Minus Ends. J. Cell Biol. *138*, 105–117.

Vale, R.D., and Fletterick, R.J. (1997). The design plan of kinesin motors. Annu. Rev. Cell Dev. Biol. *13*, 745–777.

Varga, V., Helenius, J., Tanaka, K., Hyman, A.A., Tanaka, T.U., and Howard, J. (2006). Yeast kinesin-8 depolymerizes microtubules in a length-dependent manner. Nat. Cell Biol. *8*, 957–962.

Varga, V., Leduc, C., Bormuth, V., Diez, S., and Howard, J. (2009). Kinesin-8 Motors Act Cooperatively to Mediate Length-Dependent Microtubule Depolymerization. Cell *138*, 1174–1183.

Vemu, A., Szczesna, E., Zehr, E.A., Spector, J.O., Grigorieff, N., Deaconescu, A.M., and Roll-Mecak, A. (2018). Severing enzymes amplify microtubule arrays through lattice GTP-tubulin incorporation. Science *361*, eaau1504.

Verbrugghe, K.J.C., and White, J.G. (2004). SPD-1 Is Required for the Formation of the Spindle Midzone but Is Not Essential for the Completion of Cytokinesis in C. elegans Embryos. Curr. Biol. *14*, 1755–1760.

Verde, F., Dogterom, M., Stelzer, E., Karsenti, E., and Leibler, S. (1992). Control of microtubule dynamics and length by cyclin A- and cyclin B-dependent kinases in Xenopus egg extracts. J. Cell Biol. *118*, 1097–1108.

Verhey, K.J., and Gaertig, J. (2007). The tubulin code. Cell Cycle Georget. Tex *6*, 2152–2160.

Vernì, F., Somma, M.P., Gunsalus, K.C., Bonaccorsi, S., Belloni, G., Goldberg, M.L., and Gatti, M. (2004). Feo, the Drosophila Homolog of PRC1, Is Required for Central-Spindle Formation and Cytokinesis. Curr. Biol. *14*, 1569–1575.

Vukušić, K., Buđa, R., Bosilj, A., Milas, A., Pavin, N., and Tolić, I.M. (2017). Microtubule Sliding within the Bridging Fiber Pushes Kinetochore Fibers Apart to Segregate Chromosomes. Dev. Cell *43*, 11-23.e6.

Walker, R.A., O'Brien, E.T., Pryer, N.K., Soboeiro, M.F., Voter, W.A., Erickson, H.P., and Salmon, E.D. (1988). Dynamic instability of individual microtubules analyzed by video light microscopy: rate constants and transition frequencies. J. Cell Biol. *107*, 1437–1448.

Walker, R.A., Inoué, S., and Salmon, E.D. (1989). Asymmetric behavior of severed microtubule ends after ultraviolet-microbeam irradiation of individual microtubules in vitro. J. Cell Biol. *108*, 931–937.

Walker, R.A., Pryer, N.K., and Salmon, E.D. (1991). Dilution of individual microtubules observed in real time in vitro: evidence that cap size is small and independent of elongation rate. J. Cell Biol. *114*, 73–81.

Wang, H.-W., and Nogales, E. (2005). Nucleotide-dependent bending flexibility of tubulin regulates microtubule assembly. Nature *435*, 911–915.

Wang, D., Villasante, A., Lewis, S.A., and Cowan, N.J. (1986). The mammalian beta-tubulin repertoire: hematopoietic expression of a novel, heterologous beta-tubulin isotype. J. Cell Biol. *103*, 1903–1910.

Waters, J.C., Cole, R.W., and Rieder, C.L. (1993). The force-producing mechanism for centrosome separation during spindle formation in vertebrates is intrinsic to each aster. J. Cell Biol. *122*, 361–372.

Weinger, J.S., Qiu, M., Yang, G., and Kapoor, T.M. (2011). A Nonmotor Microtubule Binding Site in Kinesin-5 Is Required for Filament Crosslinking and Sliding. Curr. Biol. *21*, 154–160.

Weisenberg, R.C., and Deery, W.J. (1976). Role of nucleotide hydrolysis in microtubule assembly. Nature *263*, 792–793.

Weisenberg, R.C., Broisy, G.G., and Taylor, E.W. (1968). Colchicine-binding protein of mammalian brain and its relation to microtubules. Biochemistry *7*, 4466–4479.

Westermann, S., and Weber, K. (2003). Post-translational modifications regulate microtubule function. Nat. Rev. Mol. Cell Biol. *4*, 938–948.

White, E.A., and Glotzer, M. (2012). Centralspindlin: At the heart of cytokinesis. Cytoskeleton *69*, 882–892.

Widlund, P.O., Podolski, M., Reber, S., Alper, J., Storch, M., Hyman, A.A., Howard, J., Drechsel, D.N., and Drubin, D.G. (2012). One-step purification of assembly-competent tubulin from diverse eukaryotic sources. Mol. Biol. Cell *23*, 4393–4401.

Wieczorek, M., Bechstedt, S., Chaaban, S., and Brouhard, G.J. (2015). Microtubule-associated proteins control the kinetics of microtubule nucleation. Nat. Cell Biol. *17*, 907–916.

Wijeratne, S., and Subramanian, R. (2018). Geometry of antiparallel microtubule bundles regulates relative sliding and stalling by PRC1 and Kif4A. ELife *7*, e32595.

Winey, M., Mamay, C.L., O'Toole, E.T., Mastronarde, D.N., Giddings, T.H., McDonald, K.L., and McIntosh, J.R. (1995). Three-dimensional ultrastructural analysis of the Saccharomyces cerevisiae mitotic spindle. J. Cell Biol. *129*, 1601–1615.

Yamashita, A., Sato, M., Fujita, A., Yamamoto, M., and Toda, T. (2005). The Roles of Fission Yeast Ase1 in Mitotic Cell Division, Meiotic Nuclear Oscillation, and Cytokinesis Checkpoint Signaling. Mol. Biol. Cell *16*, 1378–1395.

Yamashita, N., Morita, M., Legant, W.R., Chen, B.-C., Betzig, E., Yokota, H., and Mimori-Kiyosue, Y. (2015). Three-dimensional tracking of plus-tips by lattice light-sheet microscopy permits the quantification of microtubule growth trajectories within the mitotic apparatus. J. Biomed. Opt. *20*, 101206.

Yau, K.W., van Beuningen, S.F.B., Cunha-Ferreira, I., Cloin, B.M.C., van Battum, E.Y., Will, L., Schätzle, P., Tas, R.P., van Krugten, J., Katrukha, E.A., et al. (2014). Microtubule Minus-End Binding Protein CAMSAP2 Controls Axon Specification and Dendrite Development. Neuron *82*, 1058–1073.

Zhai, Y., and Borisy, G.G. (1994). Quantitative determination of the proportion of microtubule polymer present during the mitosis-interphase transition. J. Cell Sci. *107*, 881–890.

Zhai, Y., Kronebusch, P.J., Simon, P.M., and Borisy, G.G. (1996). Microtubule dynamics at the G2/M transition: abrupt breakdown of cytoplasmic microtubules at nuclear envelope breakdown and implications for spindle morphogenesis. J. Cell Biol. *135*, 201–214.

Zhang, R., Alushin, G.M., Brown, A., and Nogales, E. (2015). Mechanistic Origin of Microtubule Dynamic Instability and Its Modulation by EB Proteins. Cell *162*, 849–859.

Zhu, C., Lau, E., Schwarzenbacher, R., Bossy-Wetzel, E., and Jiang, W. (2006). Spatiotemporal control of spindle midzone formation by PRC1 in human cells. Proc. Natl. Acad. Sci. *103*, 6196–6201.